Doctoral Dissertation

Gadolinium added uranium mononitride fuels for light water reactor applications: fabrication and thermophysical property measurements

Gyeonghun Kim

Department of Nuclear Engineering

Ulsan National Institute of Science and Technology

2021

Gadolinium added uranium mononitride fuels for light water reactor applications: fabrication and thermophysical property measurements

Gyeonghun Kim

Department of Nuclear Engineering

Ulsan National Institute of Science and Technology

Gadolinium added uranium mononitride fuels for light water reactor applications: fabrication and thermophysical property measurements

A dissertation submitted to
Ulsan National Institute of Science and Technology
in partial fulfillment of the
requirements for the degree of
Doctor of Philosophy

Gyeonghun Kim

06.14.2021 of submission
Approved by

Advisor
Sangjoon Ahn

Gadolinium added uranium mononitride fuels for light water reactor applications: fabrication and thermophysical property measurements

Gyeonghun Kim

This certifies that the dissertation of Gyeonghun Kim is approved.

06.14.2021 of submission

Advisor: Sangjoon Ahn

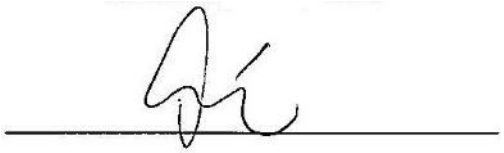

Hee Reyoung Kim

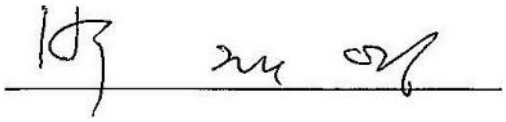

Jaeyoung Park

Eisung Yoon

Seung-Ho Jung

Abstract

The uranium mononitride (UN) has superior thermophysical properties such as high thermal conductivity, melting point, and fissile atom density than traditional uranium dioxide (UO_2) fuels. The use of UN fuel, however, has not been considered economically feasible because extremely high temperature is required to obtain high-density pellets by conventional sintering method. The spark plasma sintering (SPS) has thus been proposed for UN fuel fabrication since this technique has the capability of rapid densification at relatively low temperatures. However, the SPS behavior of UN fuel has not yet been sufficiently studied, for both pure and gadolinium added pellets, two representative types of light water reactor (LWR) fuels.

Densification and grain growth behavior of the pure UN powder during SPS were investigated in a wide range of temperatures (from 1500 to 1800 °C) and times (from 5 to 180 min) under uniaxial pressure of 70 MPa. The hydride-nitride process was employed to synthesize the UN powder with an average particle size of 6.0 ± 4.9 μm. The thermal etching technique was used to reveal the grain boundaries of the pellets. The crystallographic and microstructural characterizations were completed by using X-ray diffraction (XRD) and scanning electron microscope (SEM). Collected data presented in the grain size-density trajectory revealed two distinct stages of the SPS process in accordance with sintering temperature: at temperatures below 1700 °C, the pellet density increased until it reached the maximum value (~97 %TD) as temperature increased, while the grain growth was not significant (average grain size < 3.5 μm); at 1800 °C, the maximum density was very rapidly achieved in less than 5 min, while a considerable grain growth (> 8 μm) was followed with continued heating time (up to 180 min).

Phase stability of UN/GdN and UN/Gd_2O_3 composite pellets was investigated for various compositions of GdN (3.5, 7.0, 10.7, 14.5, and 38.4 wt%) and Gd_2O_3 (5, 10, and 15 wt%). The SPS temperature and time were respectively varied from 1800 to 2000 °C and from 10 to 60 min. The XRD analysis confirmed two separate phase formation in UN/Gd_2O_3 pellets for all SPS conditions. In case of UN/GdN, however, solid-solution $(U_{1-x},Gd_x)N$ phase formation was observed from high temperature (2000 °C) SPSed pellets.

The thermal conductivity of the SPSed UN/GdN and UN/Gd_2O_3 composite pellets was measured from 25 to 1000 °C by using laser flash analysis (LFA). Throughout the temperature range measured, the thermal conductivity of both composite pellets decreased with increasing Gd compositions. The non-solid-solution UN/GdN pellets exhibited 14–25% higher thermal conductivity

than the solid-solution $(U_{1-x},Gd_x)N$ pellets; and even these solid-solution pellets showed 20–65% higher thermal conductivity than the UN/Gd_2O_3 pellets. These results may indicate that relatively higher thermal conductivity of UN/GdN composite as burnable absorber fuel could be further enhanced with an optimized microstructure obtainable from relatively low (< 1800 °C) SPS temperature.

CONTENTS

List of figures

List of tables

Explanation of acronyms and abbreviations

American Society for Testing and Materials (ASTM)

Atomic Percent (at%)

Back-Scattered Electron (BSE)

Beginning of Cycle (BOC)

Burnable Absorber (BA)

Coefficient of Linear Thermal Expansion (CLTE)

Conventional Sintering (CS)

Dilatometer (DIL)

End of Cycle (EOC)

Experimental Breeder Reactor-II (EBRII)

Fission Gas Release (FGR)

Fission Product (FP)

Fuel Cladding Mechanical Interaction (FCMI)

Fuel-Cladding Chemical Interaction (FCCI)

Gadolinium Nitride (GdN)

Hot Pressing (HP)

International Centre for Diffraction Data (ICDD)

Infrared (IR)

Laser Flash Analysis (LFA)

Liquid Nitrogen (LN_2)

Light Water Reactor (LWR)

Mixed Uranium-Plutonium Oxide (MOX)

Moderator Void Coefficient (MVC)

Nuclear Regulatory Commission (NRC)

Powder Diffraction File (PDF)

Post Irradiation Examinations (PIE)

Particle Size Distribution (PSD)

Relative Lattice Parameter Difference (RLPD)

Spark Plasma Sintering (SPS)

Separative Work Unit (SWU)

Specific Heat Capacity (C_p)

Theoretical Density (TD)

Uranium Dioxide (UO_2)

Uranium Mononitride (UN)

Uranium-Plutonium Mixed Nitride (MNUP)

Weight Percent (wt%)

X-Ray Diffraction (XRD)

Chapter 1. INTRODUCTION

1.1. Motivation

Uranium mononitride (UN) has been proposed as a promising nuclear fuel because of its attractive thermophysical properties such as high thermal conductivity, high melting point, and high fissile atom density compared with other representative fuel materials shown in Table 1-1. The thermal conductivity of UN is ~25 W/m·K at 1000 °C [1], while uranium dioxide (UO_2) exhibits only ~2.8 W/m·K at the same temperature [2–4]; the melting point of UN is as high as ~2800 °C; and fissile atom density of UN is ~40% higher than its oxide counterpart. For this reason, many fast reactors [5–9] and space reactors [10–12] have already adopted the UN as an advanced fuel.

The application of UN fuel in light water reactors (LWR) could also bring considerable economic benefits. Currently, more than 500 LWRs, which include about 400 pressurized water reactors (PWR) and 100 boiling water reactors (BWR), are being operated all around the world. These account for ~90% of installed reactor capacity worldwide. Therefore, significant economic advantages could be achieved by uprating existing LWRs' power output and/or by extending fuel cycle length. Previously over the past decades, the United States Nuclear Regulatory Commission (U.S.NRC) has approved 170 uprates of LWRs, which amounted to ~24 gigawatts-thermal (GWth) in total.

Higher fissile density fuel may be required to achieve further power uprates or longer fuel cycle lengths. Since conventional low-enriched UO_2 fuel (< 5% ^{235}U) could not bring such improvements, UN fuel is now being proposed as the fuel alternative not just because of its higher fissile density, but also due to additional safety margin from lower fuel centerline temperature than that of conventional UO_2 fuel. It is estimated by Giudicelli [13] that the power of the AP1000 [14] could be uprated in the order of 15% by using UN fuels even with lower enrichment (~4.3% ^{235}U) and a small number of fuel assemblies (#60) compared to original UO_2 fuels with higher enrichment of ~4.6% ^{235}U and #68 assemblies.

Several challenges, however, remain to be addressed to ensure the technical and economic feasibility of the UN fuel application in LWRs. First, the UN fuel has relatively poor oxidation resistance than that of conventional UO_2 fuel. The pure UN readily oxidizes to whether U_3O_8 in the air at high temperature of ~200 °C [15–17] or UO_2 under super-heated steam atmosphere at ~400 °C [18–21]. Various attempts to overcome this drawback have been made by the means of hydrothermal corrosion

resistant fuel concepts [22–28]. Since previous studies have demonstrated markedly improved oxidation resistance, it is thus becoming quite conceivable to utilize the UN fuel in LWRs.

Another drawback is radionuclide ^{14}C generation in the nitride fuel mainly from $^{14}N(n, p)^{14}C$ reaction. The ^{14}C is a beta emitter with a long half-life of 5730 years and is easily absorbed into a living organism. In consequence, the ^{14}C would contribute a considerable portion of effective dose than any other radionuclides once it is released to the environment from nuclear power plants [29]. Therefore, ^{15}N enrichment up to 99% has been considered to resolve the concern about the potential environmental impact caused by massive ^{14}C production. This would raise the total fuel cost because of the very low ^{15}N natural abundance (0.364%); however, following Wallenius et al. [30], the cost increase would be acceptable (5–10%).

The last major challenge, which increases the fuel fabrication cost considerably, is difficulty in achieving high-density pellets using conventional sintering. According to several post-irradiation examination (PIE) results [31,32], high-density and larger-grained structures are primary requirements for UN fuel to secure its irradiation swelling resistance. Conventional cold-press sintering, which is commonly used in fabricating traditional UO_2 fuel pellets, is economically not applicable for UN, because the process requires extremely high temperature (> 2000 °C) for tens of hours [12] to achieve a pellet density higher than 90 %TD (theoretical density). In recent days, spark plasma sintering (SPS) has demonstrated significant improvements in fabricating various ceramic powders at relatively low sintering temperatures with short dwell times than those of conventional sintering. Up to now, uranium carbide (UC) [33], SiC/UO_2 composites [34], and sub-micrometer grained UO_2 [35] have been successfully fabricated from this advanced technique. The SPS has also been utilized to fabricate UN pellets and has shown promising results [36–42]. Within a short period of introduction, however, the SPS behavior of UN powder was barely investigated. Considering that the performance of nuclear fuel during irradiation is largely affected by the fabrication characteristics such as fuel density, porosity, grain size, and stoichiometry, a comprehensive investigation on the sintering behavior of UN fuel is required to control tightly over fuel characteristics.

With regard to UN fuel application in LWRs, the addition of burnable absorber (BA) element is primarily required to limit the excess reactivity at beginning of the cycle (BOC) and to control the reactivity swing over the cycle. In commercial LWRs, gadolinium is generally used in a chemical form of gadolinium oxide (Gd_2O_3), which is homogeneously blended with the UO_2 powder forming a solid-solution $(U_{1-x},Gd_x)O_2$ phase. For the UN fuel, on the other hand, gadolinium nitride (GdN) would be more suitable additive compound than Gd_2O_3, because GdN could form the solid-solution $(U_{1-x},Gd_x)N$ phase with UN. The use of solid-solution BA fuel could mitigate the unexpected interaction between dispersed Gd compounds and UN matrix, which would change various fuel properties during the

operation. Furthermore, thermal conductivity decrease in UN pellets with increasing Gd concentration is anticipated in the similar manner that thermal conductivity decrease of $(U_{1-x},Gd_x)O_2$ with Gd concentration increase [43,44]. However, experimental study on the fabrication and thermal physical properties of Gd-bearing UN fuels has never been reported up to now.

1.2. Objectives

This study aims to investigate experimentally the fabrication characteristics and thermophysical properties of the pure and Gd-bearing UN fuel pellets sintered by SPS for LWR applications. To achieve this goal, two sub-objectives are established as follows.

For the first part, the effects of SPS operating conditions on densification and grain growth of the pure UN powder are to be investigated in a wide range of temperature (1500–1800 °C) and dwell time (5–180 min). The thermal etching method would be adopted to reveal the grain boundary of the UN pellets instead of the wet chemical etching to avoid the use of toxic etchants including hydrofluoric and nitric acid. Microstructural characterization is to be completed from the analysis of scanning electron microscopy (SEM) images.

For the second part, UN/GdN and UN/Gd_2O_3 composite pellets with various compositions of GdN (3.5, 7.0, 10.7, 14.5, and 38.4 wt%) and Gd_2O_3 (5.0, 10, and 15.0 wt%) are to be fabricated by SPS. The crystal structure of the composite pellets is to be identified by X-ray diffraction (XRD). Surface microstructure characterization would be completed through the scanning electron microscope-backscattered electron (SEM/BSE) image analysis. Thermophysical properties of gadolinium compounds added UN composites would be measured using dilatometer (DIL), and laser flash analyzer (LFA) within the temperature range from 25 to 1000 °C. After then, the thermal conductivity of the UN/Gd_2O_3 and UN/GdN composite pellets are to be calculated from the measured values of the density, thermal expansion coefficient, heat capacity, and thermal diffusivity.

Table 1-1. Comparison of thermophysical properties and swelling behavior of representative nuclear fuel materials

	UO_2	UN	UC	U-10Zr alloy	U_3Si_2
Density (g/cm^3)	11.0	14.3	13.6	15.6	12.2
Melting point (°C)	2865	2800	2480	1160	1665
Thermal conductivity @1000 K (W/m·K)	3.5 [4]	23 [1]	21 [45]	35 [46]	21 [47]
Crystal structure (space group)	Cubic CaF_2-type (Fm-3m)	Cubic NaCl-type (Fm-3m,)	Cubic NaCl-type (Fm-3m)	Various structure (depending on temperature & composition)	Tetragonal (P4/mbm)
Swelling	-	Similar to UO_2	Severe than UO_2	Very severe	Lack of data

Chapter 2. LITERATURE REVIEWS

This chapter is to briefly present the background information required to comprehend this study. Section 2.1. describes the basic characteristics of uranium nitride fuel: crystal structure; thermal properties; and irradiation behavior. Section 2.2. would review UN fuel fabrication methods. In Section 2.3., the rationale for the selection of the Gd_2O_3 and GdN BAs is presented.

2.1. Characteristics of uranium nitride

2.1.1. Crystal structure

The uranium-nitrogen (U-N) system has four different stable stoichiometric compounds: UN, α-U_2N_3, β-U_2N_3, and UN_2 [48–54]. Table 2-1 shows the crystal structural and physical properties of those nitride compounds. The stability of uranium nitrides is highly dependent on nitrogen partial pressure and temperature. Under the inert atmosphere, the higher stoichiometric nitrides decompose into lower stoichiometry as temperature increases: UN_2 begins to decompose into α-U_2N_3 at 675 ℃ [55] as shown in Equation 2-1; α-U_2N_3 decomposes into UN at 975 ℃ [55] (see Equation 2-2); and UN decomposes into metallic uranium and gaseous nitrogen at ~1850 ℃ [56] (see Equation 2-3). A recent study [54] reported, from the first-principles calculations, that several new possible stable stoichiometric compounds (UN_4, UN_3, U_3N_5, and U_2N) would exist under high pressure up to 150 GPa.

$$2UN_2(s) \rightarrow U_2N_3(s) + 1/2N_2(g) \text{ at } 675\ ℃ \quad (2\text{-}1)$$

$$U_2N_3(s) \rightarrow 2UN + 1/2N_2(g) \text{ at } 975\ ℃ \quad (2\text{-}2)$$

$$UN(s) \rightarrow U(s) + 1/2N_2(g) \text{ at } > \sim 1850\ ℃ \quad (2\text{-}3)$$

The decomposition temperature increases as the nitrogen partial pressure increases. The decomposition temperature and corresponding nitrogen partial pressure of U_2N_3 is given in Equation

2-4 [57], where T is the decomposition temperature (K) of U_2N_3 and p_{N_2} is nitrogen partial pressure (atm). According to Equation 2-4, the U_2N_3 decomposition temperature increases up to ~1350 °C under the nitrogen pressure of 1 atm.

$$\log p_{N_2} = 7.201 - 1.174 \times 10^4 / T \tag{2-4}$$

The melting point of UN is equivalent to UN decomposition temperature since the melting point of pure uranium (1132 °C) is much below than UN decomposition temperatures. The melting point of UN is commonly known to be ~2,800 °C; however, it is also strongly dependent on the nitrogen pressure. Olson et al. [58] reported that UN decomposition temperature was determined to be 2,850 °C in 2.5 atm nitrogen from the experimental confirmation, while Benz et al. [59] has reported that the melting temperature is 2,830 °C at 3.5 atm nitrogen. Hayes [60] has developed the relationship between melting temperature and nitrogen pressure for UN based on abovementioned experimental values as shown in Equation (2-5). In Equation 2-5, T_m is the melting point (K) of UN and p_{N_2} is nitrogen pressure (atm). The equation is valid for nitrogen pressures of 1.0×10^{-13} atm $< p <$ 7.5 atm.

$$T_m = 3035.0(p_{N_2})^{0.02832} \tag{2-5}$$

Several uranium-nitrogen (U-N) binary phase diagrams [55,57,61] have been developed based on above mentioned p-T-C relationship. The U-N phase diagram of Tagawa [57] (shown in Figure 2-1) is commonly used. In Tagawa's phase diagram, the α-U_2N_3 phase exhibits a wide range of N/U ratio from 1.54 to 1.75, while the β-U_2N_3 phase is within the hypo-stoichiometric composition range from 1.45 to 1.49. The UN_2 phase exhibits a wide range of N/U ratio from 1.75 to 2.0. It is worthwhile to note that stoichiometric UN_2 has never been prepared experimentally. Thus far, the hypo-stochiometric $UN_{1.83}$ has only been fabricated under extremely high nitrogen pressure of ~200 atm by Katsura and Serizawa [62]. They concluded that nitrogen pressure in the order of 10^5–10^7 atm would be required to obtain stoichiometric UN_2 phase.

Silva et al. [55] proposed that the phase transformation between the β-U_2N_3 and UN_{2-x} occurs through the intermediate UN_2/α-U_2N_3 solid-solution phase. In this solid-solution, the position of uranium and nitrogen ions are continuously shifted with increasing nitrogen contents [63,64]. Nitrogen ions, eventually, occupy eight tetrahedral sites of UN_2 fluorite cubic structure when N/U ratio is above 1.75. Consequently, UN_2/α-U_2N_3 solid solution N/U ratio over 1.75 is named as UN_2 and below it as α-U_2N_3 [65].

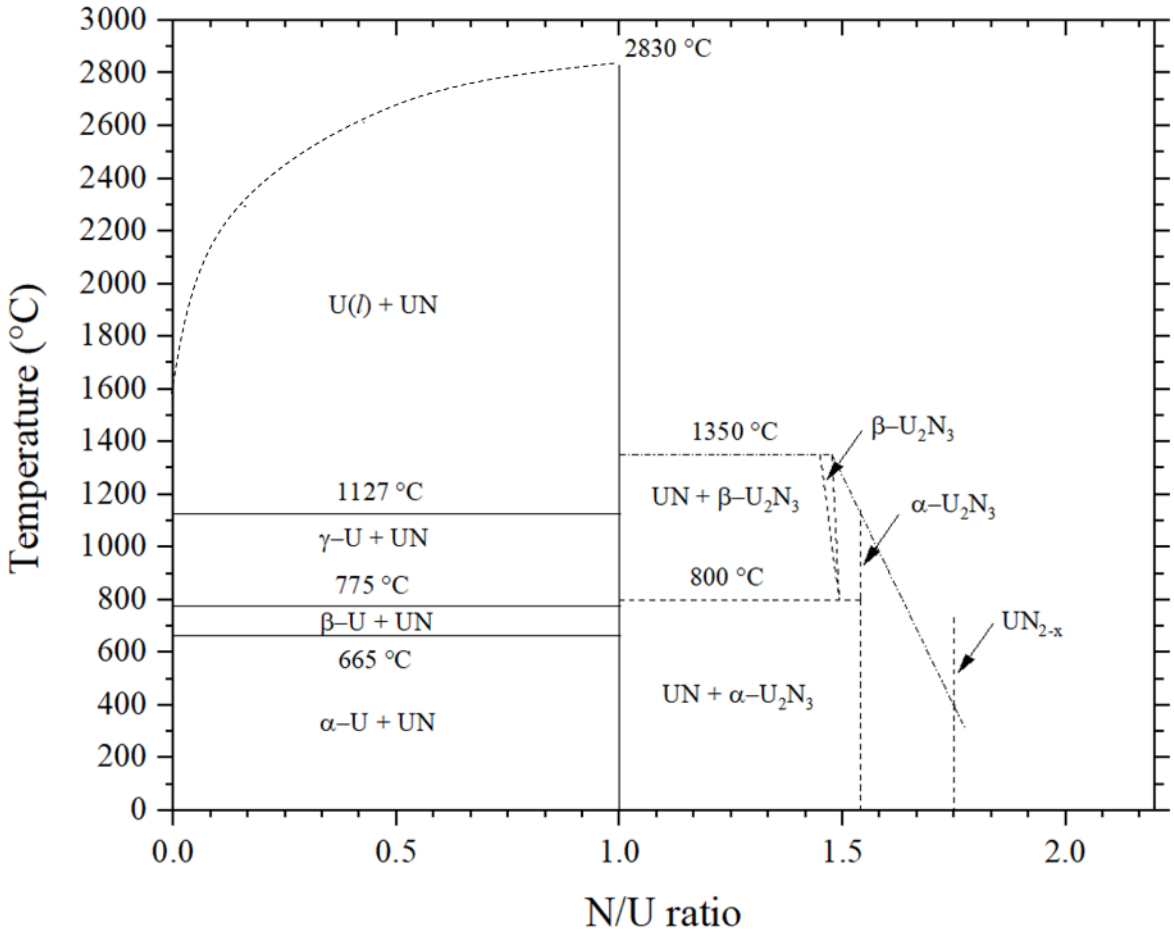

Figure 2-1. Uranium-nitrogen binary phase diagram (reproduced from H. Tagawa [57])

Table 2-1. Crystal structure and theoretical density of stoichiometric uranium nitrides

	UN	α-U_2N_3	β-U_2N_3	UN_2
Crystal structure	NaCl-type	Mn_2O_3-type	La_2O_3-type	CaF_2-type
Space group	Fm-3m	Ia3	P-3m1	Fm-3m
Theoretical density (g/cm^3)	14.33	11.35	12.63	12.02
Reference	[48] [50]	[51]	[52]	[48]

2.1.2. Thermal properties

Figure 2-2 shows the thermal conductivity of UN fuels compared with various representative fuels including U-Zr alloys, UO_2, UC, and U_3Si_2. The UO_2 fuel exhibits considerably low thermal conductivity than other fuels. The heat transfer mechanism of UO_2 is dominated by the phonon conduction up to 1773 °C [66]. The anharmonic phonon scattering due to the mass difference of U^{4+} (cation) and O^{2-} (anion) mainly contributes to the low thermal conductivity of UO_2. Furthermore, these anharmonic phonon scattering rate rapidly decreases as temperature increases [67]. Therefore, the thermal conductivity of UO_2 decreases as temperature increases. The low thermal conductivity causes significantly elevated fuel temperature; however, it was acceptable due to its high melting point of 2865 °C. On the other hand, U-Zr alloy fuels exhibit higher thermal conductivity than ceramic fuels. In general, the thermal transport in U-Zr alloys is attributed by free electrons rather than phonons [68]. Thus, the thermal conductivity of U-Zr increases with increasing temperature. Ogata [46] reported the thermal conductivity of U-Zr alloys as a function of temperature and composition as follows:

$$k = 16.309 + 0.0271 \times T - 46.27 \times C_{Zr} + 22.985 \times C_{Zr}^{\ 2} \tag{2-6}$$

where k is thermal conductivity (W/K·m), T is temperature (K), and C_{Zr} is atomic fraction of Zr (at%). Equation 2-6 indicates that the thermal conductivity of U-Zr alloy is linearly proportional to temperature.

Remarkably, the UN has advantages over both UO_2 and U-Zr alloy fuels; it simultaneously has a high melting point and high thermal conductivity. Thermal conductivity of UN was given by Hayes [1] as follows:

$$k = 1.864 \times e^{-2.14P} \times T^{0.361} \tag{2-7}$$

where k is thermal conductivity (W/K·m), T is temperature (K), and P is porosity volume fraction (vol%).

The origin of the high thermal conductivity of UN has been reviewed in several studies [69–72]. Majority of studies reported that heat transfer mechanism of UN is dominated by the electronic conduction: Yin et al. [70] evaluated that UN exhibits strong electronic correlations from the first-principles calculations, whereas lattice thermal conductivity contribution on UN is very minor at 727 °C; Kurosaki et al. [69] also demonstrated that the electronic contribution is dominant in UN thermal transport from the molecular dynamics (MD) calculation. On the contrary, Webb and Charit [71] proposed that heat transport in UN is mainly determined by lattice vibrations (phonon transport) at temperatures ranging between 27 °C and 1727 °C.

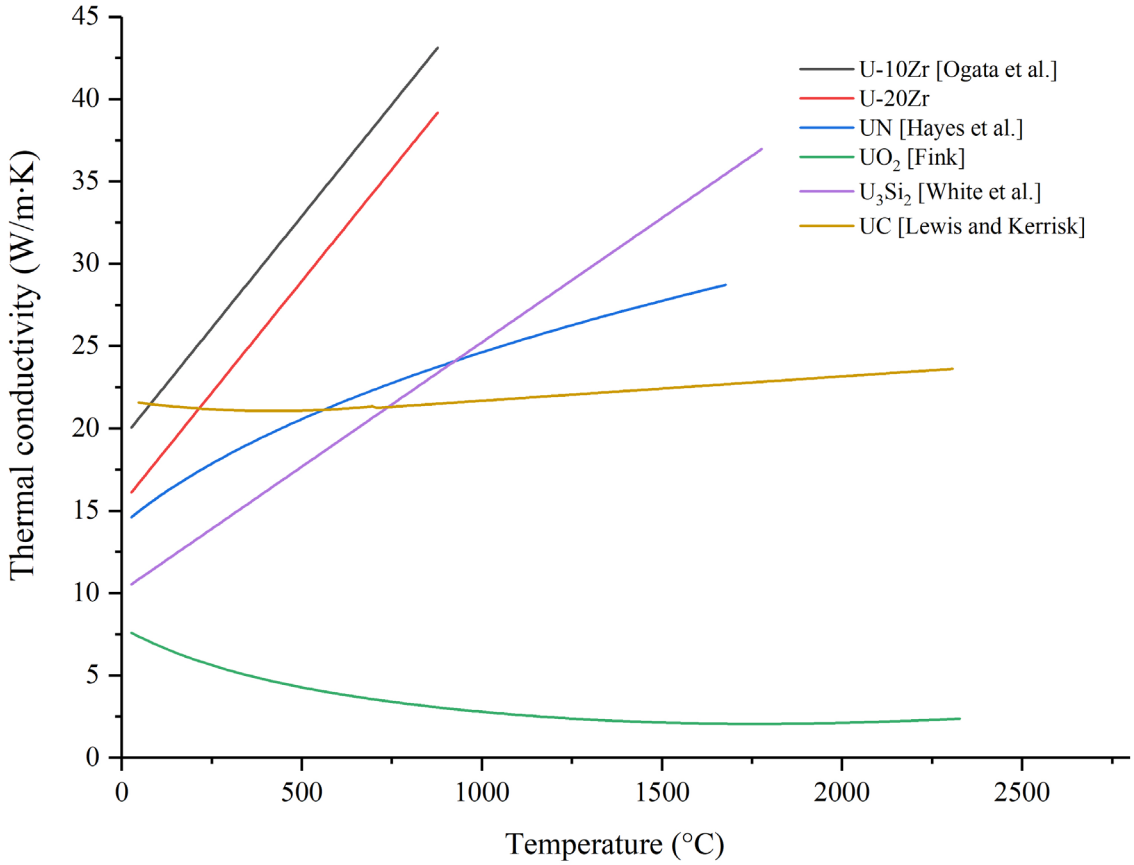

Figure 2-2. Thermal conductivity of representative nuclear fuels for comparison: U-10Zr and U-20Zr alloys from Ogata et al. [46], UN from Hayes et al. [1], UO_2 from Fink [4], U_3Si_2 from White et al. [47], and UC from Lewis and Kerrisk [45]

2.1.3. Irradiation behavior

Irradiation behavior of nuclear fuels is influenced by numerous variables, including burnup rate, temperature gradient, grain size, impurity, or stoichiometry of the fuel. For UN fuel, the effect of those variables has not been studied sufficiently; irradiation experiences of UN and uranium-plutonium mixed nitride (MNUP) have been very limited to ~200 fuel pins around the world, including the U.S., Russia, France, Japan, and the U.K. [73–79]. In the previous tests, the linear heat generation rates (LHGR) were varied from 350 to 1300 W/cm and the density of the fuel was ranged from 83 %TD to 95 %TD. Up to now, the maximum burnup of ~12 at% under the LHGR of 545 W/cm has been achieved for $(U_{0.4}Pu_{0.6})N$ pellets with 85 %TD [76].

The results of those irradiation tests have consistently indicated that UN exhibits outstanding irradiation resistance than that of UO_2 fuel, being consistent with its superior thermophysical properties. Figure 2-3 shows the representative microstructures of mixed uranium-plutonium oxide (MOX) fuel and UN fuel, which were irradiated at similar conditions: Figure 2-3a shows MOX pellet irradiated up to 110 GWd/MTU at 320 W/cm in EBR-II [79]; Figure 2-3b shows UN pellet irradiated up to 110 GWd/MTU at 545 W/cm in BOR-60 [76]. Severe microstructural degradation was not observed in the nitride fuels except several cracks formed at the periphery region, while MOX fuel showed the formation of the central hole, large gas bubbles, and cracks.

With those in mind, this section is to briefly describe the two representative irradiation behavior of UN fuel, namely, irradiation swelling and fission gas release compared with those of UO_2 fuel.

2.1.3.1. Swelling

The study by Matthews et al. [12] revealed that the higher-density and larger-grained UN fuel were more resistant to swelling. The UN fuel pellet with 87 %TD showed 8.9 vol% swelling during 0.74 at% burnup, while the pellet density of 95 %TD showed only ~2 vol% swelling rate at the same burnup. This indicates that high-density and larger-grained structure are strongly preferred to ensure the swelling resistance of UN fuel.

Other than high-density and larger-grained fuel pellets, lower smear density (the fraction of

fuel cross-sectional area inside cladding multiplied with fuel density in %TD unit) would enhance the fuel swelling resistance. Tanaka et al. [74] employed low-density (U,Pu)N fuels (84–86 %TD) with ~80% smear density to mitigate the fuel cladding mechanical interaction (FCMI). In these fuels, He fill gas was used to compensate the gap conductance decrease. Their irradiation results revealed that the fuel pins irradiated at 750 W/m to 4.3 at% burnup showed only 1.6–1.8 vol%/at% swelling. It sould be noted that the optimized smear density should be found because the large gap would increase the fuel temperature,

Althought the high temperature would promote fuel swelling, its effects have not been fully investigated yet. This is mainly due to the inconsistency of the swelling data available: the swelling rates of UN fuels irradiated under similar conditions was varied up to ± 300% [31,32]. Ross et al. [80] proposed the UN swelling model based on previous results in high temperature regions from 927 to 1327 °C; however, the uncertainty of his correlation was as high as ± 60% compared to the experimental data.

2.1.3.2. Fission gas release

In a typical LWR fuel system, a fuel pellet is the first barrier to fission gas release (FGR). The released fission gas to the fuel-cladding gap would decrease the gap conductance between the fuel and the cladding, and it thus increases fuel centerline temperature and internal pressure of discharged fuel rods. Nonetheless, the FGR mechanisms of ceramic nuclear fuels have hardly been understood, even for the conventional UO_2 fuel with decades of operating experience. This is mainly because FGR of fuels are affected by numerous material properties and operating parameters, which include fuel temperature, initial fuel porosity size and distribution, fuel density, burnup rate, and so on [81].

For UO_2 fuels, the FGR is typically less than 0.5% at ~3 at% burnup [82]. With increasing burnup, the FGR steadily increased to ~ 2.5% at ~5.5 at% burnup [82]. Further increase of burnup rate raises the FGR significantly: 23% was obtained when pellet average burnup reached 10 at% and 42% for 12 at% burnup [83]. In addition, the FGR is highly dependent on the fuel temperature. The irradiation test in Halden reactor [81] revealed FGR onset temperature is ~1000 °C; ~47% FGR was observed from 5 at% burnup pellets when a fuel centerline temperature exceeded 1000 °C.

The fission gas release rate of UN fuel showed similar values to those of UO_2 (or MOX) fuel. According to Storms [73], fission gas release rate for UN is suggested as follows:

$$R = \frac{100}{\exp\left(0.0025\left(\frac{90\rho_{TD}^{\ 0.77}}{B^{0.09}} - T\right)\right) + 1} \tag{2-8}$$

where R is fission gas release rate (%), ρ_{TD} is theoretical density (%), B is burnup rate (at%), and T is temperature in Kelvin. Thus, according to Equation 2-8, only 5% of FGR is expected at 10 at% burnup under 1000 °C. Considering the fuel centerline temperature of UN fuel would be much lower than oxide fuels due to its high thermal conductivity, considerably lower FGR is expected.

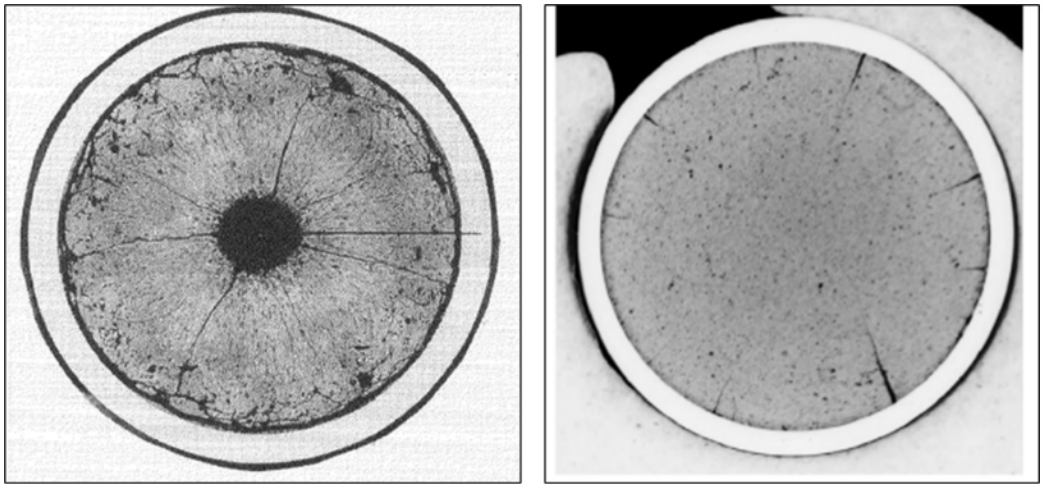

Figure 2-3. (a) MOX fuel irradiated in EBR-II up to 110 GWd/t(U) at a linear heat generation rate of 32 kW/m [79], (b) UN fuel irradiated in BOR-60 up to 110 GWd/t(U) at a linear heat generation rate of 54.5 kW/m [76]

2.2. Fabrication of nitride fuels

2.2.1. UN powder synthesis

By and large, the densification and microstructural development of ceramics are strongly affected by the characteristics of the starting powder, such as particle morphology, size, and size distribution; these factors are, in turn, dependent on powder synthesis methods and conditions. In this section, various techniques for stoichiometric UN powder synthesis are reviewed in brief.

2.2.1.1. Carbothermic reduction

The carbothermic reduction process has been most widely used to prepare the UN powder [84–89]. The method is based on the following reaction:

$$UO_2(s) + 2C(s) + 1/2N_2(g) \rightarrow UN + 2CO \quad (2\text{-}9)$$

In the above reaction, the UO_2-C mixed power is heated under N_2 gas atmosphere at around 1500–1700 °C. At first, this method has received interest for its potential application in the mass production of the UN powder because the process uses UO_2 as a starting material, whose commercial production systems have already been well established, namely, through the ammonium diuranate (ADU), ammonium uranyl carbonate (AUC), or dry conversion (DC) processes. However, several disadvantages have been found during the practical application. Firstly, the presence of un-reacted UO_2 powder was inevitable with the initial carbon to dioxide mixing molar ratio (C/UO_2) of 2.0 because this technique is basically based on the solid-state reaction. To resolve this issue, additional carbon has been added to nitrify the UO_2 power fully. The C/UO_2 mixing ratio was chosen from 2.2 to 2.5 [89], but under these carbon-rich conditions the uranium carbonitride phase, $U(N_{1-x},C_x)$, was formed as follows:

$$UO_2(s) + (2+x)C(s) + (1-y)/2N_2(g) \rightarrow U(N_{1-y}, C_y) + 2CO + (x-y)C \quad (2\text{-}10)$$

Eventually, to remove such carbon impurities and carbonitride phases shown in Equation 2-10,

post-processes of hydrogen-reduction and nitridation [86] have to be followed as below:

$$(x-y)C + 2(x-y)H_2 \rightarrow (x-y)CH_4 \quad (2\text{-}11)$$

$$U(N_{1-y}, C_y) + 1/2\,yN_2 \rightarrow UN + yC \quad (2\text{-}12)$$

The hydrogen reduction process given in Equation 2-11 requires a reaction temperature between 1000–1200 °C and the nitride process in Equation 2-12 requires 1500–1700 °C. These extra procedures with high reaction temperatures are now considered as the main drawback of the carbothermic reduction method.

2.2.1.2. Hydride-nitride process

Hydride-nitride process has also been widely used for synthesis of lanthanide or actinide nitride powders [12,37,39,85,88,90–93], usually in a laboratory-scale. This process is conducted at relatively lower reaction temperature (< 1300 °C) than the carbothermic reduction method (> 1500 °C) described in the previous section. The reaction sequences are as follows:

$$U(s) + 3/2H_2(g) \leftrightarrow UH_3(s) \quad (2\text{-}13)$$

$$2UH_3(s) + 3/2N_2(s) \rightarrow U_2N_3(s) + 3H_2(g) \quad (2\text{-}14)$$

$$U_2N_3(\mathrm{s}) \rightarrow 2UN(\mathrm{s}) + 1/2N_2(\mathrm{g}) \quad (2\text{-}15)$$

Firstly, uranium metal is heated under pure hydrogen at 225–235 °C, forming UH_3 as shown in Equation 2-13. Due to the oxidation sensitive nature of both metal samples and UH_3 powder, all processes must be carried out in an inert gas-filled glove box. The several hours of heating are required depending on the mass to volume ratio of the sample loaded, e.g., it took 4 h for a small piece of metal (15 g) [93], but 16 h for a large ingot (100 g) [85]. The UH_3 powder is then heated under the pure N_2 atmosphere as described in Equation 2-14. This reaction is normally completed within 1 h at 300–500 °C due to the high reactive nature of the UH_3 with N_2 gas. After then, the U_2N_3 powder is decomposed to UN at 1300 °C under inert atmosphere following Equation 2-15. The hydride-nitride

process includes no additives in the system; therefore, the quality of the UN powder has been demonstrated to be superior in terms of impurity levels.

2.2.1.3. Direct nitridation of uranium metal

Speidel and Keller [90] revealed that the direct nitridation of the uranium metal is possible by heating uranium metal in pure N_2 atmosphere. The uranium metal, heated at 850 °C under N_2 atmosphere, is converted to a nitride with a composition between U_2N_3 and UN_2 (see Equation 2-16). However, compared to the hydride-nitride process described in the previous section, the direct nitridation process requires significantly longer reaction time. The time was lengthened up to 65 h to fully nitrify a piece of uranium metal. For a small sample (0.6 × 0.6 × 0.3 mm), it normally takes ~15 h to complete the reaction. The U_2N_{3+x} powder then decomposes to UN under inert atmosphere at 1300 °C. The particle size of UN powder synthesized by direct nitridation process was larger (80 mesh, i.e., < 177 μm) than that of UN powder by hydride-nitride method (325 mesh, i.e., < 45 μm).

$$2U(s) + (3+x)/2N_2(g) \leftrightarrow U_2N_{3+x}(s) \quad (2\text{-}16)$$

$$U_2N_{3+x}(\mathrm{s}) \rightarrow 2UN(\mathrm{s}) + (1+x)/2N_2(\mathrm{g}) \quad (2\text{-}17)$$

2.2.1.4. Ammonolysis of uranium fluoride

Ammonolysis of uranium fluoride process was first proposed by Yeamans et al. [94]. They successfully synthesized the UN powder from UO_2 by following sequence of reactions:

$$UO_2 + 4NH_4HF_2 \rightarrow (NH_4)_4UF_8 + 2H_2O \quad (2\text{-}18)$$

$$(NH_4)_4UF_8 + 6NH_3 \rightarrow UN_2 + 8NH_4F + H_2 \quad (2\text{-}19)$$

$$2UN_2 \rightarrow U_2N_3 + 1/2N_2 \quad (2\text{-}20)$$

$$U_2N_3 \rightarrow 2UN + 1/2N_2 \quad (2\text{-}21)$$

The UO_2 powder is reacted with solid ammonium bifluoride, $NH_3(HF)_2$, at ambient temperature as shown in Equation 2-18, which produces ammonium uranium fluoride, $(NH_4)_4UF_8$. Afterward, the $(NH_4)_4UF_8$ reacts with NH_3 at 700 °C and is converted to UN_2. The UN_2 is then decomposed to U_2N_3 and UN at 1100–1200 °C under Ar atmosphere. This method has the advantage of relatively low-temperature processing compared to the previously mentioned methods.

2.2.1.5. Ammonolysis of UF_4

Ammonolysis of UF_4 has been proposed by Silva et al. [55,95]. The synthesis process is as follows:

$$UF_4 + 6NH_3 \rightarrow UN_2 + 4NH_4F + H_2 \quad . \quad (2\text{-}22)$$

The UF_4 powder is heated under an ammonia atmosphere at lower processing temperature of 800 °C and converted to UN_2 powder directly. The synthesized UN_2 power is then decomposed to the UN powder under inert atmosphere at 1100 °C. Notably, this method is considered to be the most practicable process for commercial-scale UN powder production, because the UF_4 is the intermediate product of the conventional reconversion process (UF_6 to UO_2).

2.2.2. UN pellet fabrication

As mentioned in Section 2.1.3., high-density pellet is required to enhance the swelling resistance of UN fuel. The UN powder, however, exhibits a poor sinterability than oxide or carbide powder due to the low diffusivity of uranium ions in UN. To compensate for its low sinterability, extremely high sintering temperature has to be applied, and this eventually increases the fuel fabrication

cost significantly. Thus, a proper fabrication technique needs to be established for economic fuel fabrication. This section is to describe the sintering methods applicable for the UN fuel fabrication.

2.2.2.1. Conventional sintering (CS)

The CS method, also known as cold-press sintering, consists of two processes: powder compaction and heating. This method has been used to fabricate the UN fuel pellets [90,91,93,96–98]; however, high pellet density was hardly achieved due to its low sintering capability. During the early development of UN fuels in 1960s, Evans and Davies [93] have concluded that 75 %TD would be the maximum density obtainable by the CS. The improvement of powder quality afterward enabled to increase the maximum obtainable value up to 90 %TD [98]. In addition, Tennery et al. [91] further investigated the sinterability of UN as a function of the N_2 pressure and revealed that sinterability could be further enhanced by employing high N_2 pressure: UN pellets sintered at 1600 °C under N_2 pressure of 2.2×10^{-7} atm achieved 75 %TD, while 85 %TD was achieved under 1.5 atm at the same temperature.

Nevertheless, a significantly high sintering temperature is still required to achieve high-density pellets using CS. To achieve over 90 %TD, a higher temperature than 2000 °C is required under 1 atm N_2 pressure. So far, 94 %TD was the largest density obtained from CS, which was conducted at 2100 °C for 2 h under 1.5 atm N_2 pressure [91].

For MNUP fuel, however, a relatively low sintering temperature is required to obtain a high-density pellet due to the high diffusivity of plutonium. Arai [94] reported 94 %TD achieved after 5 h CS at 1750 °C under Ar-8%H_2 atmosphere.

2.2.2.2. Hot-pressing technique

The hot-pressing (HP) technique has been used to overcome the low sinterability of CS technique. Isostatic pressure is applied during the heating enhances the pore removal process, and thus powder agglomerates more rapidly compared to CS. For UN fuel, the hot-pressing technology was first adopted by Evans and Davies [93]. They successfully fabricated the high-density UN fuels (98 %TD) at 1000 °C for 4 h under 25–30 MPa. A similar study was also conducted by Spidel and Keller [90]. In their study high-density UN fuels (97 %TD) were fabricated at 1480–1580 °C for 3 h under 69 MPa;

however, the presence of oxide and nitride, UO_2 and U_2N_{3+x} phases, throughout the UN matrix were problematic.

The effect of the sintering pressure on the densification of UN and MNUP was investigated by Chang [99]. In his study, density of pure UN pellets sintered at 1400 °C for 90 min was increased from 86 to 97 %TD, corresponding to sintering pressure increase from 17 to 43 MPa. A similar tendency was presented in UN-20wt%PuN pellets despite the presence of plutonium enhancing the sinterability. The pellet density increased from 94 to 99 %TD with increasing pressure from 21 to 28 MPa at 1400 °C for 90 min.

2.2.2.3. Spark plasma sintering

The SPS is one of the HP technologies; however, this method is distinguished by the use of spark plasma, which is driven by pulsed high-energy DC current passing through the powder inside graphite molds. This spark plasma generates intensive heat and thus bonds the particles together very rapidly and uniformly. Although the fundamental principle of SPS was first proposed 50 years ago [100], its application on the UN was first considered about 15 years ago [23,36–42].

Up to now, SPS has partially demonstrated superior sintering performances for both pure and composite UN pellets. The high density (> 99 %TD) with low porosity (0.2 %) UN pellets have been fabricated by Pertti [37] under the SPS conditions of 1650 °C and 3 min. Moreover, the UN composite pellets of UN/U_3Si_2 [40,41], UN/ThN [42], and UN/UO_2 [23] have been fabricated using SPS. According to Hiroaki [36], the degradation of thermal and mechanical properties from fast densification was not observed in SPSed UN pellets compared to conventionally sintered UN pellets. The effects of sintering conditions on the microstructure of SPSed UN pellets have only been investigated by Kyle [38,39]. In the studies, sintering temperature was varied from 1450 to 1650 °C under the pressure of 45–135 MPa with holding time from 2 to 15 min.

2.3. Burnable absorber

For typical LWRs, to suppress the excess reactivity at BOC and to minimize the reactivity swing over the cycle, a boron compound is dissolved in the primary coolant; however, its concentration is limited below ~1300 ppm to secure the negative moderator void coefficient (MVC). To compensate the remnant excess reactivity, BA elements are additionally loaded in fuel pins. Thus, the selection of proper BA material and its configuration is essential to enhance the fuel performance and safety during reactor operation. This section is to present the BA element candidates for UN fuel and their effects on the fuel thermal property degradation.

2.3.1. Burnable absorber element candidates

The initial negative reactivity, which is given by BA at the BOC, has to be minimized at the end of cycle (EOC) to secure the long fuel cycle. Thus, the burnout rate is the most crucial factor during the selection of the burnable absorber element. Rare earth elements including, samarium (Sm), europium (Eu), gadolinium (Gd), dysprosium (Dy), and erbium (Er) are known to have high burnout rates under the thermal spectrum. Table 2-2 summarized the general properties of those candidates. The study conducted by Asou et al. [101] reported that, among the rare earth candidates, Gd and Er are more applicable as burnable absorbers for typical PWRs because Sm, Eu, and Dy have relatively long decay chains where daughter isotopes have considerable thermal neutron absorption cross sections.

In commercial LWRs, Gd is widely used due to its high thermal neutron absorption cross-section. For this purpose, Gd_2O_3 is homogeneously mixed in the UO_2 pellets and forms a solid-solution $(U_{1-x},Gd_x)O_2$ phase. Galahom [102] revealed that Er is more applicable for a long fuel cycle since it depleted slower than gadolinium because of its relatively low thermal neutron absorption cross-section. For this reason, Er BA has been adopted for System 80+ reactor [103], a PWR type reactor loaded by MOX fuel with a long refueling cycle of 24 months.

Table 2-2. General properties of burnable absorber elements [101]

	Element				
	Gd	Sm	Eu	Dy	Er
Natural abundance (g/tons)	6.36	6.47	1.06	4.47	2.47
Average thermal cross section (barns)	40,000 ± 100	5800 ± 100	4600 ± 100	930 ± 20	162 ± 8
Average resonance integral (barns)	390 ± 10	1400 ± 200	2430 ± 200	1600 ± 200	740 ± 10
Number of absorber isotopes	2 (^{155}Gd, ^{157} Gd)	2 (^{149}Sm, ^{151}Sm)	4 (^{151}Eu,^{152}Eu,^{154}Eu,^{155}Eu)	2 (^{164}Dy, ^{165}Dy)	1 (^{167}Er)

2.3.2. Burnable absorber configurations

In addition to the elements, the neutronic performance of BA is strongly affected by its configuration. Renier et al. [104], for example, compared the four types of conceivable Gd_2O_3 BA configurations:

1. Homogeneously mixed with the fuels
2. Mixed with only the outer one-third of fuel pellets
3. Coated on the perimeter of the fuel pellets
4. Alloyed with the cladding.

A comparison of the above four configurations revealed that outer one-third volume mixing of Gd_2O_3 with UO_2 fuel (*case 2*) shows the most effective neutronic performance followed by homogeneously mixed pellets (*case 1*): the residual negative reactivity of the *case 1* configuration was $\sim 2 \times 10^{-3}$ $\Delta k_{eff}/k_{eff}$ and that of *case 2* was $\sim 0.5 \times 10^{-3}$ $\Delta k_{eff}/k_{eff}$ after 4 years operation at full power of 3400 MWth (17.6 MWth per fuel assembly). This implies that the amount of BA compound added in fuels could be reduced by adopting the configuration of the *case 2*; however, from the viewpoint of the fuel fabrication cost, a homogeneous configuration of the *case 1* would be more practical.

2.3.3. Effect of BA presence on fuel thermal conductivity

The presence of BA elements tends to degrade fuel thermal conductivity; therefore, a reliable thermophysical data for the BA added fuels is essential to estimate the fuel temperature correctly and to ensure core safety during the operation. For traditional UO_2 fuels, the effects of Gd_2O_3 additive on the fuel thermal properties have been widely investigated [105–108]; however, for UN fuels, those effects have never been investigated so far. With a lack of data available, to estimate the achievable power uprates and corresponding fuel temperature changes in LWR with UN fuels, Giudicelli [13] calculated the effective thermal conductivity of gadolinium compounds added UN fuel on the basis of the following assumption:

$$\frac{\lambda_{UO_2-Gd_2O_3}(C_{Gd_2O_3},\ T)}{\lambda_{UO_2-Gd_2O_3}(C_{Gd_2O_3}=0,\ T)}=\frac{\lambda_{UO_2-GdN}(C_{GdN},\ T)}{\lambda_{UO_2-GdN}(C_{GdN}=0,\ T)} \tag{2-23}$$

where $\lambda_{UO_2-Gd_2O_3}$ and λ_{UO_2-GdN} are thermal conductivities of UO_2-Gd_2O_3 and UN-GdN mixed pellets, C is weight fraction (wt%) of Gd compounds, and T is temperature (K).

However, this assumption would not be valid because the heat transfer mechanism of UO_2 completely differs from that of UN. As briefly mentioned in Section 2.1.2, the heat transfer mechanism of UO_2 is dominated by phonon conduction. This phonon conduction is presented as follows:

$$\lambda=\frac{1}{A+BT} \tag{2-24}$$

where λ is thermal conductivity, T is temperature, and A and B is constant. Based on Equation 2-24, Massih et al. [105] suggested thermal conductivity of Gd_2O_3 mixed UO_2 fuel as follows:

$$\lambda=\frac{1-\beta(1-\rho_{TD})}{1-\beta(1-0.95)}\cdot\left[\frac{1}{A+a_0x_{Gd_2O_3}+BT}+C\exp(dT)\right] \tag{2-25}$$

where $x_{Gd_2O_3}$ is weight fraction of Gd_2O_3, T is the temperature in °C, ρ_{TD} is the fraction of theoretical density, β = 2.58 - 0.58T, A = 0.1149, a_0 = 1.1599, B = 2.48×10^{-4}, C = 0.01216, and d = 0.001867. Equation 2-25 presented that the thermal conductivity decreases with increasing gadolinium contents, while the decreasing rate becomes smaller at higher temperatures.

On the contrary, the thermal conductivity of UN is dominated by electronic conduction as previously described in Section 2.1.2. Therefore, a thermal conductivity degradation behavior of UN rather follows that of the metallic fuels as shown in Equation 2-6. Unfortunately, no experimental study has been conducted to measure the UN thermal conductivity degradation rate by addition of nitride compounds.

Chapter 3. EXPERIMENTAL

3.1. Sample preparation

3.1.1. Powder synthesis

3.1.1.1. Pure UN powder

The UN powder was synthesized from depleted uranium (DU) metal (shown in Figure 3-3a) using the hydride-nitride process (described in Section 2.2.1.2.). Specific procedures and conditions are presented in Figure 3-2. Prior to the synthesis, the thin UO_2 layer (brownish) on the metal surface was removed using nitric acid (60 %). The as-cleaned DU chunk (shown in Figure 3-3b) was placed in an alumina crucible and loaded into the air-tight furnace connected to the glove box (see Figure 3-1) filled with high purity Ar (oxygen < 5 ppm). After the sample loading, the furnace chamber was evacuated by a rotary pump and refilled with high-purity H_2 (99.999%). The furnace was heated to 235 °C for 4 h with H_2 flow rate of 50 mL/min. Following the reaction in Equation 2-13, the metal was converted into UH_3 and simultaneously shattered into tiny pieces due to significant volume expansion during the phase transformation from U (19.05 g/cm^3) to UH_3 (10.95 g/cm^3). The shattered UH_3 pieces were ground into fine black powder (see Figure 3-3c) using an agate mortar for 15 min. It was noted that UH_3 was easily pulverized because it is sufficiently brittle. The as-pulverized UH_3 powder is loaded in an alumina crucible and again placed in the furnace. The furnace was heated up to 500 °C under N_2 atmosphere with a flow rate of 1 L/min, which was quickly (< 30 min) completed since the reaction given by Equation 2-10 is highly reactive. Following the reaction in Equation 2-15, the U_2N_3 powder was decomposed to the dark-grey UN powder (see Figure 3-3d) at 1200 °C for 8 h under Ar atmosphere with a flow rate of 1 L/min. The particle sizes of as-synthesized UN powder (shown in Figure 3-4) were ranged from 1 to 20 μm with an average size of ~6.0 ± 4.9 μm.

Figure 3-1. Apparatus of the glove box (right) and attached furnace (left)

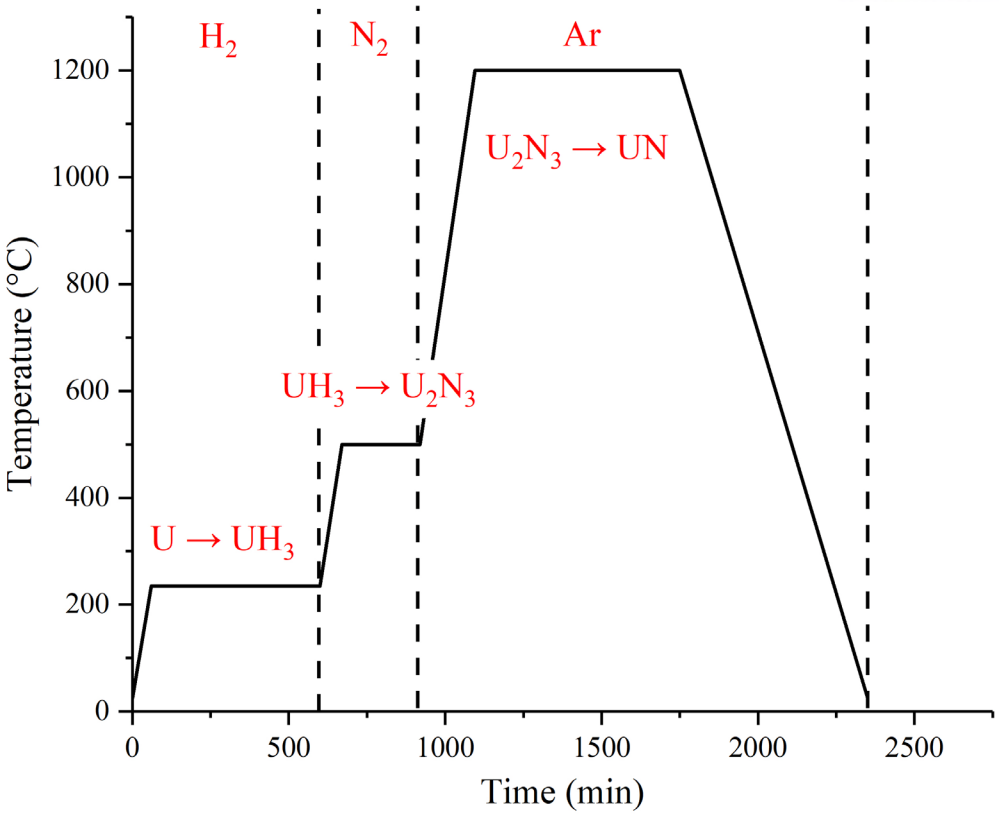

Figure 3-2. Hydride-nitride procedures and conditions for UN power synthesis

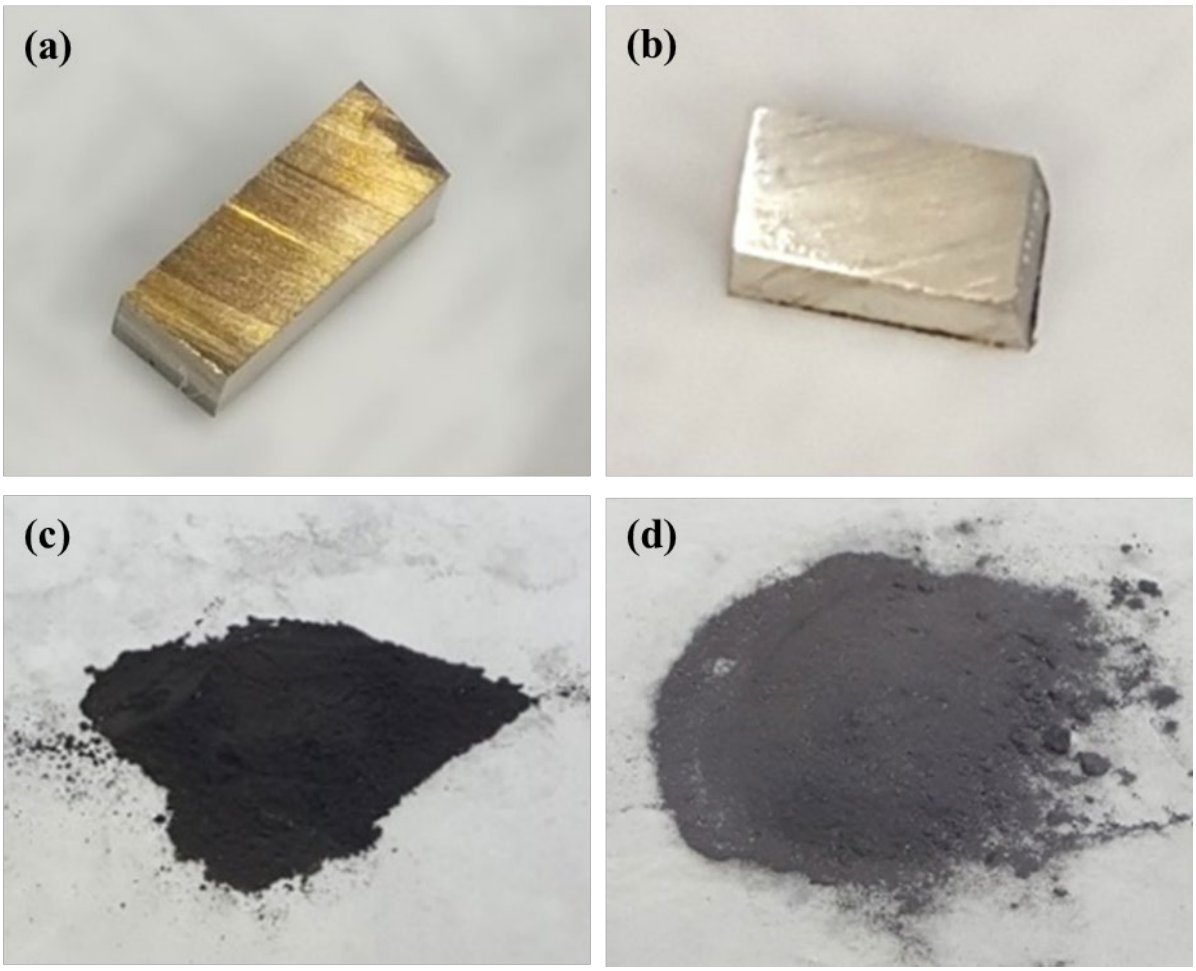

Figure 3-3. Visual images of (a) uncleaned U metal, (b) cleaned DU metal (c) ground UH_3 powder, and (d) as-synthesized UN powder

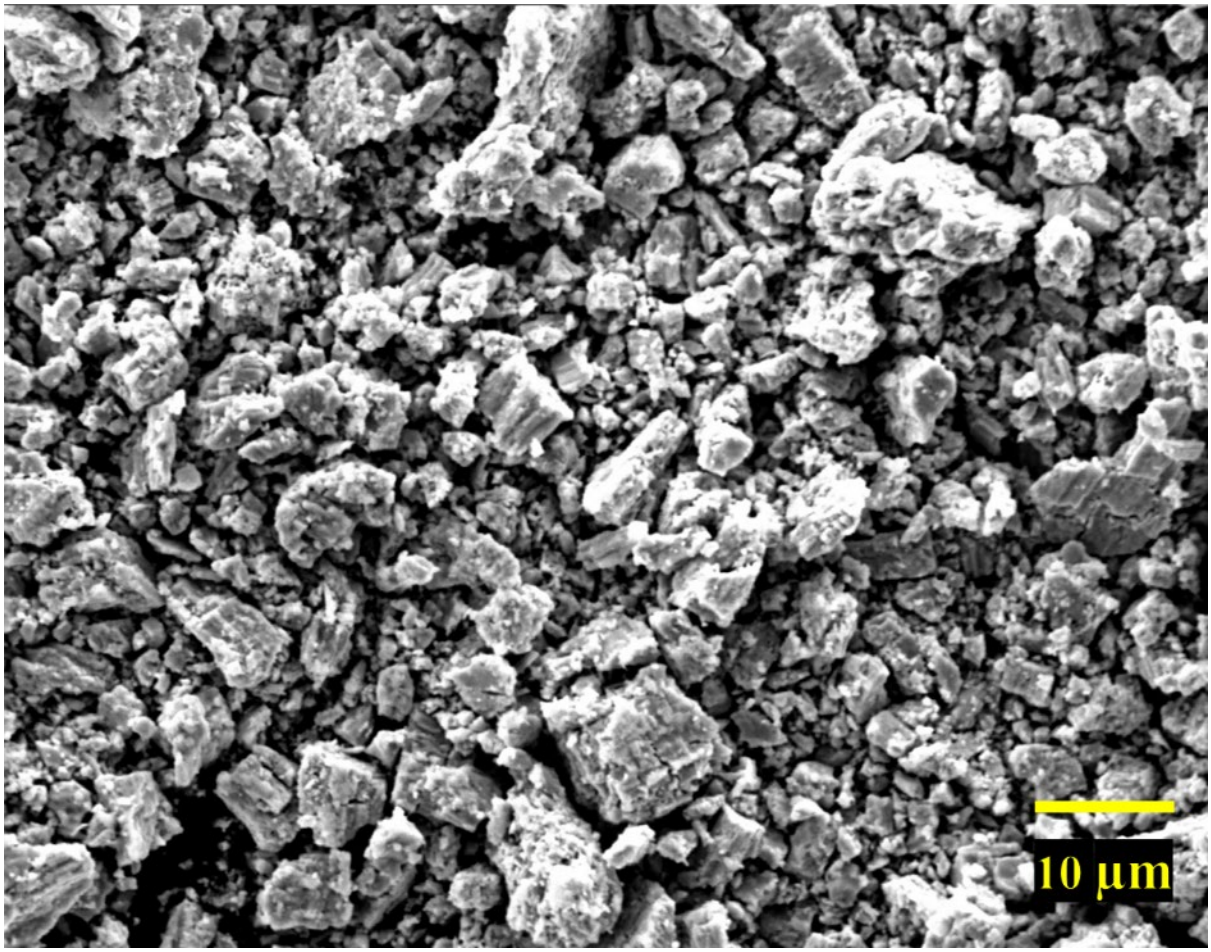

Figure 3-4. SEM image of the as-synthesized UN power

3.1.1.2. GdN and Gd_2O_3 powder

The GdN powder was synthesized from commercial-grade Gd metal (99.9%, Alfa Aesar) through the hydride-nitride method. The process conditions were slightly modified from those used in the previous UN powder synthesis. A piece of Gd metal was placed in an Ar-filled glove box with low oxygen level (< 5 ppm) to mitigate the surface oxidation. A gadolinium piece was contained in alumina crucible and loaded in the furnace connected to the glove box. The furnace was filled with pure H_2 (99.999 %) after the evacuation. The metal sample was heated to 230 °C for 4 h under H_2 atmosphere with a flow rate of 50 mL/min. This process produced shattered GdH_3 powder. After then, the powder was ground manually for 15 min using an agate mortar. The as-ground GdH_3 powder was then loaded in the furnace and heated at 500 °C under N_2 atmosphere. In this case, the de-nitride process was unnecessary since GdN is the only stoichiometric component formed in the Gd-N system.

On the contrary, the commercial-grade Gd_2O_3 powder was purchased from Alfa Aesar (99.9%, < 10 μm).

3.1.2. Spark plasma sintering

The pure and gadolinium compounds added UN powders (UN/GdN and UN/Gd_2O_3) were fabricated using SPS (DrSinter, SPS-211LX) shown in Figure 3-5. The powder was loaded inside the graphite mold assembly, which consisted of a graphite cylinder die (30.0 mm outer diameter, 10.5 mm inner diameter, and 30 mm height) and a pair of graphite punches (10.0 mm diameter and 20.0 mm height). A schematic illustration of the graphite assembly is shown in Figure 3-6. To reduce the heat loss from the mold and to decrease the temperature gradient inside, the mold assembly was covered with 3 mm graphite felt. Additionally, a thin (0.2 mm) graphite sheet was positioned between the powder and the die to prevent an unexpected reaction between a sample and a mold. The heating and cooling rate were set to 100 K/min. Throughout the SPS process, the chamber pressure was maintained lower than 1 Pa to mitigate the sample oxidation. The temperature of the sample was continuously monitored using a pyrometer. To enhance the measurement accuracy, the pyrometer sighted near the sample through the hole drilled close to the sample surface (2 mm).

3.1.2.1. UN pellet fabrication

Various SPS times and temperatures were examined to investigate the effect of those parameters on the microstructure development of UN pellets under a uniaxial pressure of 70 MPa. Various sintering temperatures of 1500, 1600, 1700, and 1800 °C were first investigated for 10 and 60 min, respectively. After then, dwell times of 5, 30, and 180 min were further investigated at 1800 °C.

3.1.2.2. UN/Gd_2O_3 composite pellet fabrication

The UN/Gd_2O_3 mixed powders were prepared with the Gd_2O_3 fraction of 5, 10, and 15 wt%. To ensure homogeneous mixing, the mixed powders were blended in an agate mortar for 15 min inside the Ar glove box. The specific amount of UN and Gd_2O_3 are listed in Table 3-1. The mixed powders were sintered at 1800 °C for 10 min under a uniaxial pressure of 70 MPa. Notably, the pure Gd_2O_3 pellet was prepared at relatively low temperature of 1000 °C and 10 min because of the phase instability issue (described in Section 5.2.1).

3.1.2.3. UN/GdN composite pellet

Two sets of UN/GdN mixed powders were prepared with various GdN compositions of 3.5, 7.0, 10.7, 14.5, and 38.4 wt%. Table 3-2 and 3-3 show the specific amounts of mixed powder of UN and GdN, which were homogeneously mixed using an agate mortar for 15 min inside the glove box. Each set of powders was sintered under two different SPS conditions: 1800 °C for 10 min were used to prepare the non-solid-solution pellets; 2000 °C for 60 min were chosen to fabricate the solid-solution pellets. Pure GdN was prepared separately prepared at 1800 °C for 10 min. All samples were SPSed under a uniaxial pressure of 70 MPa.

3.1.3. Thermal etching

By and large, to reveal the microstructure of a UN pellet surface, the wet chemical etching technique is commonly used because of its simplicity and low cost. The major drawback of this method is the difficulty with handling (including disposal) of the toxic etchant consisting of nitric, lactic, and hydrofluoric acids [109], especially when it contains radioactive elements. To avoid the use of the toxic etchant, a thermal etching method was employed for the first time in this study. Although thermal etching has never been applied to UN, it has been demonstrated to be effective for other nitride compounds including titanium and aluminum nitrides (TiN and AlN) [110]. A nitrogen atmosphere, used in the previous study, however, is not applicable for UN due to the nitrification of UN to U_2N_3. Thus, various etching gas candidates, including pure Ar, H_2/Ar and CO/CO_2, were tested to find a suitable etching atmosphere. During the test, the oxygen sensor (C-100, Nano-ionics) was used to measure the oxygen partial pressure in the gases. It was revealed that Ar atmosphere with oxygen partial pressure (p_{O_2}) of 10^{-4} atm was effective for UN etching.

In addition to the pre-selected gas atmosphere, various heating temperatures from 1000 to 1400 °C and etching durations from 1 to 15 min, were examined to improve the etching quality. Since the thermal etching quality was highly sensitive to surfacial defects of the polished sample, such as scratches, dents, or cracks, the samples were carefully mirror-polished using diamond pastes with particle sizes down to 1.0 μm prior to the etching. Optimal etching conditions were found in ways to minimize the over-etched areas.

Eventually, all the UN pellets were thermally etched at 1100 °C with a heating rate of 5 °C/min. Etching durations were chosen mostly depending on pellet porosity, i.e., a shorter duration for higher porosity samples.

Table 3-1. Specification of UN/Gd_2O_3 mixed powder

Composite	UN (g)	Gd_2O_3 (g)	Composition	
			(at%)	(wt%)
UN + 5wt%Gd_2O_3	3.2312	0.1695	6.8	5.0
UN + 10wt%Gd_2O_3	3.0628	0.3387	12.5	10.0
UN + 15wt%Gd_2O_3	2.8886	0.5123	15.7	15.1

Table 3-2. Specification of UN/GdN mixed powder SPSed at 1800 °C

Composite	UN (g)	GdN (g)	Composition	
			(at%)	(wt%)
UN + 3.5wt%Gd_2O_3	3.2827	0.1183	5.0	3.5
UN + 7.0wt%Gd_2O_3	3.1625	0.2395	10.0	7.0
UN + 10.7wt%Gd_2O_3	3.0340	0.3642	15.0	10.7
UN + 14.5wt%Gd_2O_3	2.9037	0.4930	20.0	14.5
UN + 38.4wt%Gd_2O_3	2.0978	1.3083	47.9	38.4

Table 3-3. Specification of UN/GdN mixed powder SPSed at 2000 °C.

Composite	UN (g)	GdN (g)	Composition	
			(at%)	(wt%)
UN + 3.5wt%Gd_2O_3	3.3342	0.1202	5.0	3.5
UN + 7.0wt%Gd_2O_3	3.2122	0.2433	10.0	7.0
UN + 10.7wt%Gd_2O_3	3.0340	0.3642	15.0	10.7
UN + 14.5wt%Gd_2O_3	2.9125	0.4945	20.0	14.5
UN + 38.4wt%Gd_2O_3	2.0547	1.2814	47.9	38.4

Figure 3-5. Spark Plasma Sintering system (Dr. Sinter® SPS-212)

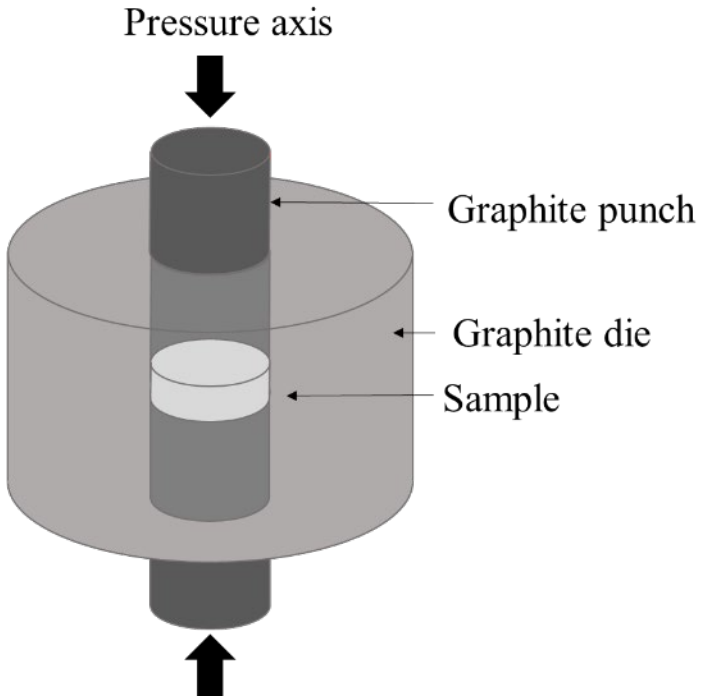

Figure 3-6. Schematics illustration of the graphite assembly

3.2. Sample characterization

3.2.1. Phase and microstructure analysis

3.2.1.1. X-ray diffraction analysis

The crystal structure of the as-synthesized powder and the sintered pellets was analyzed using the X-ray diffractometer (Rigaku, SmartLab SE) shown in Figure 3-7. The monochromatic Cu Kα radiation (λ = 1.54056 Å) was used, which was operated at 40 kV and 25 mA. Under the Bragg-Brentano geometry, X-ray diffraction (XRD) patterns were obtained in the 2θ range from 20 to 100 ° at a constant scanning rate of 2°/min. The lattice parameter of samples was calculated based on Bragg's Law as follows:

$$\lambda = 2d \sin\theta \tag{3-1}$$

The incident beam was aligned parallel to the surface of the samples. For this purpose, the direct-beam (2θ = 0) scanned the sample along the z-axis and was positioned to the height where the incident beam was cut in half. After z-axis adjustment, the direct-beam was rotated about the ω-axis, which is perpendicular to both z-axis and x-axis, until the beam was cut in half.

3.2.1.2. Scanning electron microscopy

The morphology of as-synthesized UN powder and pellets was observed using SEM (COXEM, EM-30ax plus). For better image quality, the powder sample was coated with a ~40 nm gold layer using the ion sputter coater (COXEM, SPT-20); however, for the sintered pellets, ion coating was not necessarily required due to the appreciable electric conductivity of the UN phase. The accelerating voltage of 20 kV was employed to observe thermally etched microstructures of pure UN pellets. The same voltage was applied for UN/GdN and UN/Gd_2O_3 mixed pellets; however, a backscatter electron (BSE) detector was used in this case to reveal the phase contrast between uranium and gadolinium compounds. The mean grain size of thermally etched samples was determined according to ASTM E112-13 [111].

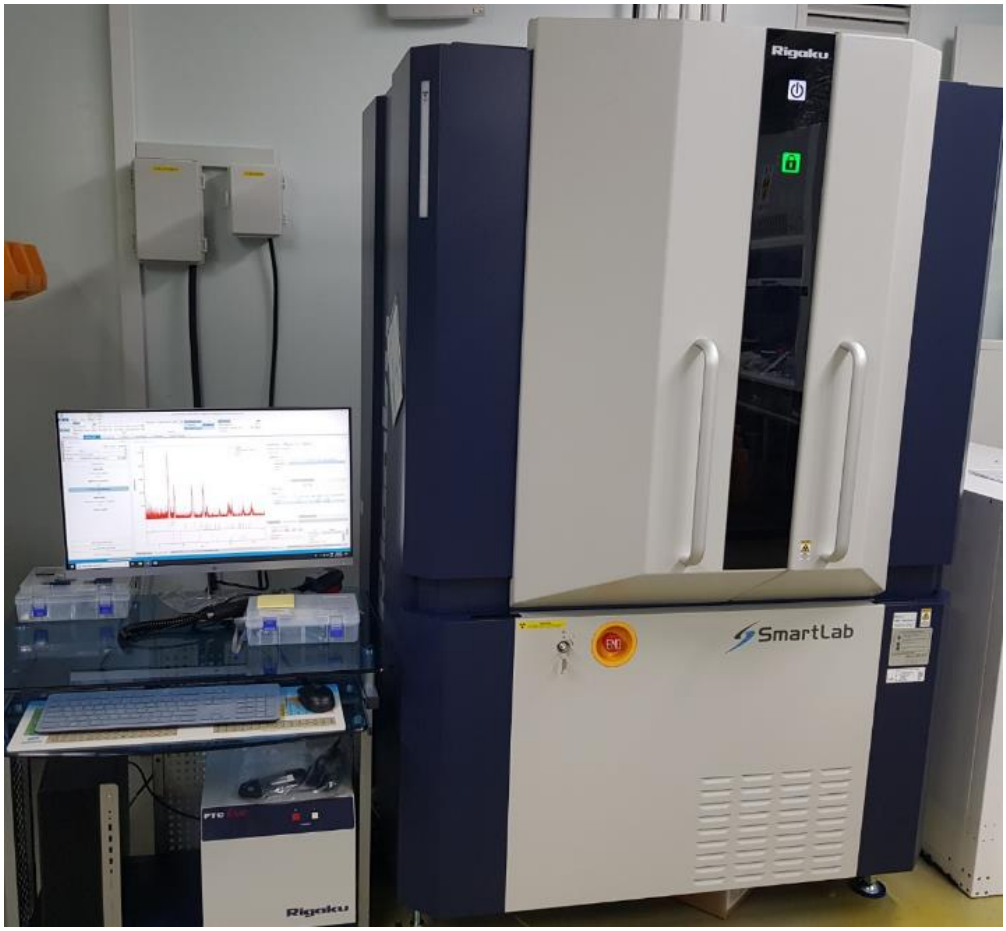

Figure 3-7. Apparatus of the XRD (SmartLab, Rigaku)

3.2.2. Thermophysical property measurements

3.2.2.1. Densitometer

The density of the SPSed pellets was measured at room temperature by using a densitometer (shown in Figure 3-8). The samples were first weighed in dry air and in ethanol, respectively. The samples were then reweighted in the air assuming that the open pores are filled with liquid. From the measured weights, the bulk density of samples was calculated referring to the ASTM B962 [112]. Notably, not water but ethanol was used not to produce radioactively contaminated water in the lab environment. The temperature-dependent density was calculated as follows:

$$\rho(T) = \frac{\rho_0}{(1+\alpha)^3} \tag{3-1}$$

where ρ is the temperature-dependent density, ρ_0 is the density at room temperature, and α is the linear thermal expansion coefficient (CLTE) of the sample.

The theoretical density of Gd compounds mixed UN pellets was calculated based on the rule of mixtures as follows:

$$\frac{1}{\rho_m} = \frac{w_1}{\rho_1} + \frac{w_2}{\rho_2} \tag{3-2}$$

where ρ_m is the density of the mixture, ρ_1, and ρ_2 are the density of pure components 1 and 2, and w_1 and w_2 are the weight fraction of pure components 1 and 2 in the mixture. The relative density of composite pellets was calculated using the corresponding TD obtained using Equation 3-2.

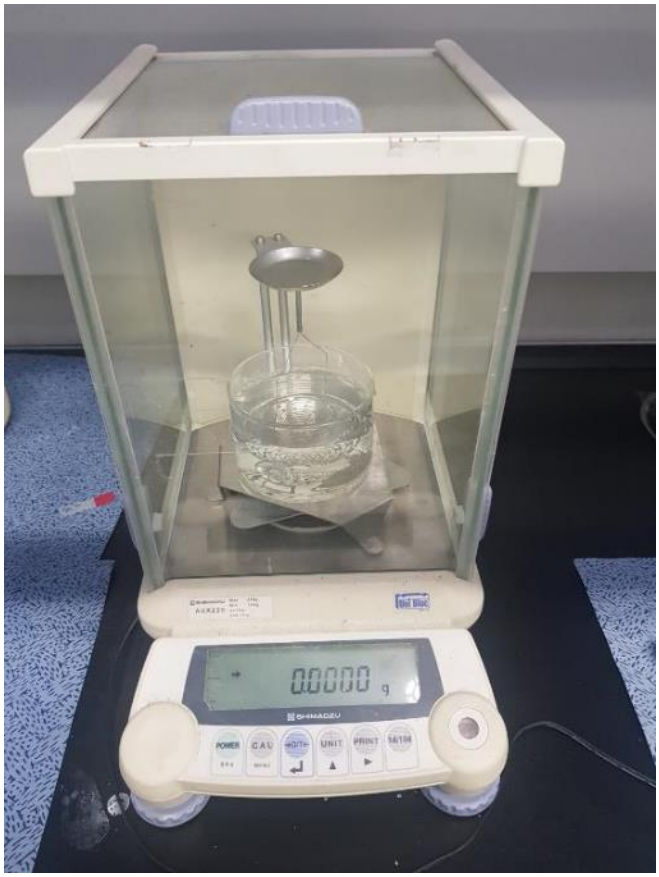

Figure 3-8. Apparatus of the densitometer

3.2.2.2. Dilatometry

The thermal expansion coefficients of pure GdN and Gd_2O_3 pellets were measured using a dilatometer (DIL 402C, Netzsch). For this purpose, GdN and Gd_2O_3 pellet rods (6.0 mmD × 10 mmH) were additionally prepared using the SPS. The specimen length changes (dL/L_0) were recorded with increasing temperature from 25 to 1000 °C. The whole process was conducted under an Ar atmosphere to avoid sample oxidation. The CLTE values of the samples were calculated using the reference data of the standard Al_2O_3 rod with the same dimension, which was measured in advance at the same conditions.

For pure UN and composite pellets, no commercially available laboratory was found which would accept those samples due to the radioactive nature of the uranium containing samples. Thus, the CLTE values of UN/GdN and UN/Gd_2O_3 samples were calculated according to the rule of mixtures at the corresponding mixing ratios.

3.2.2.3. Laser flash analysis

The thermal diffusivity and specific heat capacity (C_p) were measured using LFA (LFA467HT, Netzsch) shown in Figure 3-9. The measurement was conducted in the temperature range of 25–1000 °C following the standard procedure (ASTM E1461) [113]. At first, a high-intensity and short-duration laser pulse heated the bottom-side of the sample surface. The infrared (IR) detector then recorded the temperature change of the opposite-side surface as a function of the time. Both sides of the sample surfaces were coated with a thin layer of graphite to ensure the complete absorption of the laser. During the measurement, argon atmosphere was used to avoid sample oxidation and liquid nitrogen (LN_2) was continuously supplied to prevent IR sensor overheating. The thermal diffusivity was obtained as follows:

$$\alpha = 0.1388 \cdot L / t_{half} \tag{3-3}$$

where α is the thermal diffusivity, L the thickness of the sample, and t_{half} the time when the temperature of the opposite-side surface reaches half of its maximum value. The dimensions of the LFA samples were measured to be 9.80–10.00 mm diameter and 2.50–3.00 mm thickness. The heat capacity of the samples was simultaneously obtained from the measured sample temperature as follows:

$$C_p^{sample} = \frac{T_{\max}^{ref}}{T_{\max}^{sample}} \cdot \frac{\rho^{ref} \cdot L^{ref}}{\rho^{sample} \cdot L^{sample}} \cdot C_p^{ref} \quad (3\text{-}4)$$

where T_{max} is the maximum temperature, ρ is the density, L is the height, and the superscripts *ref* and *sample* refer to the reference and the sample, respectively. The pyroceram-9606 was used as the reference. The measurement uncertainty is estimated to be 5% for this method [114,115].

The heat capacity of the composite pellets was calculated by the Kopp–Neumann law, i.e., it was presumably assumed that the heat capacity of the mixture is dependent on the composition of the elements rather than the microstructure.

3.2.2.4. Thermal conductivity calculation

The thermal conductivity of the samples was calculated as follows:

$$\lambda = \alpha \times \rho \times C_p \quad (3\text{-}5)$$

where λ is the thermal conductivity (W/m·K), α the thermal diffusivity (m^2/s), ρ the density (kg/m^3), and C_p the specific heat capacity (J/kg·K). In this study, since most of the sample densities were close to 97 %TD, the data was not corrected to the single density using the Maxwell-Eucken correlation.

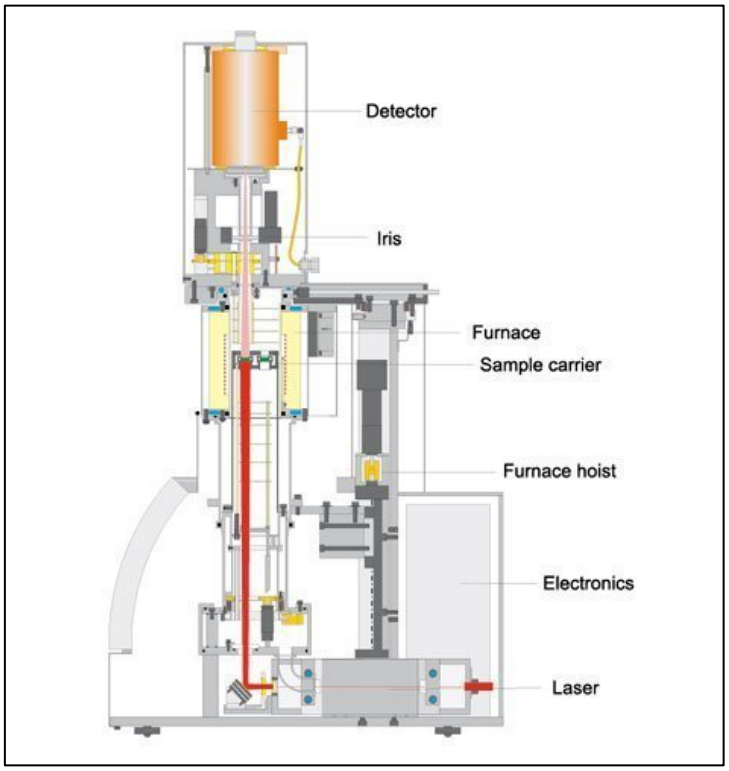

Figure 3-9. Apparatus of LFA-467HT (top) with schematic configuration (bottom, figure courtesy of NETZSCH)

Chapter 4. RESULTS

4.1. Pure UN pellets

4.1.1. XRD patterns

Figure 4-1 shows the XRD patterns of the UN powder (blue line) synthesized from the hydride-nitride process and the pellet (yellow line) sintered by SPS. In the case of the powder sample, the relative intensities and positions of all peaks were well matched with the International Centre for Diffraction Data (ICDD) reference patterns (PDF#00-032-1397). On the contrary, the XRD pattern of the pellet is partially unmatched with the reference of which the intensity of the (200) peak is higher than that of the reference. The lattice parameters of the powder and pellet were estimated to be 4.888 and 4.876 Å, respectively. The values are slightly lower than that of the ICDD reference (4.8897 Å). Further discussion on the results is presented in Section 5.1.1.

4.1.2. Density

The pellet densities obtained under various SPS conditions are organized in Figure 4-2 and Table 4-1. The pellet density increased significantly with increasing temperature for two different dwell times of 10 and 60 min, while relative densities were closing the gap with increasing sintering temperature. Eventually, almost the same densities (~97 %TD) were achieved for the pellets sintered at temperature 1800 °C; thus, higher sintering temperature over 1800 °C was not examined further. To better understand the effect of the dwell time on the pellet density, several pellets were additionally sintered for 5, 30, and 180 min at 1800 °C. The measured densities (see Table 4-1) at 1800 °C reveal that the maximum density of pellets was only slightly higher than ~97 %TD even for 180 min, though the pellet density rapidly reached 97.0 %TD within 5 min. This clearly indicates no appreciable densification occurred after the first 5 min at 1800 °C.

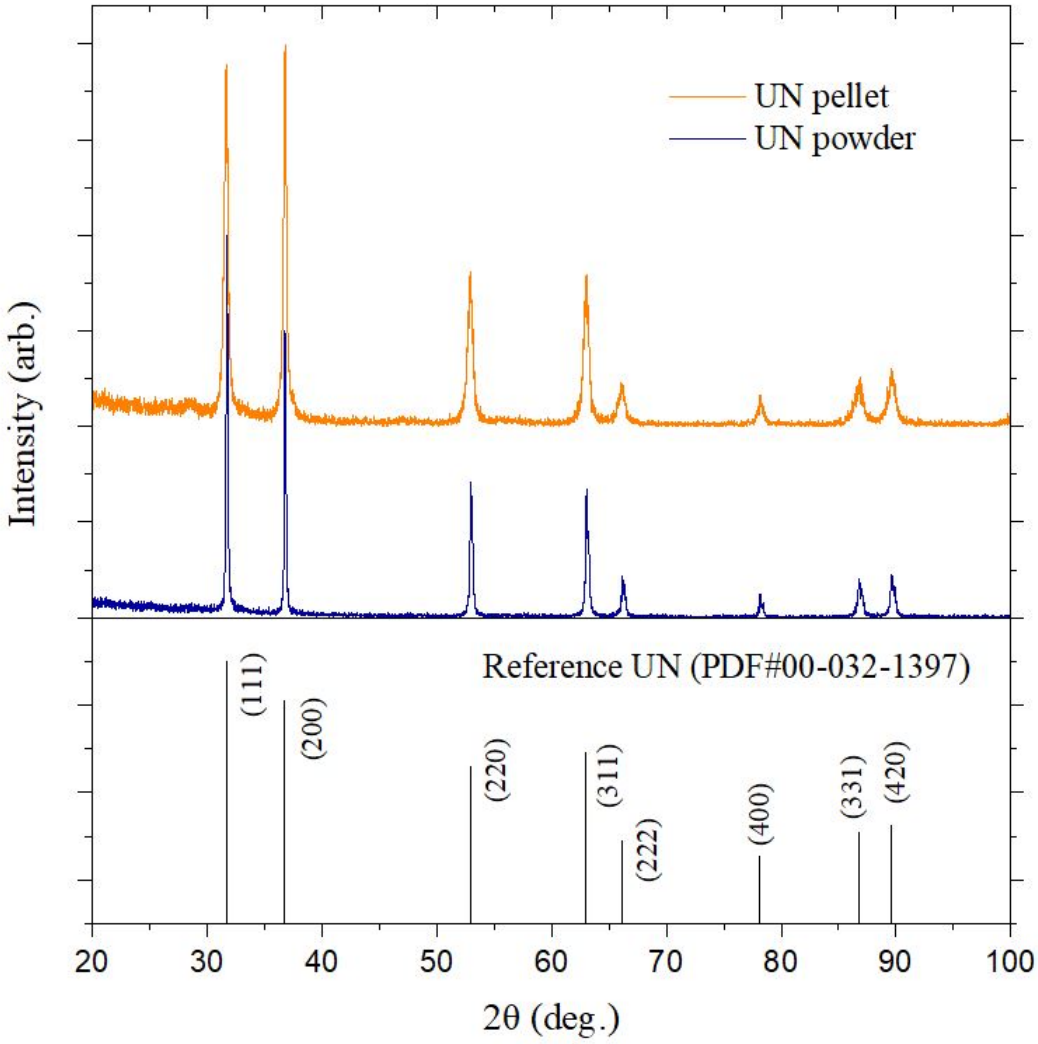

Figure 4-1. Normalized XRD patterns of UN powder (blue) and pellet (yellow) with ICDD reference of PDF#00-032-1397 (black)

Table 4-1. Density of the SPSed UN pellets at the corresponding conditions

	Dwell time (min)				
	5	10	30	60	180
Temperature (°C)	Density (%)				
1500		85.9		93.6	
1600		92.4		95.9	
1700		95.3		96.7	
1800	97.0	97.0	97.2	97.3	97.1

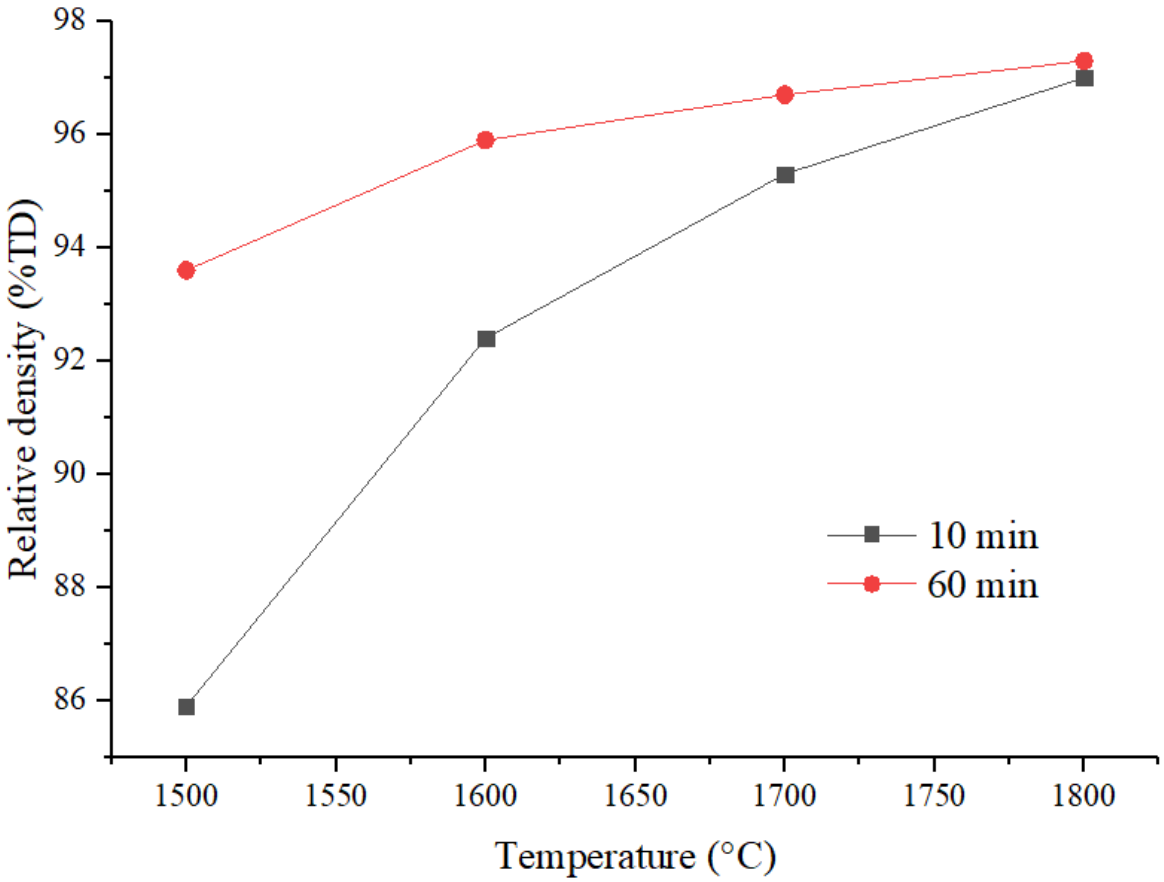

Figure 4-2. Density of the UN pellets SPSed for 10 min (grey) and 60 min (red) as a function of sintering temperature.

4.1.3. Microstructure

4.1.3.1. Microstructures of as-polished UN pellets

The microstructural evolution of UN pellets during SPS is displayed in this section. Figure 4-3 shows the as-polished surface of the UN pellet sintered at 1500 °C for 10 min. The porous structures were widely observed on the sample surface due to its low density (~86 %TD). Figure 4-4 presents the pellet sintered for 60 min at the same temperature. Since the relatively high density (~94 %TD) was obtained in this sample, a porous structure was not further observed, while several large isolated pores were presented. In addition, sub-micron pores, shown as small black dots, appeared throughout the sample surface. These pore sizes were too small to be measured using the SEM (COXEM, EM-30ax plus), which provides relatively low effective magnification (up to ~10,000x).

The as-polished surface of pellets sintered at 1600 and 1700 °C are displayed in Figures 4-5 to 4-8. For all samples with a similarly high density (from 92.4 to 96.7 %TD), small pores (black dots) appeared throughout the surfaces. It is notable that sub-micron pores appeared to be lined up on the pellet sintered at 1600 °C for 10 min (see Figure 4-5b) and the pellet sintered at 1700 °C for 60 min (see Figure 4-8a), indicating that the continuous pore channels were formed along the grain boundaries during the rapid densification.

A noticeable microstructural evolution occurred in the pellets sintered at 1800 °C. The comparison between Figure 4-9 and 4-10 reveals that the pore size increased as the sintering time increased from 60 to 180 min. Remarkably large pores were only observed in the pellet sintered at 1800 C for 180 min (Figure 4-10b). This may indicate that pore agglomeration has occurred as a result of grain growth above 1800 °C.

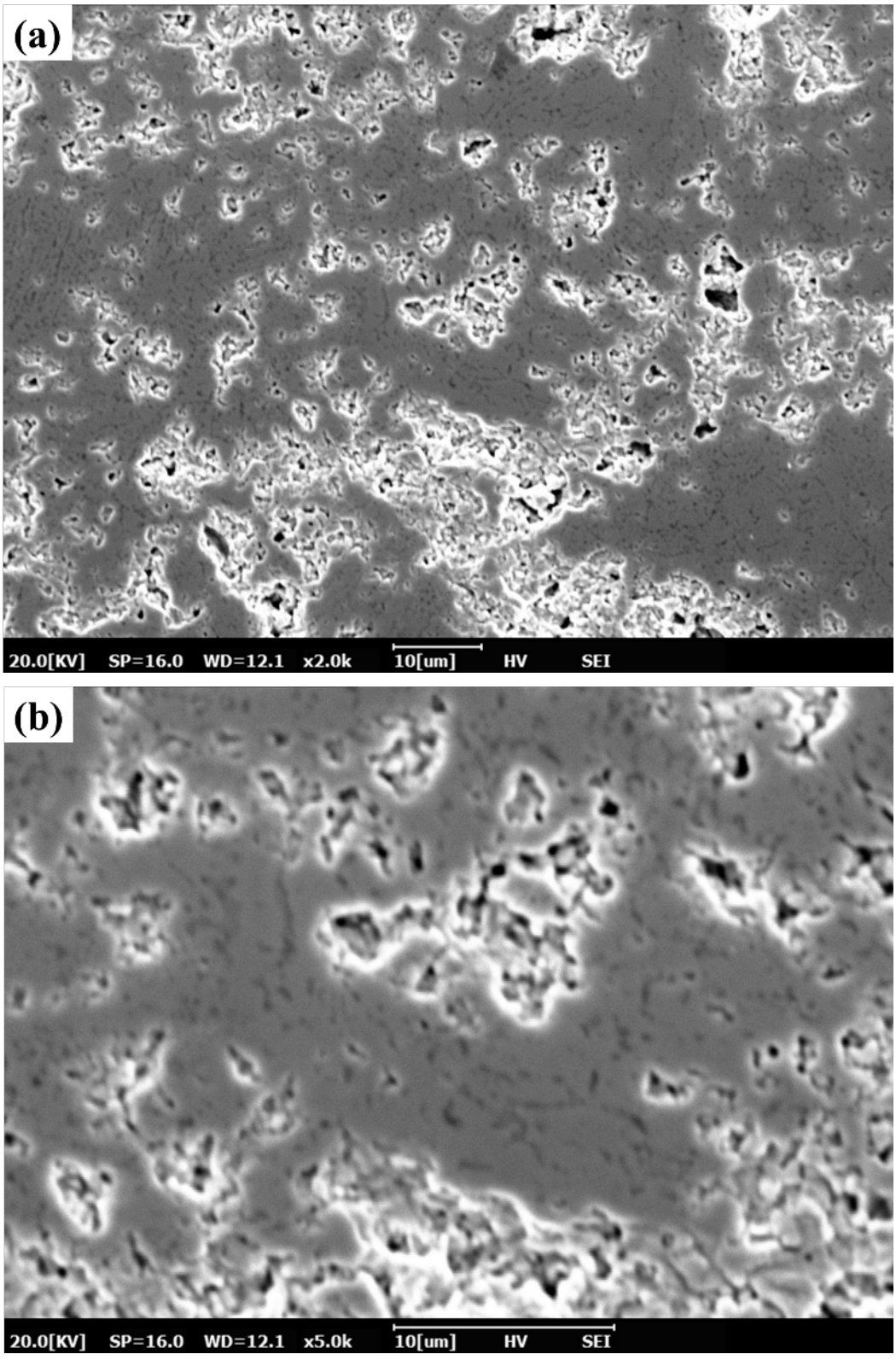

Figure 4-3. SEM images of as-polished UN pellet surface SPSed at 1500 °C for 10 min under 70 MPa uniaxial pressure (a) x2,000 and (b) x5,000

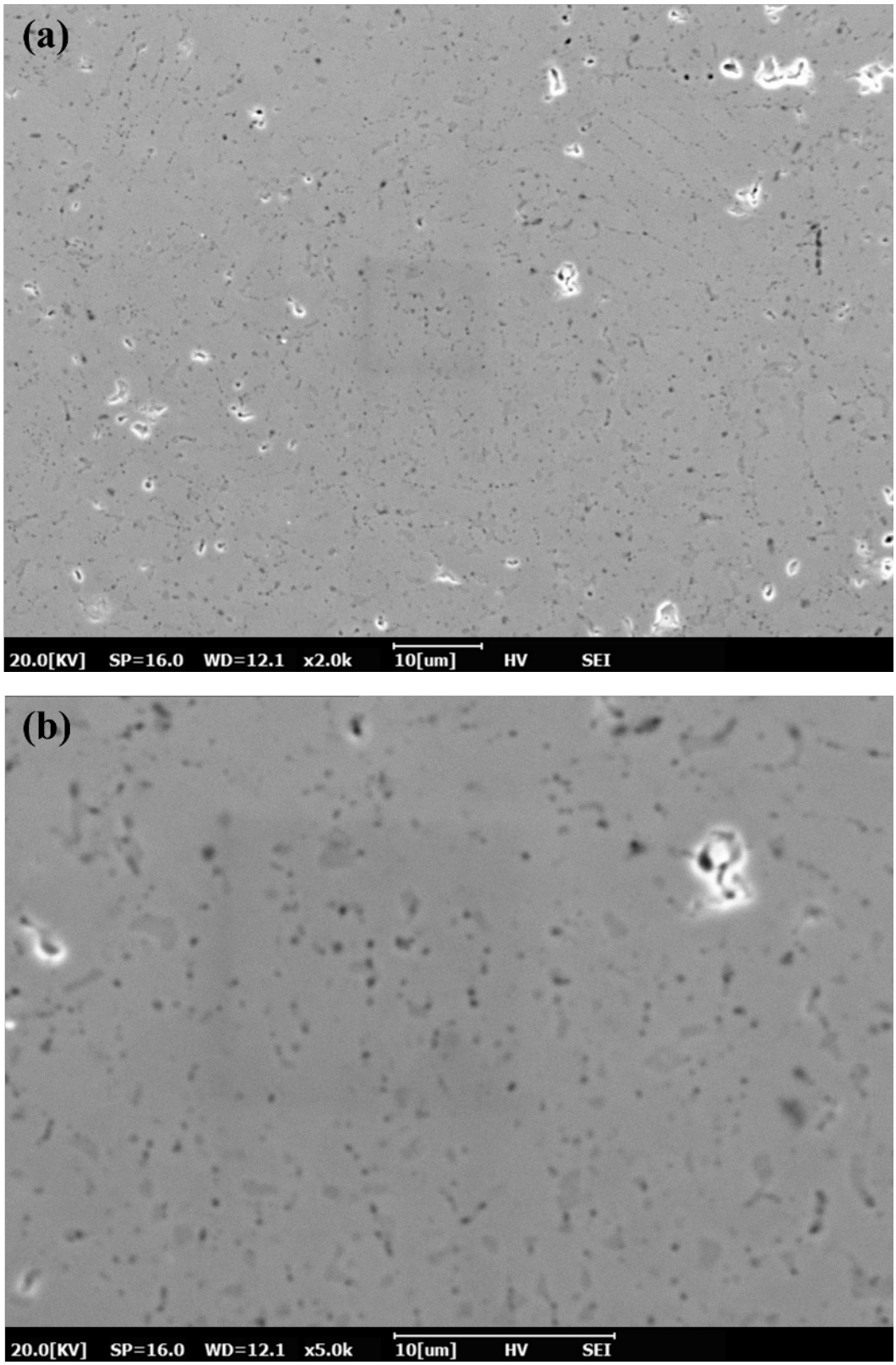

Figure 4-4. SEM images of as-polished UN pellet surface SPSed at 1500 °C for 60 min under 70 MPa uniaxial pressure (a) x2,000 and (b) x5,000

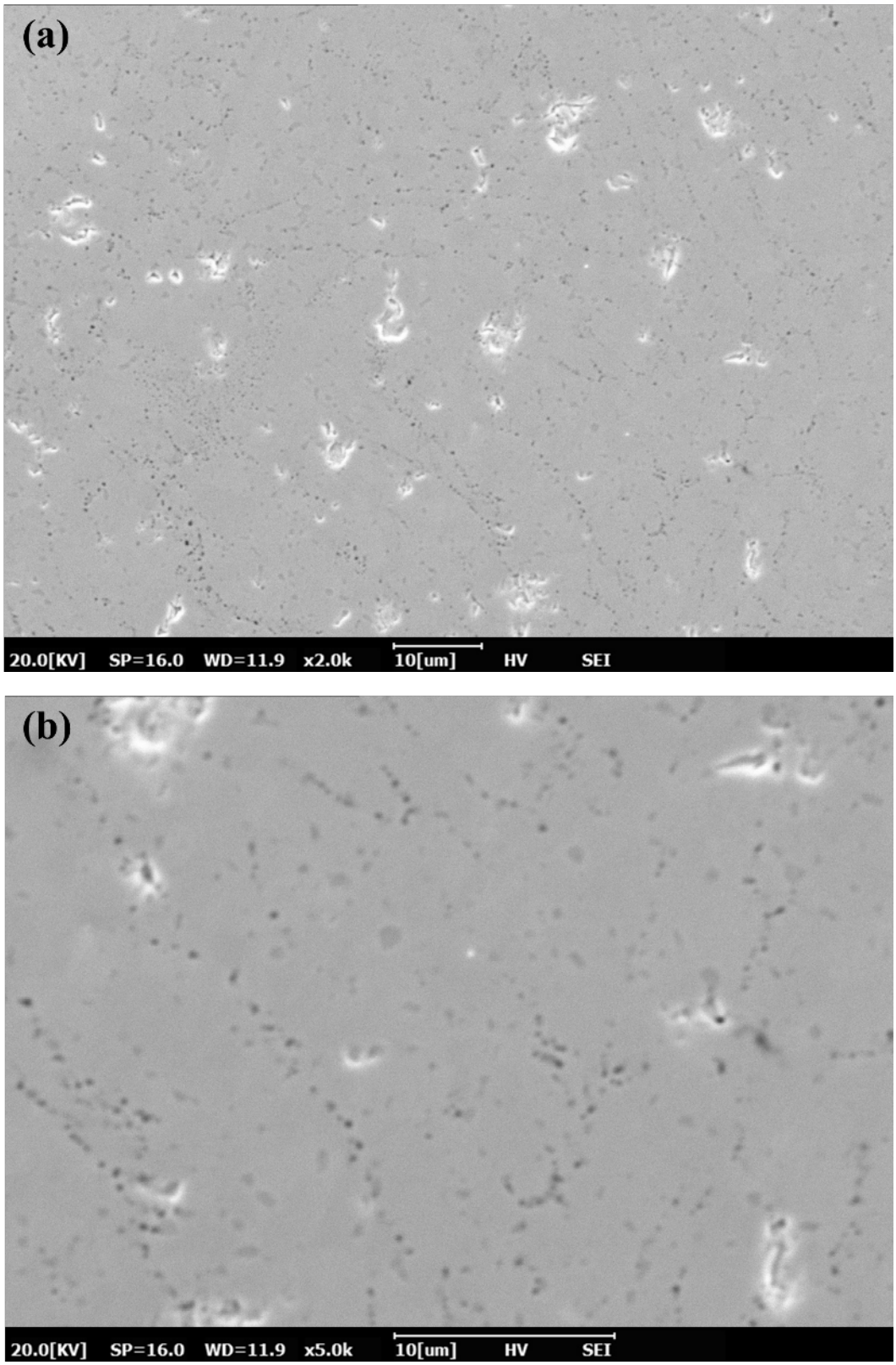

Figure 4-5. SEM images of as-polished UN pellet surface SPSed at 1600 °C for 10 min under 70 MPa uniaxial pressure (a) x2,000 and (b) x5,000

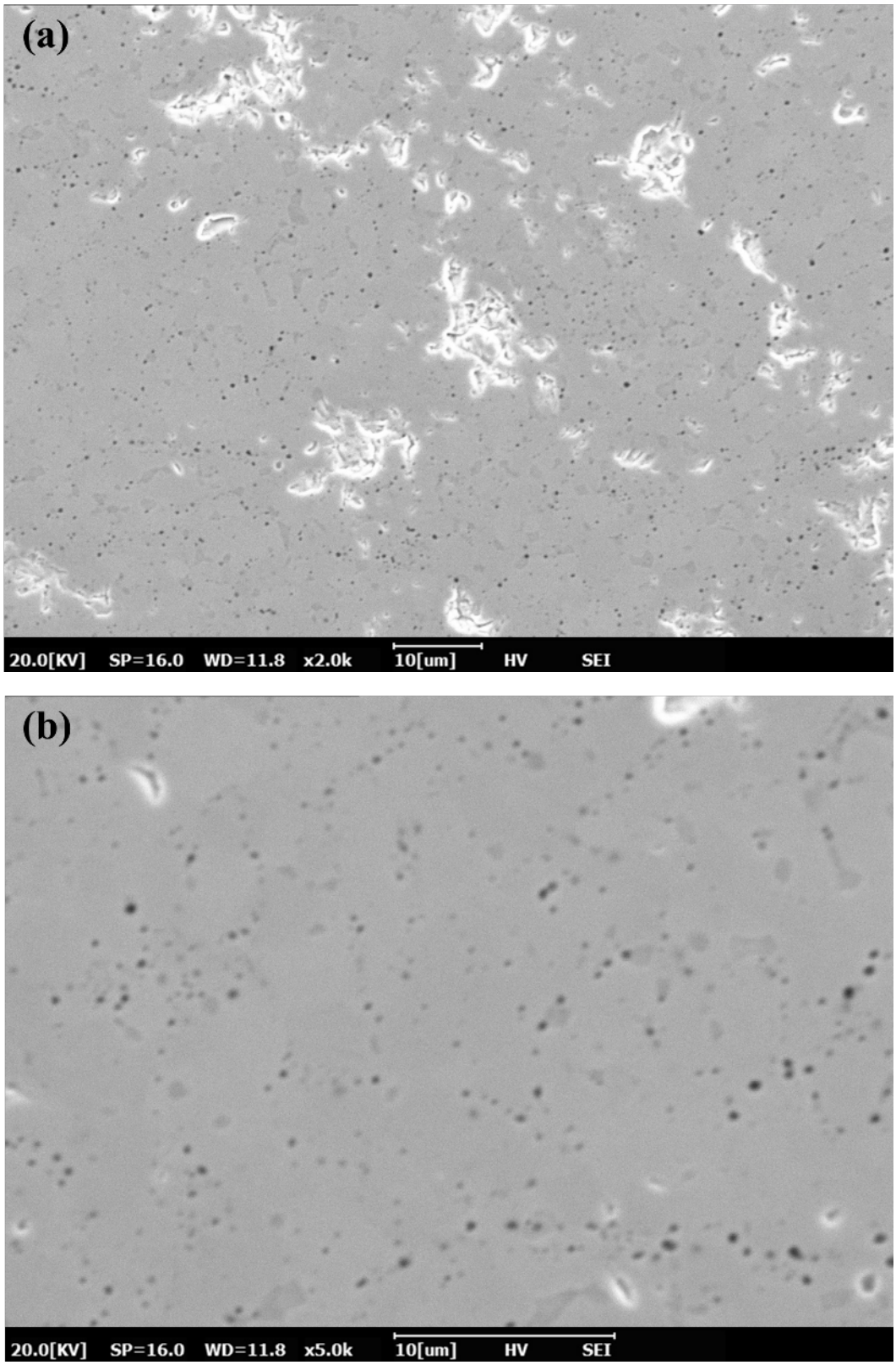

Figure 4-6. SEM images of as-polished UN pellet surface SPSed at 1600 °C for 60 min under 70 MPa uniaxial pressure (a) x2,000 and (b) x5,000

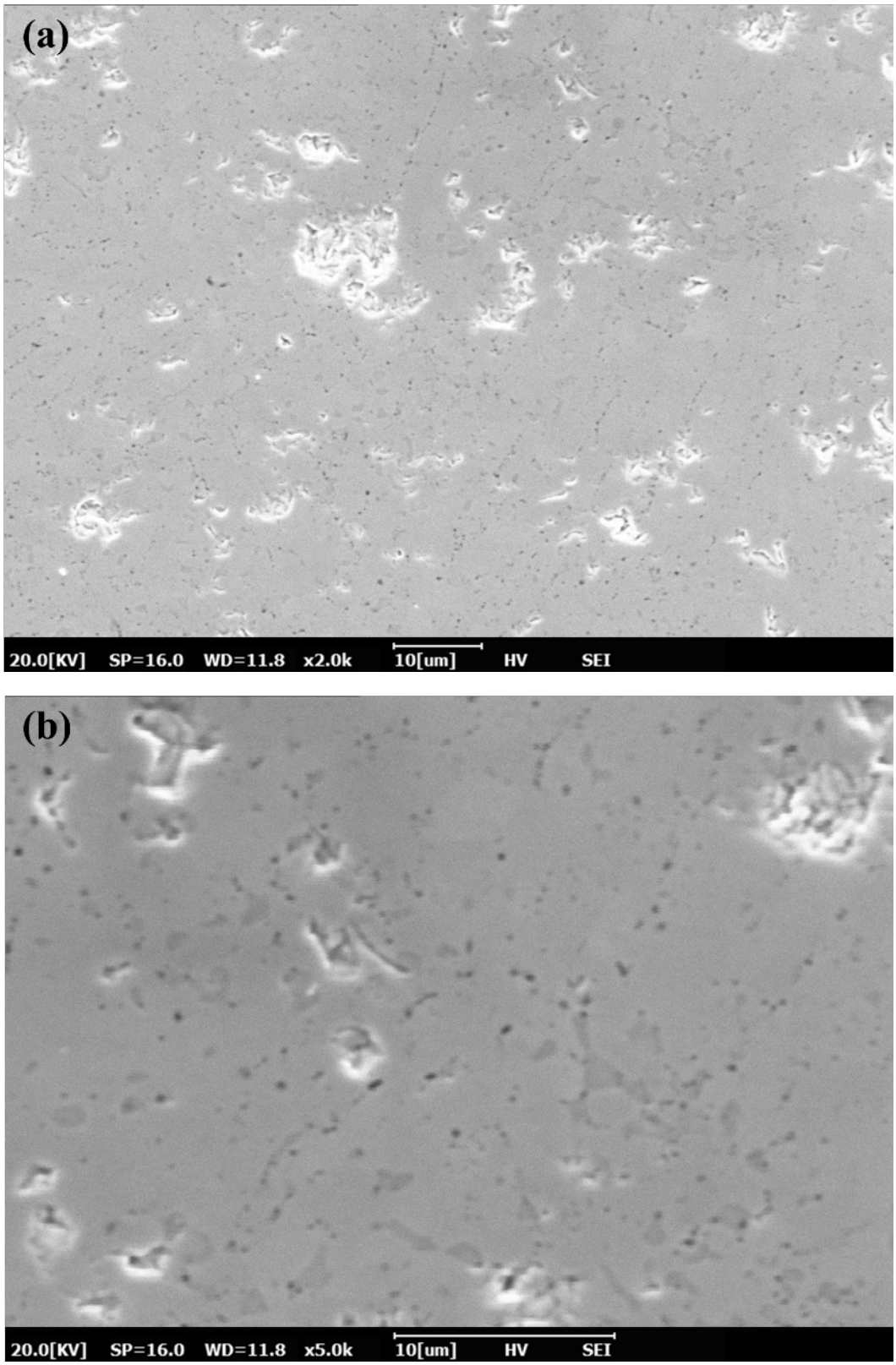

Figure 4-7. SEM images of as-polished UN pellet surface SPSed at 1700 °C for 10 min under 70 MPa uniaxial pressure (a) x2,000 and (b) x5,000

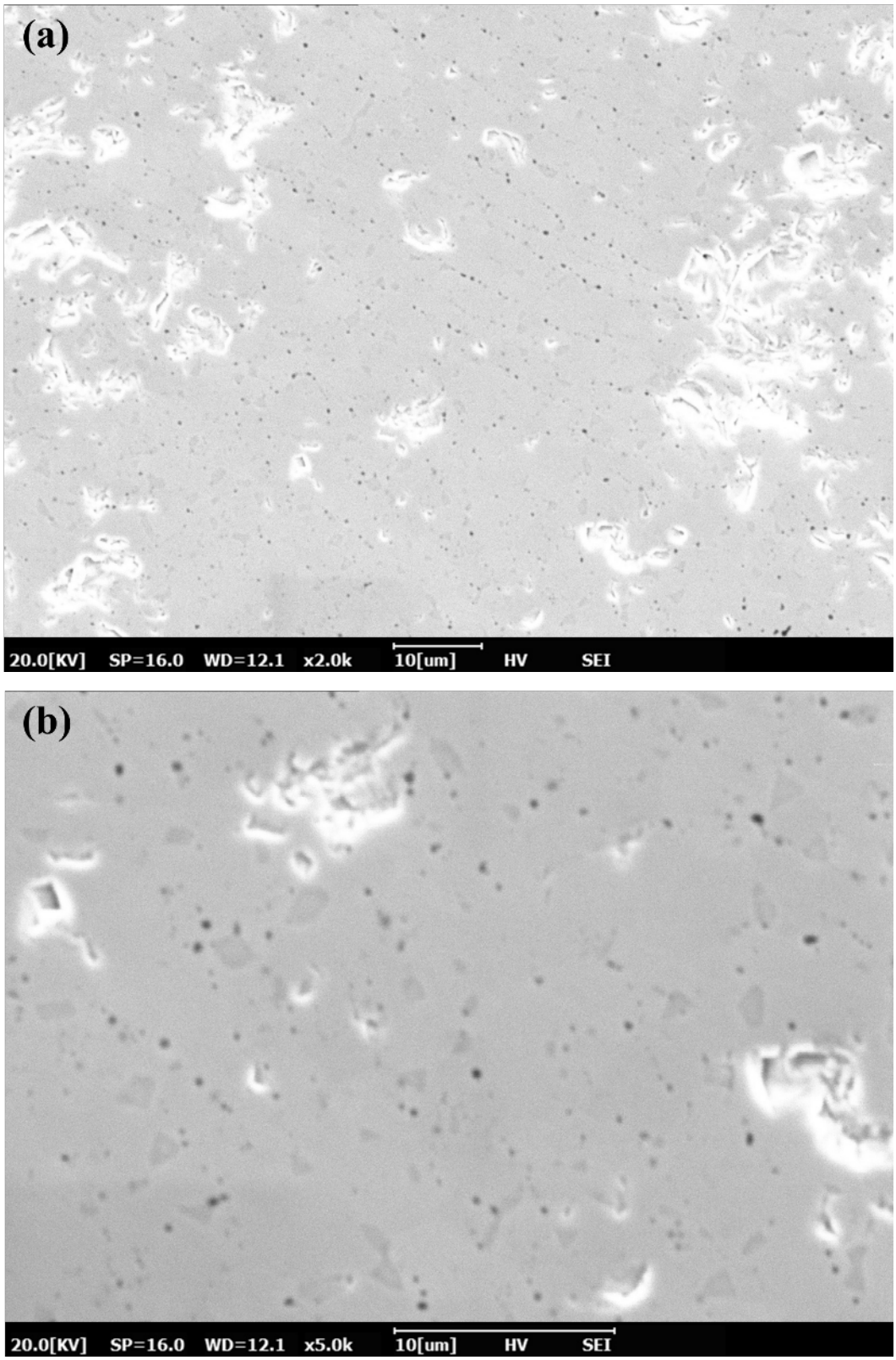

Figure 4-8. SEM images of as-polished UN pellet surface SPSed at 1700 °C for 60 min under 70 MPa uniaxial pressure (a) x2,000 and (b) x5,000

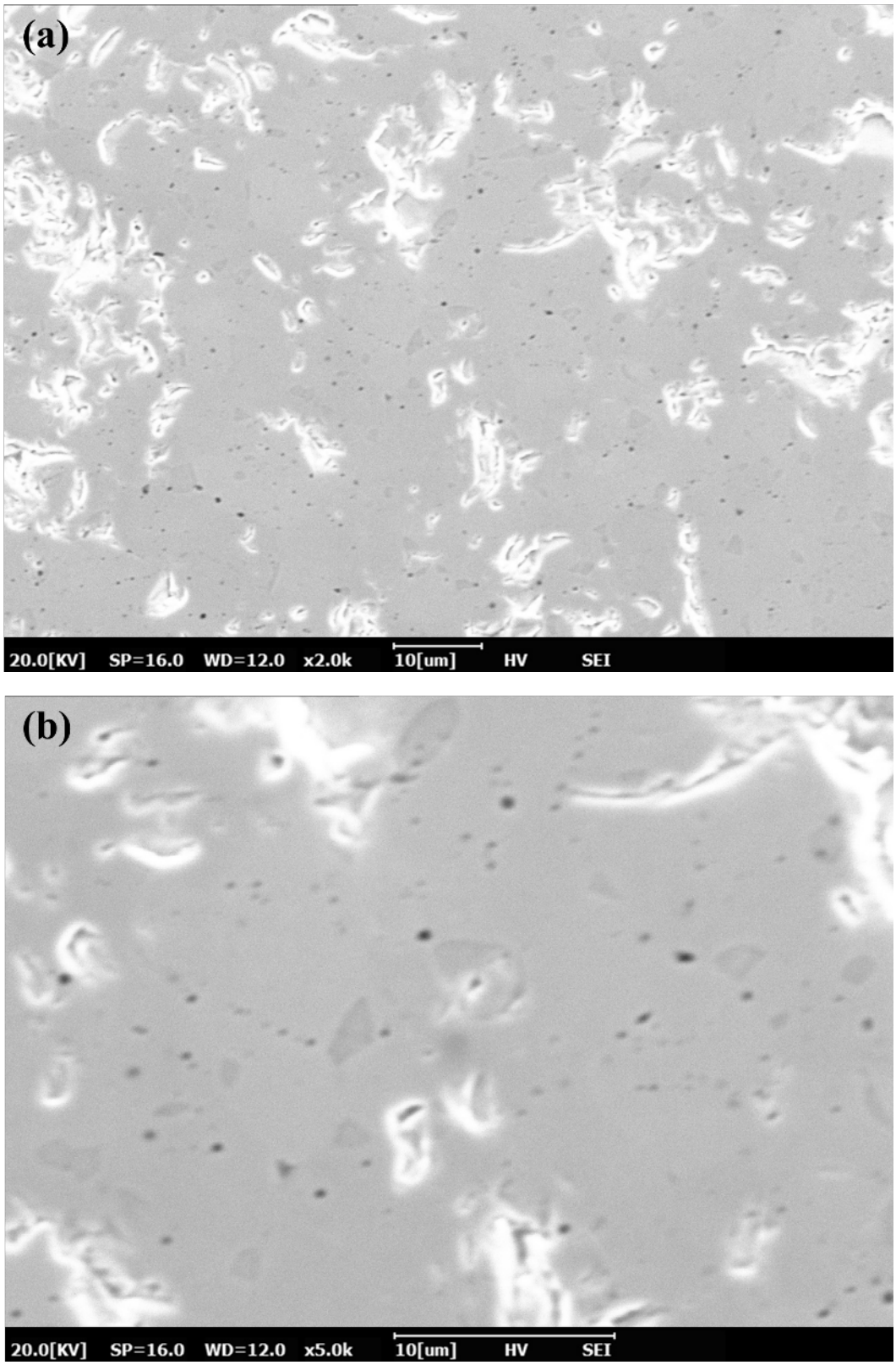

Figure 4-9. SEM images of as-polished UN pellet surface SPSed at 1800 °C for 60 min under 70 MPa uniaxial pressure (a) x2,000 and (b) x5,000

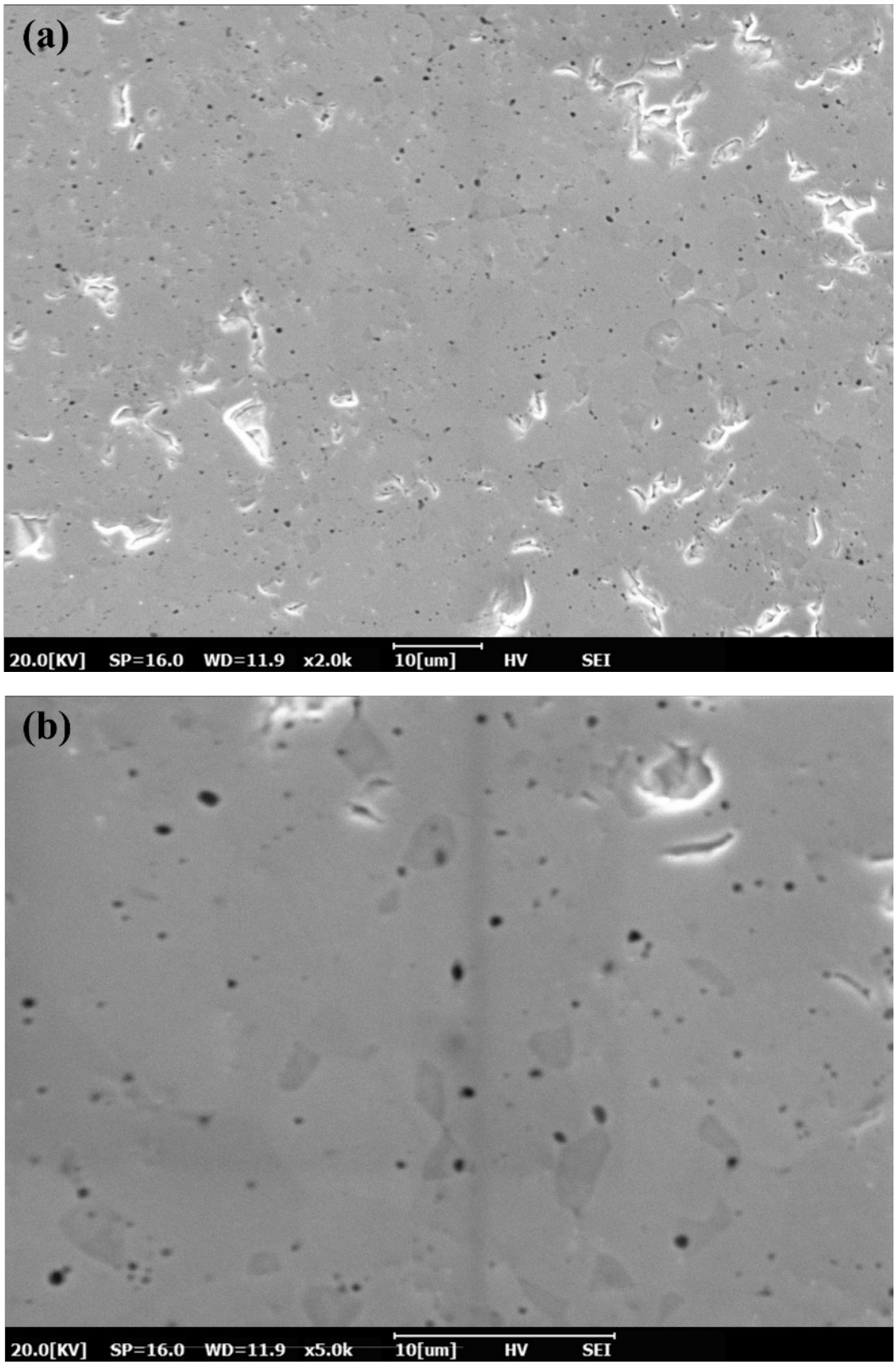

Figure 4-10. SEM images of as-polished UN pellet surface SPSed at 1800 °C for 180 min under 70 MPa uniaxial pressure (a) x2,000 and (b) x5,000

4.1.3.2. Microstructures of thermally etched UN pellets

The SEM images of the thermally etched pellet surface are displayed in this section. The images with magnifications of 2000–5000x were selected to present the clear microstructure of each sample. In many cases, under- and over-etched areas were co-existed on the samples. Over-etching seemed to have occurred due to remnant defects from the polishing process, such as scratches, dents, or cracks.

Figure 4-11 shows the thermally etched microstructure of the UN pellet sintered at 1500 °C for 60 min. The grain sizes were uniformly distributed, while the grain shape was irregular. Slightly under-etched areas were found over the surface (see red circle in Figure 4-11a).

The SEM images of both pellets sintered at 1600 °C for 10 and 60 min are presented in Figures 4-12 and 4-13, respectively. Over-etched areas were widely found and marked with red circles in Figure 4-12. Most of the pores were located at grain boundaries and triple junctions (i.e., intergranular pore), but some pores were presented inside the grains (i.e., intragranular pore) as well.

Figures 4-14 and 4-15 show the thermally etched surface of the UN pellet sintered at 1700 °C. Several small grains began to appear between large grains (marked by red arrows in Figures 4-14 and 4-15, indicating that grain growth had occurred via Ostwald ripening, i.e., small grains had been dissolved into large grains. Some of over-etched areas even seemed to peel off from the surface as marked with yellow circles in Figure 4-14.

The SEM images of the pellets sintered at 1800 °C from 5 to 180 min are presented in Figures 4-16 to 4-20. Large pores were widely observed at grain boundaries and triple junctions, which was in accordance with the microstructural features of the as-polished pellet surface (Figure 4-10b). Several unknown particles were observed, as indicated with yellow arrows in Figure 4-16. These particles appeared to be debris from over-etched surfaces. Two interconnected intragranular pores (Figure 4-18b) seemed about to be merged and subsequently formed a large intragranular pore. Notably, the trapezoidal void was presented in the pellet sintered for 60 min (indicated by the arrow in Figure 4-19b).

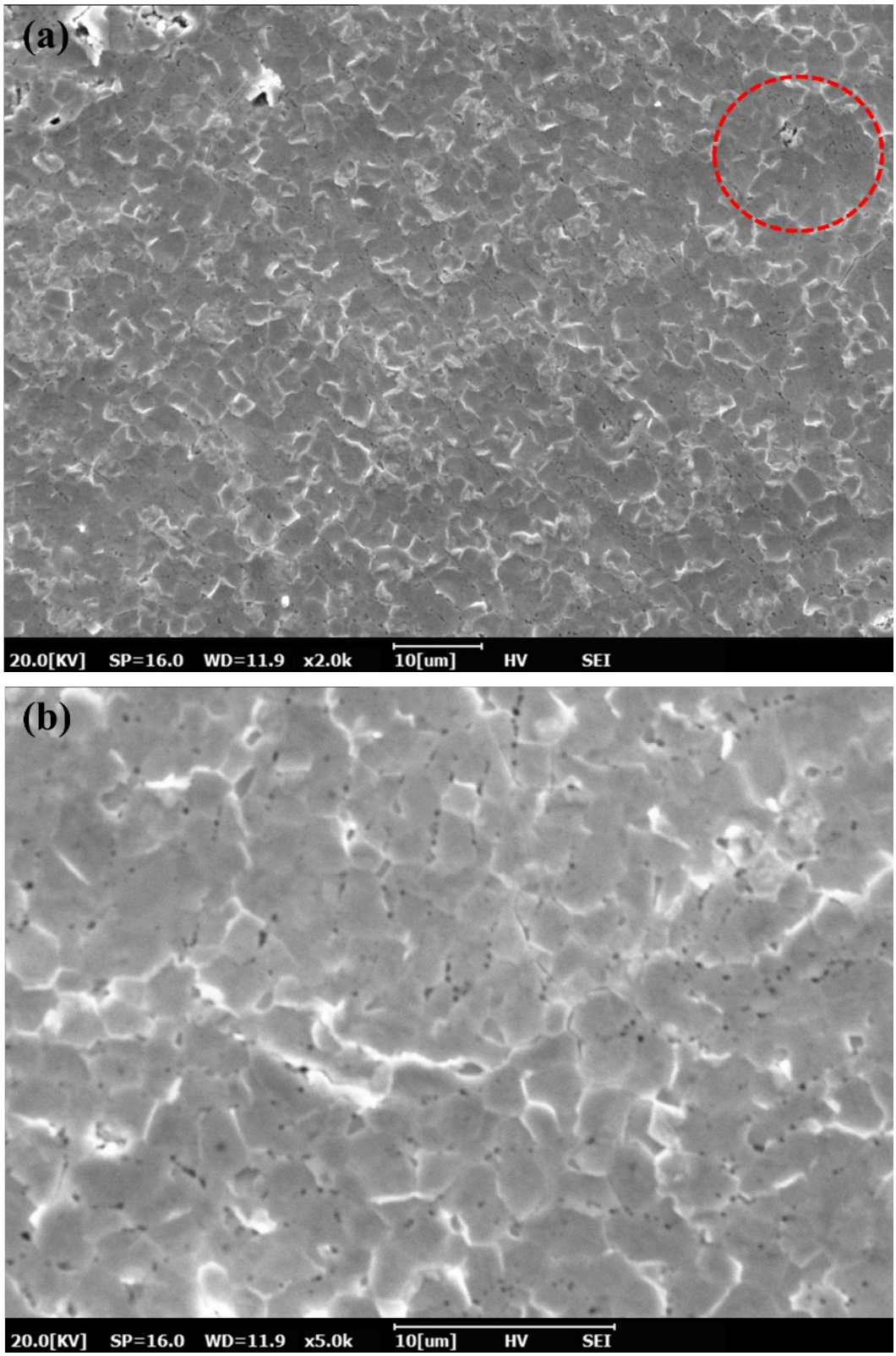

Figure 4-11. SEM images of thermally etched UN pellet surface SPSed at 1500 °C for 60 min under 70 MPa uniaxial pressure (a) x2,000 and (b) x5,000

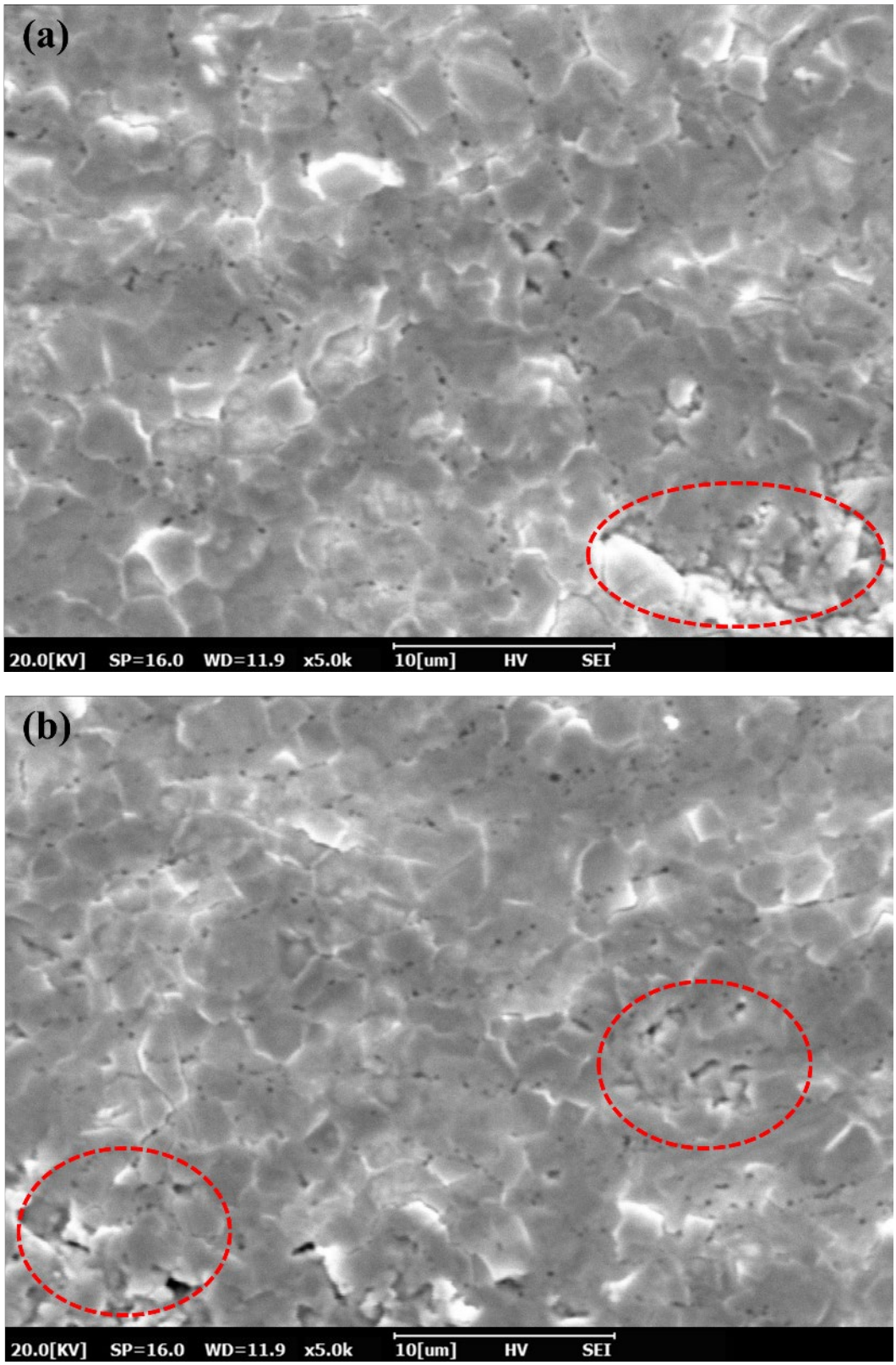

Figure 4-12. SEM images of thermally etched UN pellet surface SPSed at 1600 °C for 10 min under 70 MPa uniaxial pressure (x5,000)

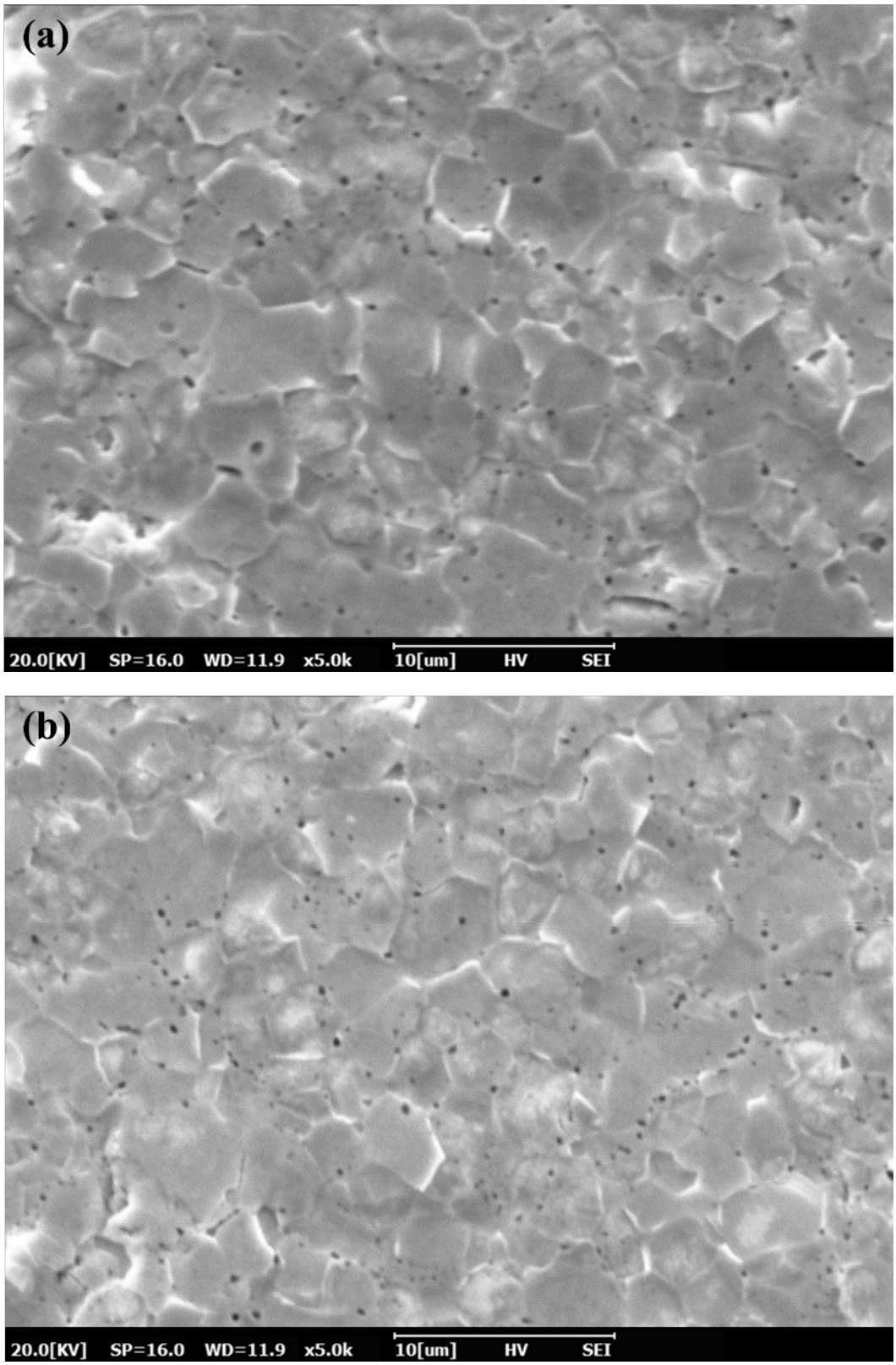

Figure 4-13. SEM images of thermally etched UN pellet surface SPSed at 1600 °C for 60 min under 70 MPa uniaxial pressure (x5,000)

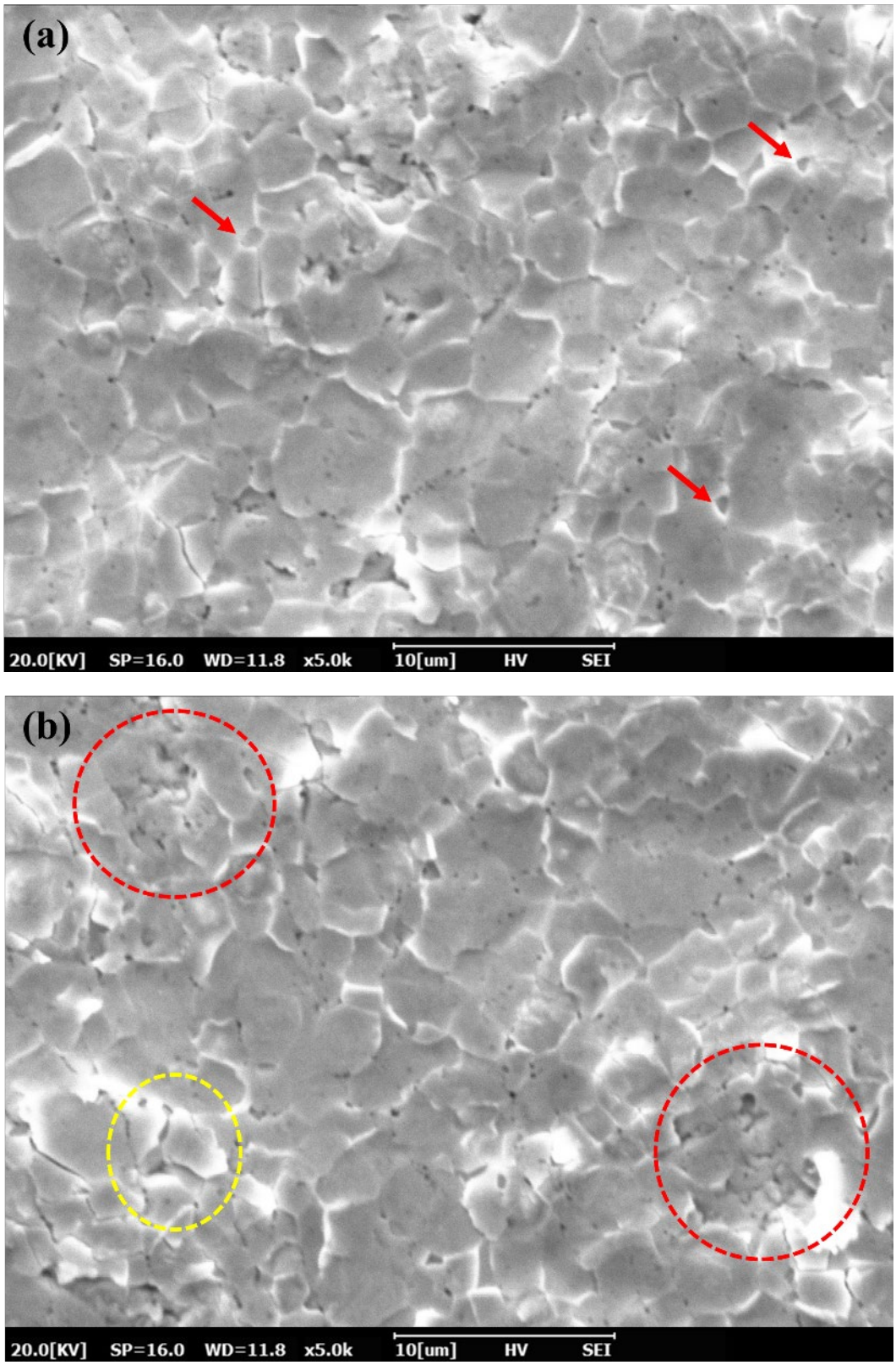

Figure 4-14. SEM images of thermally etched UN pellet surface SPSed at 1700 °C for 10 min under 70 MPa uniaxial pressure (x5,000)

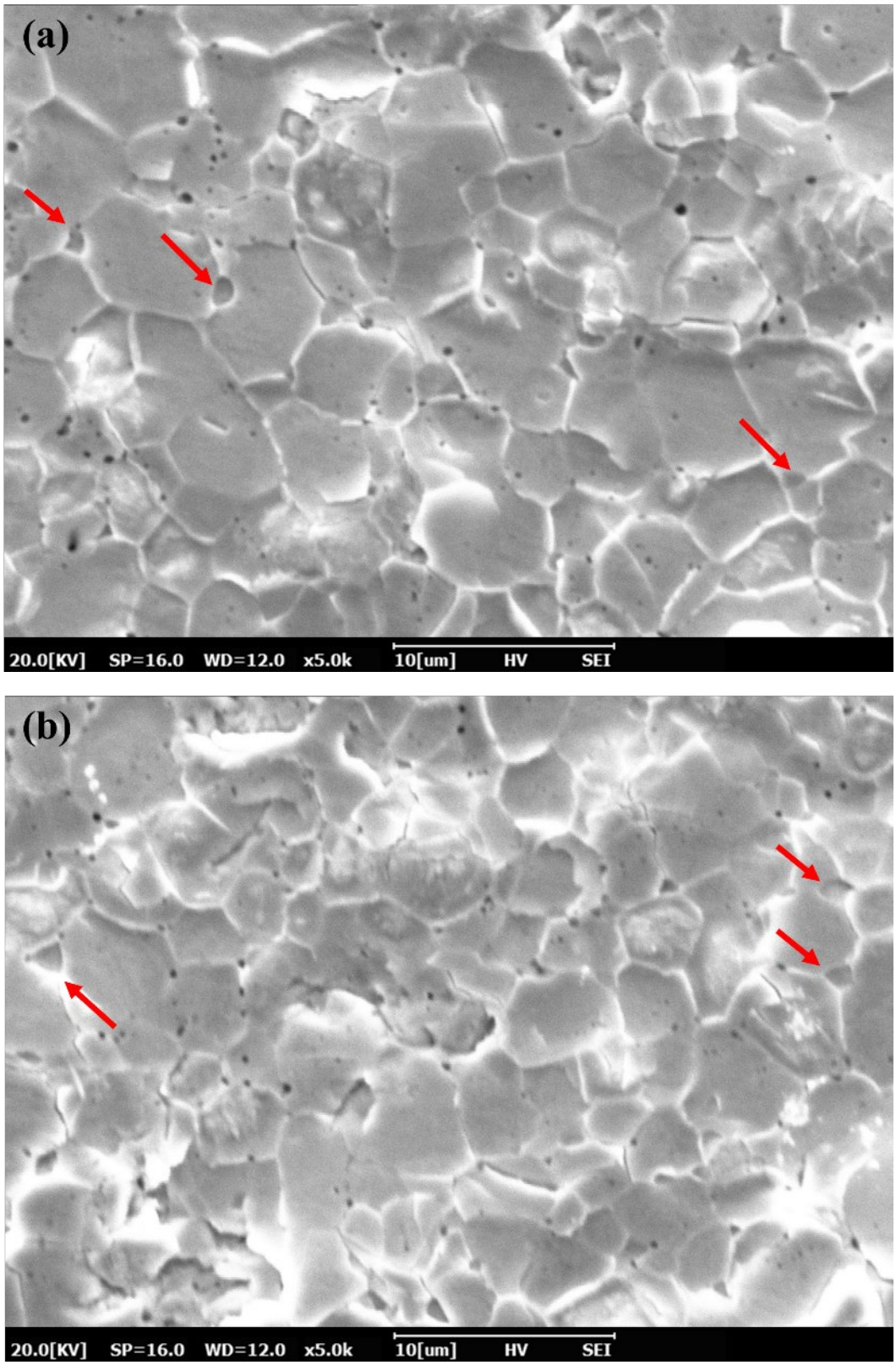

Figure 4-15. SEM images of thermally etched UN pellet surface SPSed at 1700 °C for 60 min under 70 MPa uniaxial pressure (x5,000)

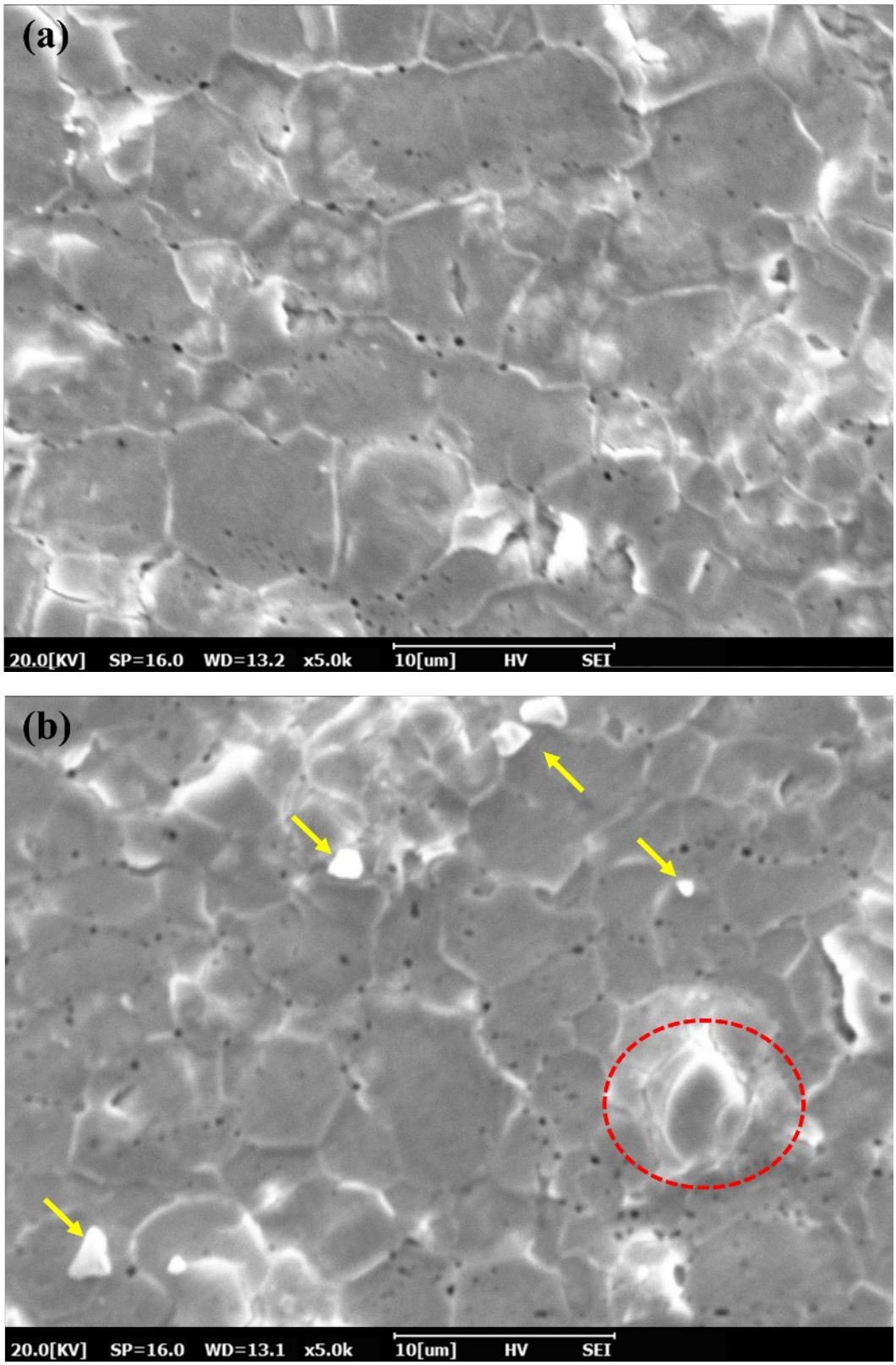

Figure 4-16. SEM images of thermally etched UN pellet surface SPSed at 1800 °C for 5 min under 70 MPa uniaxial pressure (x5,000)

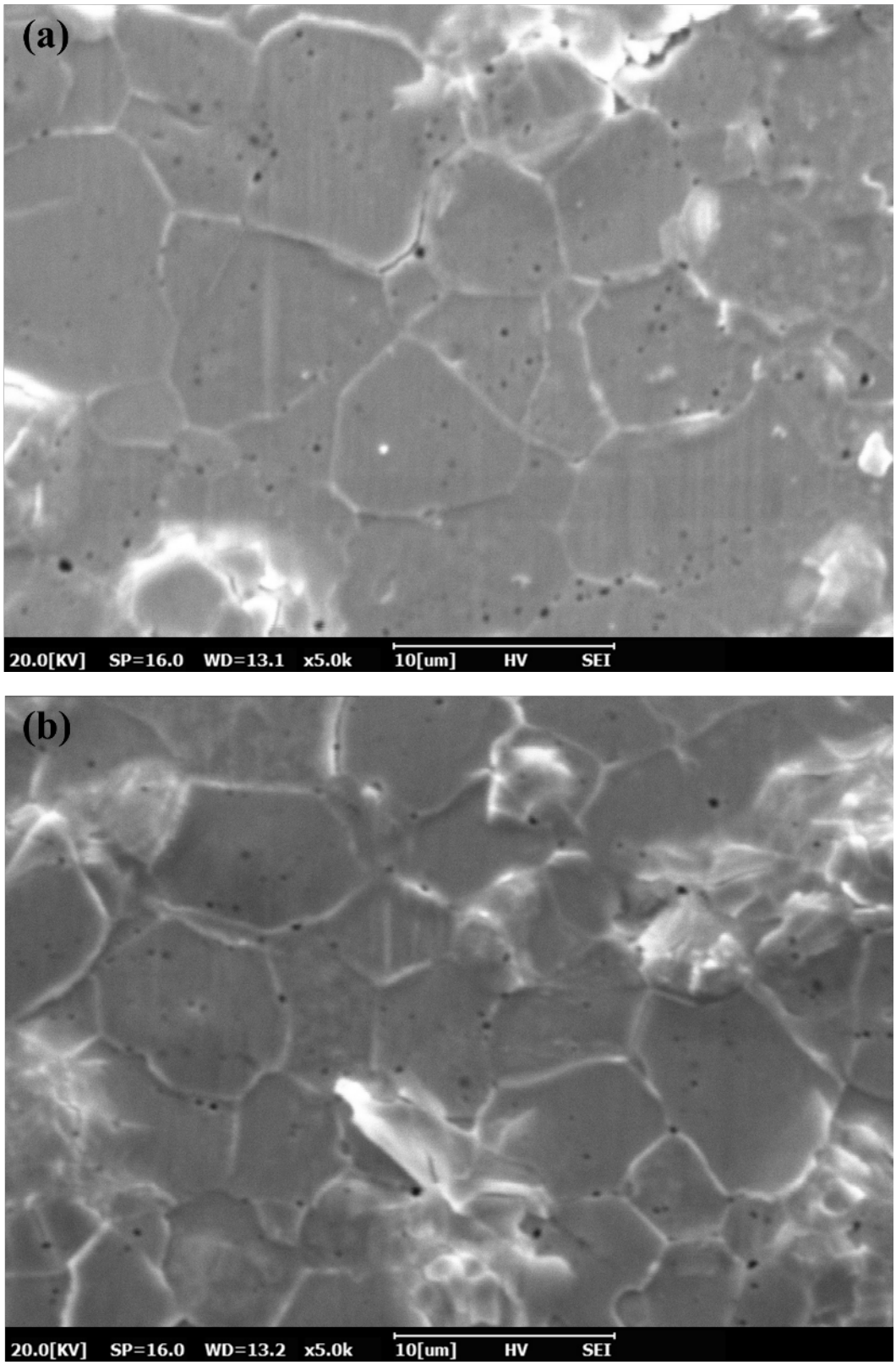

Figure 4-17. SEM images of thermally etched UN pellet surface SPSed at 1800 °C for 10 min under 70 MPa uniaxial pressure (x5,000)

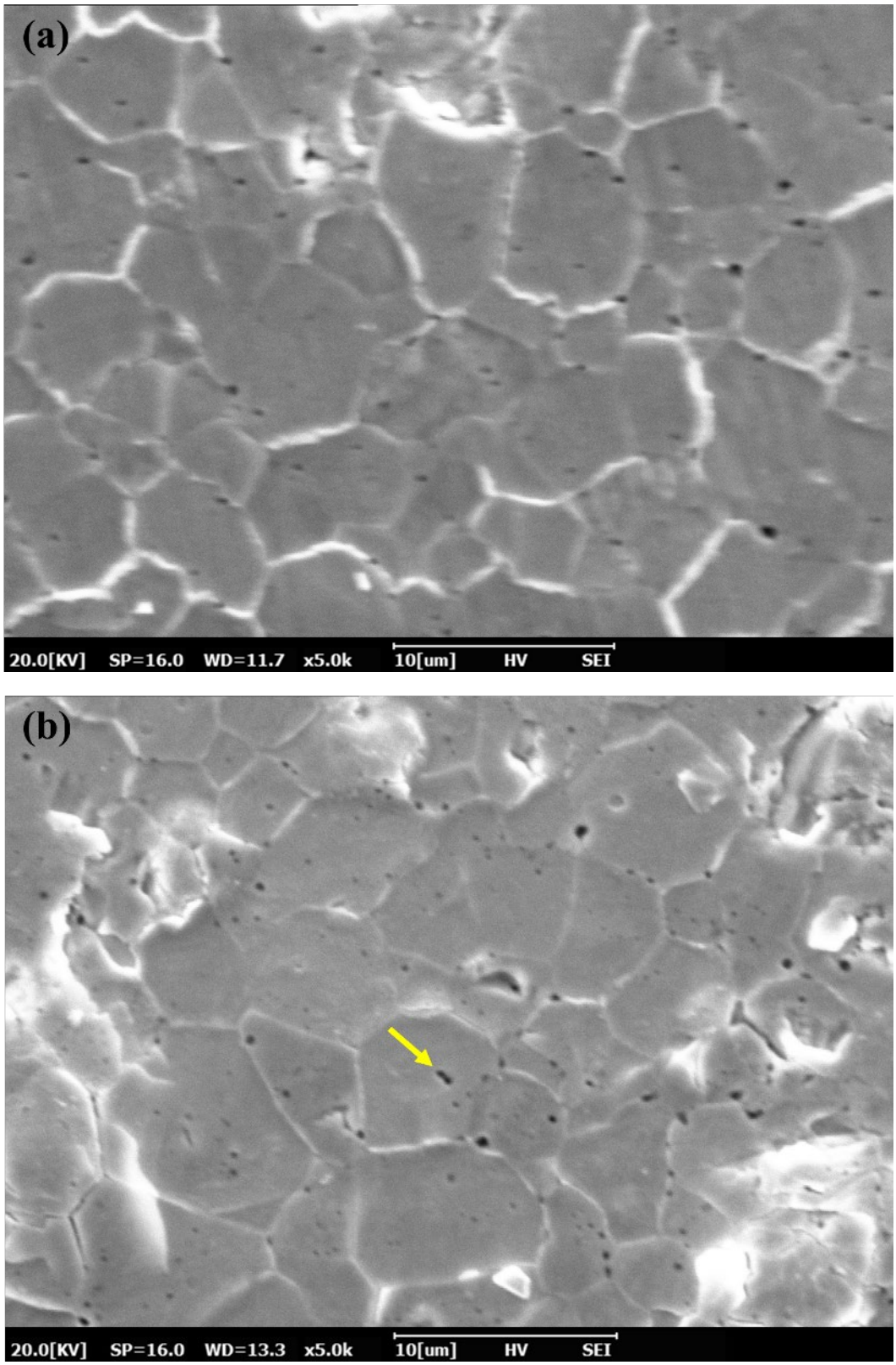

Figure 4-18. SEM images of thermally etched UN pellet surface SPSed at 1800 °C for 30 min under 70 MPa uniaxial pressure (x5,000)

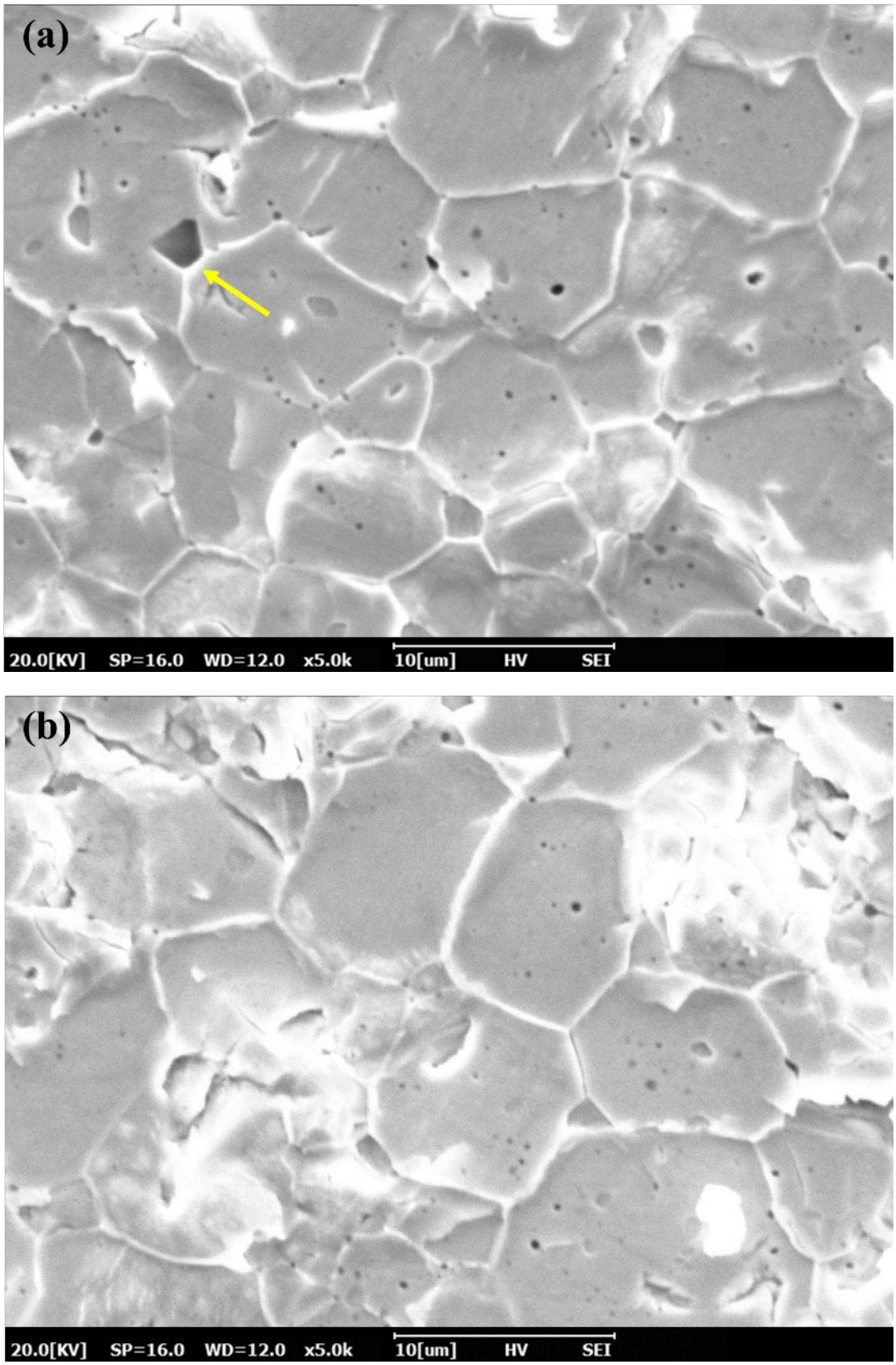

Figure 4-19. SEM images of thermally etched UN pellet surface SPSed at 1800 °C for 60 min under 70 MPa uniaxial pressure (x5,000)

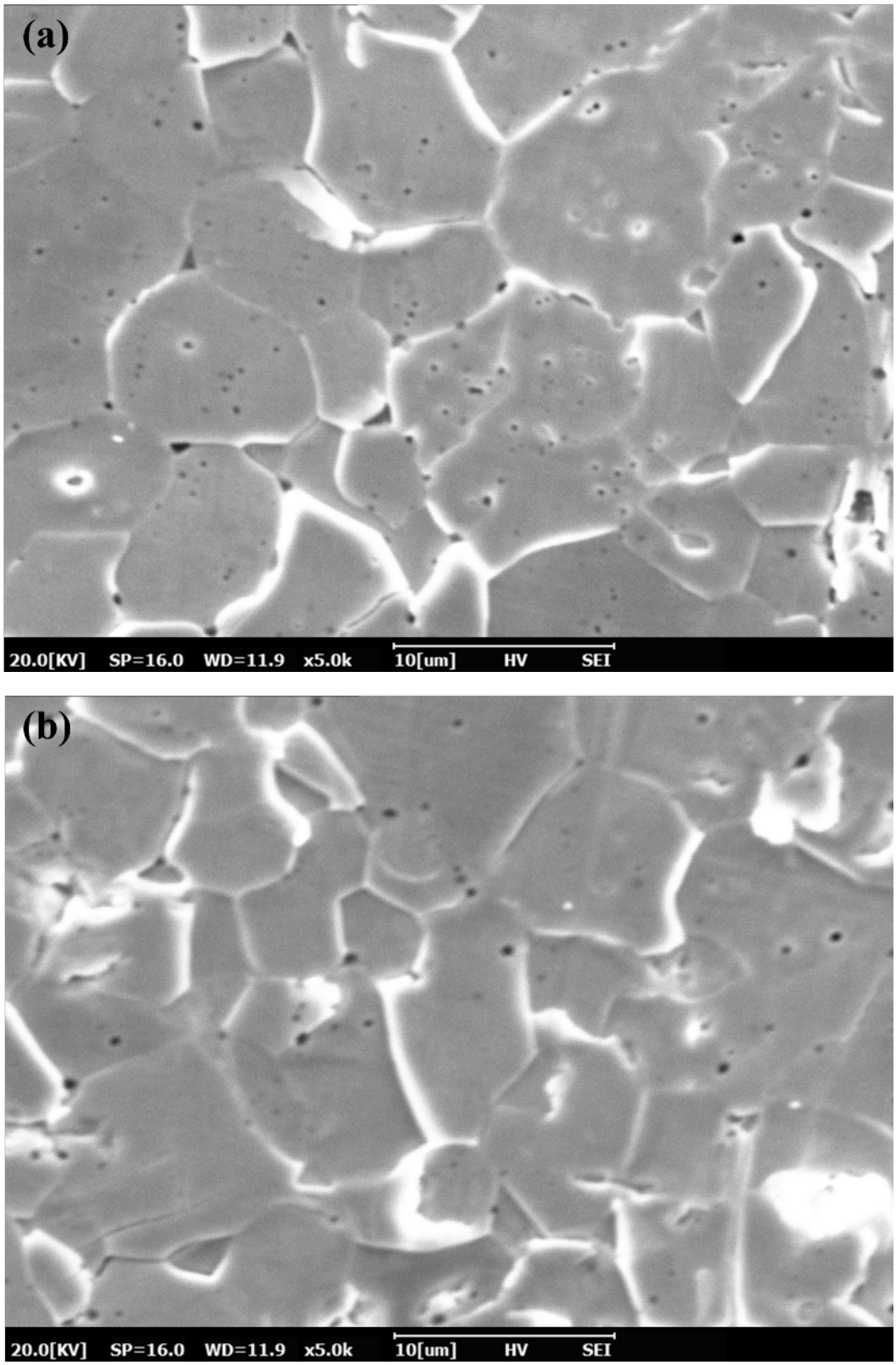

Figure 4-20. SEM images of thermally etched UN pellet surface SPSed at 1800 °C for 180 min under 70 MPa uniaxial pressure (x5,000)

4.1.4. Grain size and grain growth rate

The measured grain sizes of UN pellets are displayed in Table 4-2 and plotted in Figure 4-21 as a function of sintering time. The error bars indicate the standard deviation from three measurements of each sample. The grain sizes of pellets sintered for 10 min at 1600 and 1700 °C were measured to be 2.4 and 2.7 μm, respectively, while the relatively large grain size of 5.8 μm was achieved in the pellet sintered at 1800 °C for the same time. A similar tendency was observed in the pellets sintered for 60 min: grain sizes of pellets were measured to be 3.0, 3.5, and 7.0 μm at sintering temperatures of 1600, 1700, and 1800 °C, respectively. Accordingly, the average growth rates of 0.011, 0.015, and 0.025 μm/min were obtained at each temperature as the dwell time varied from 10 to 60 min, indicating that the growth rate was increased with increasing temperature.

In addition to the sintering temperature, the grain growth rate of pellets sintered at 1800 °C showed a decreasing tendency with increasing dwell time. The average grain growth rate was 0.298 μm/min at early-stage of 5–10 min; however, the rate decreased to 0.009 μm/min with increasing dwell time up to 180 min, which indicates the saturation of the grain size at the later part of SPS process.

Table 4-2. Gran size of the UN pellets with corresponding sintering conditions

	Dwell time (min)				
	5	10	30	60	180
Temperature (°C)	Grain size (μm)				
1500		n/a		2.9	
1600		2.4		3.0	
1700		2.7		3.5	
1800	4.3	5.8	6.7	7.0	8.1

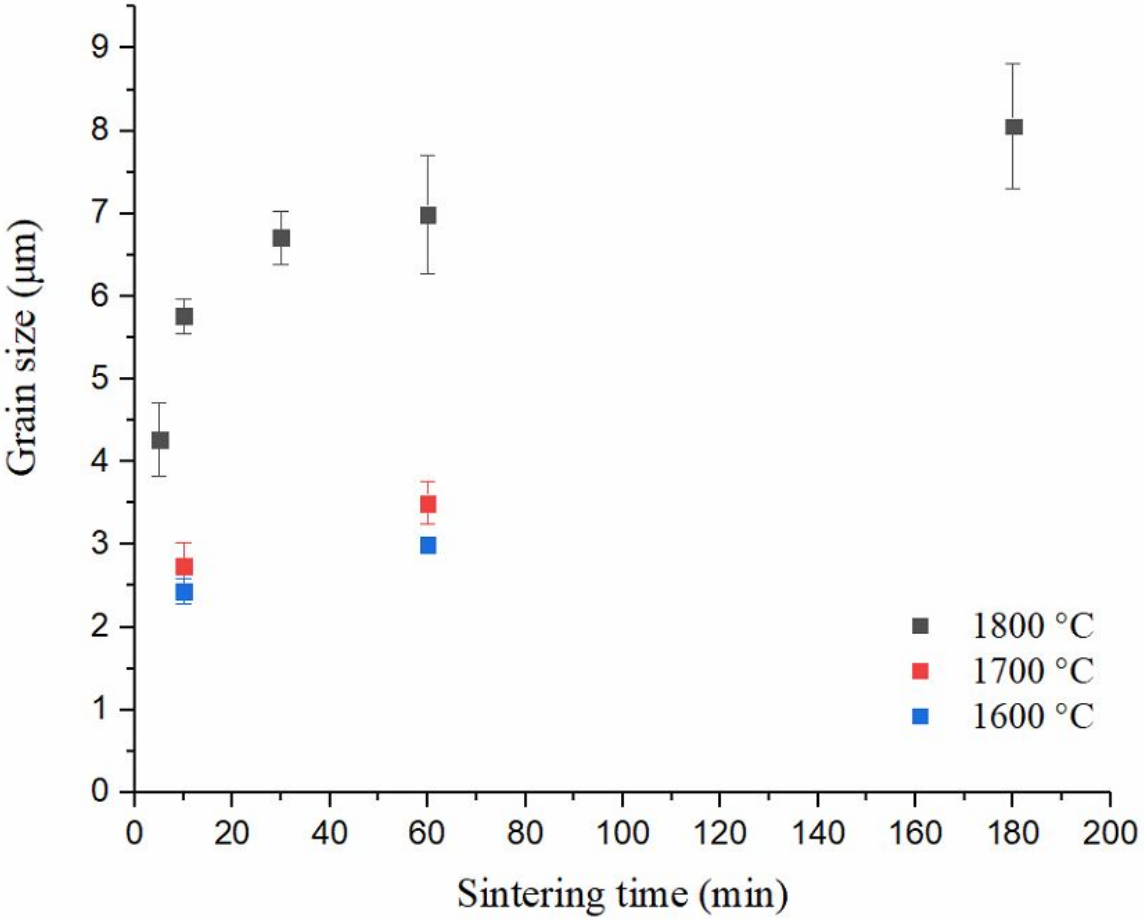

Figure 4-21. Measured grain size of UN pellets as a function of sintering time sintered at 1600 °C (blue), 1700 °C (red), and 1800 °C (grey)

4.2. Gadolinium added UN composite pellets

4.2.1. Density

The measured densities of UN/GdN and UN/Gd_2O_3 composite pellets are displayed in Table 4-3 to 4-5. These values are plotted in Figure 2-1 as a function of the Gd contents. The dashed lines in Figure 2-1 represented 97 %TD of composite pellets at each Gd composition, which were calculated based on the rule of mixtures (described in Section 3.2.2.1.). Most of the sample densities were positioned along the lines, except the UN-38.4wt%GdN pellet sintered at 1800 °C with the relatively low density (93.1 %TD).

4.2.2. Thermal expansion coefficient

Figure 4-23 presents the thermal expansion curves of GdN and Gd_2O_3 measured by DIL as a function of the temperature (from 25 to 1000 °C). For UN, the data reported by Speidel and Keller [90] was plotted instead. Similar values were obtained for all materials: the CLTE of GdN was 8.70×10^{-6}/K; Gd_2O_3, 8.55×10^{-6}/K; and UN, 9.06×10^{-6}/K and the largest difference between the values was less than 6% throughout the temperature range measured. Thus, little thermal stress would have been induced by the CLTE difference during the SPS. This eventually allowed the high-density UN/GdN and UN/Gd_2O_3 composite pellet fabrication without severe crack formation.

Table 4-3. Measured density of the non-solid-solution UN/GdN composite pellets

Sample		non-solid-solution UN/GdN pellet	
Sintering condition	Temperature (°C)	1800	
	Time (min)	10	
	Pressure (MPa)	70	
GdN composition (wt%)	Measured density (g/cm^3)	Theoretical density (g/cm^3)	Relative density (%TD)
0	13.9	14.3	97.2
3.5	13.6	14.1	96.7
7.0	13.3	13.8	96.7
10.7	13.1	13.5	96.7
14.5	12.7	13.2	96.9
38.4	11.0	11.8	93.1
100	9.1	9.2	99.3

Table 4-4. Measured density of the solid-solution UN/GdN composite pellets

Sample		solid-solution UN/GdN pellet	
Sintering condition	Temperature (°C)	2000	
	Dwell time (min)	60	
	Pressure (MPa)	70	
GdN content (wt%)	Measured density (g/cm^3)	Theoretical density (g/cm^3)	Relative density (%TD)
0	n/a	14.3	n/a
3.5	13.4	14.1	95.4
7.0	13.3	13.8	96.5
10.7	13.0	13.5	96.5
14.5	12.8	13.2	95.9
38.4	11.6	11.8	98.1
100	n/a	9.2	n/a

Table 4-5. Measured density of the UN/Gd_2O_3 composite pellets

Sample		non-solid-solution UN/Gd_2O_3 pellet	
Sintering condition	Temperature (°C)	1800	
	Dwell time (min)	10	
	Pressure (MPa)	70	
Gd_2O_3 content (wt%)	Measured density (g/cm^3)	Theoretical density (g/cm^3)	Relative density (%TD)
0	13.9	14.3	97.2
5.0	13.2	13.7	96.1
10.0	12.7	13.1	96.7
15.0	12.2	12.6	96.7
100*	7.4	7.4	99.9

*The pure Gd_2O_3 pellet was prepared at different SPS conditions of 1000 °C and 10 min

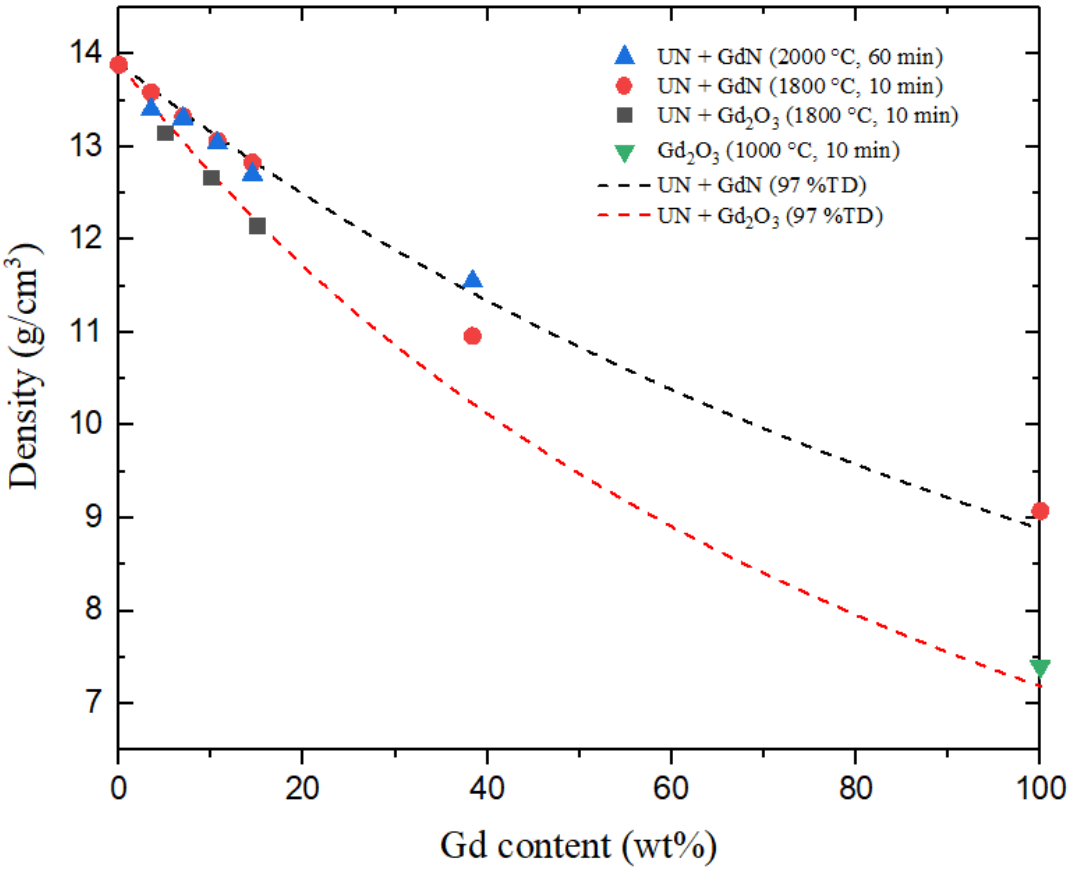

Figure 4-22. Density of GdN and Gd_2O_3 mixed UN pellets with Gd concentration

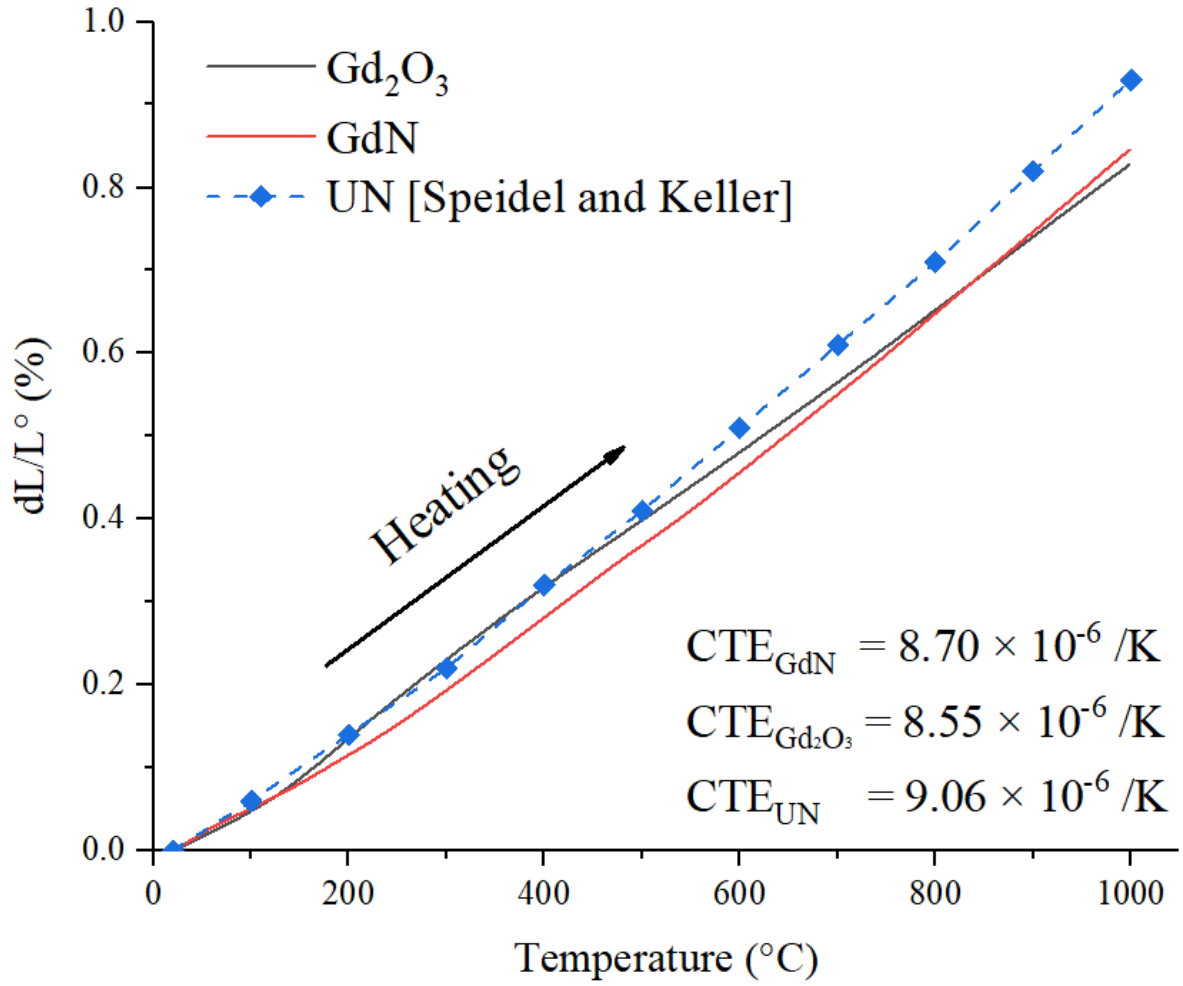

Figure 4-23. Thermal expansion curve of UN, GdN, and Gd_2O_3 as a function of temperature from 25 to 1000 °C

4.2.3. XRD patterns

The normalized XRD patterns of UN/Gd_2O_3 composite pellets are presented in Figure 4-24. The XRD patterns of the composite pellets consisted of pure UN and Gd_2O_3 patterns, which were respectively matched with the ICDD references of UN (PDF #00-032-1397) and c-Gd_2O_3 (PDF#00-043-1014), indicating that two distinct phases of UN and Gd_2O_3 co-existed.

Figures 4-25 and 4-27 respectively show the XRD patterns of the UN/GdN composite pellets SPSed at 1800 °C and 2000 °C. The XRD patterns of pure UN and GdN pellets were well-matched with corresponding ICDD references: PDF#00-032-1397 for UN and PDF#00-015-0888 for GdN. The XRD patterns of all composite samples showed a pure crystal structure of NaCl-type face-centered-cubic (fcc); however, its peak positions were slightly shifted depending on the sintering temperatures and Gd concentrations. The main (200) Bragg peak positions of the UN/GdN samples SPSed at 2000 °C (see Figure 4-26) were moved to low angles with increasing GdN composition, but this type of peak shift was not observed in UN/GdN mixed samples SPSed at 1800 °C (see Figure 4-26). The peak shift to a low angle means the increase of the lattice parameter, thus indicating the U-Gd ion exchange would have occurred during the sintering. These are the clear evidences of the solid-solution $(U_{1-x},Gd_x)N$ phase formation in UN/GdN composite pellets SPSed at 2000 °C.

4.2.4. Lattice parameter

Figure 4-29 presents the lattice parameters of the SPSed pellets with Gd concentration (at%). The dashed line represents the theoretical lattice parameter of solid-solution $(U_{1-x},Gd_x)N$ phase, which was calculated according to Vegard's law using the reference values of UN [91] and GdN [48]. The error bars indicate the standard deviation of the parameters from corresponding diffraction peaks. It is noted that the solid-solution UN/GdN composite pellets (green triangle in Figure 4-29) follow Vegard's law up to 20 at%.

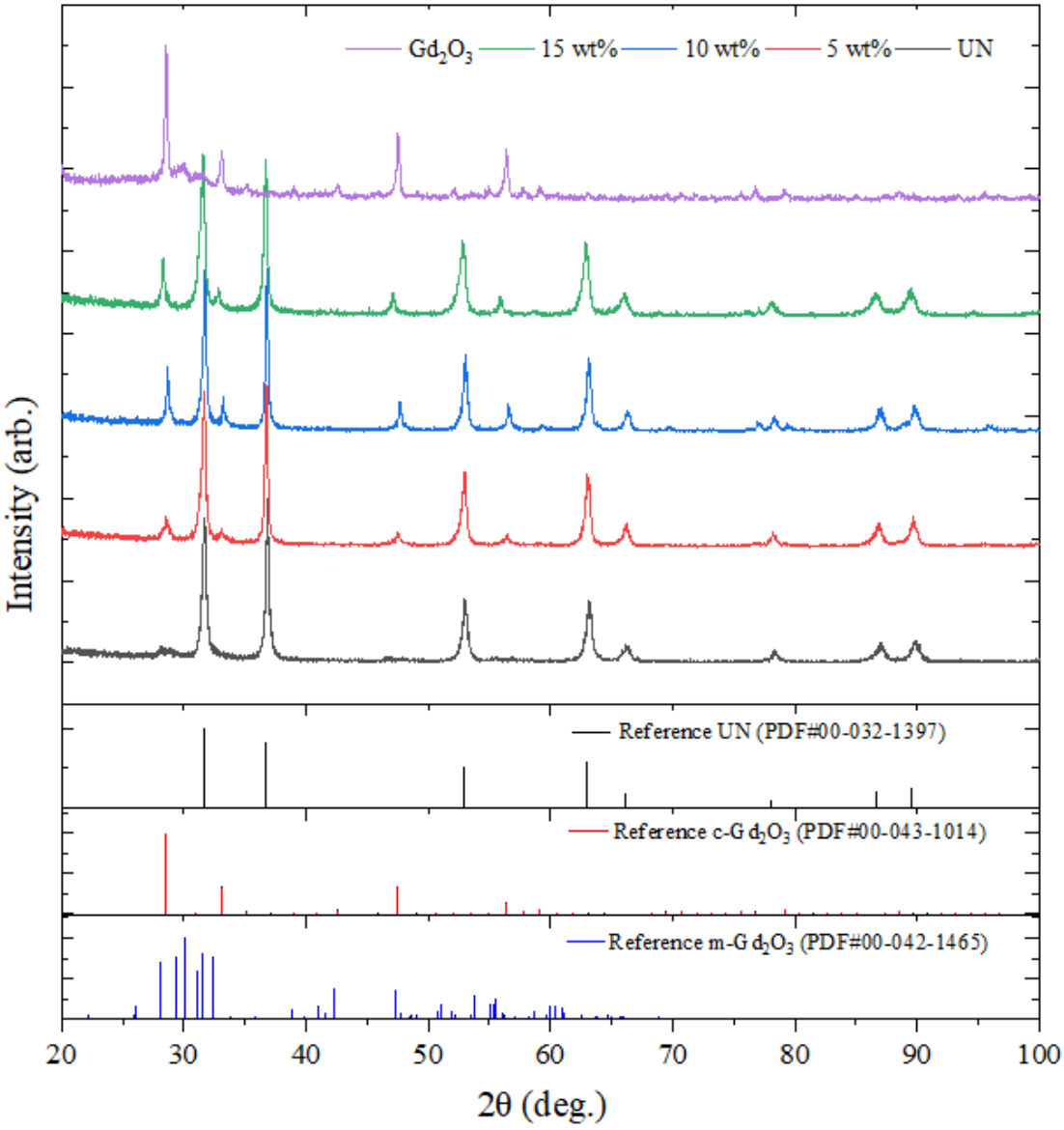

Figure 4-24. Normalized XRD patterns of the UN/Gd_2O_3 composite pellets with various Gd_2O_3 compositions; reference ICDD XRD patterns of UN (PDF#00-032-1397), c-Gd_2O_3 (PDF#00-043-1014), and m-Gd_0O_3 (PDF#00-042-1465) are shown in below.

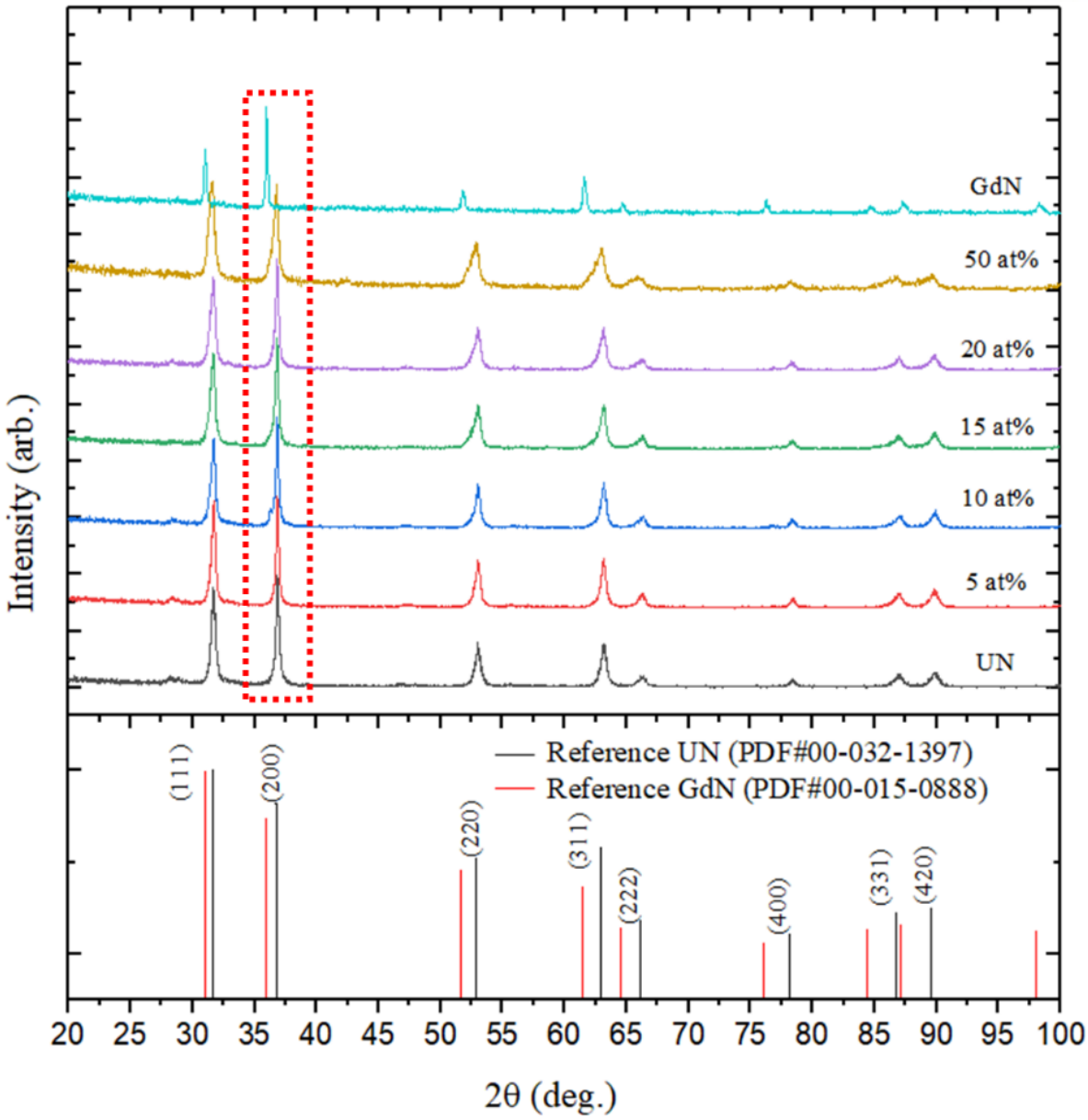

Figure 4-25. Normalized XRD patterns of the UN/GdN composite pellets SPSed at 1800 °C for 10 min with various GdN compositions; reference ICDD XRD patterns of UN (PDF#00-032-1397) and GdN (PDF#00-015-0888) are shown in below.

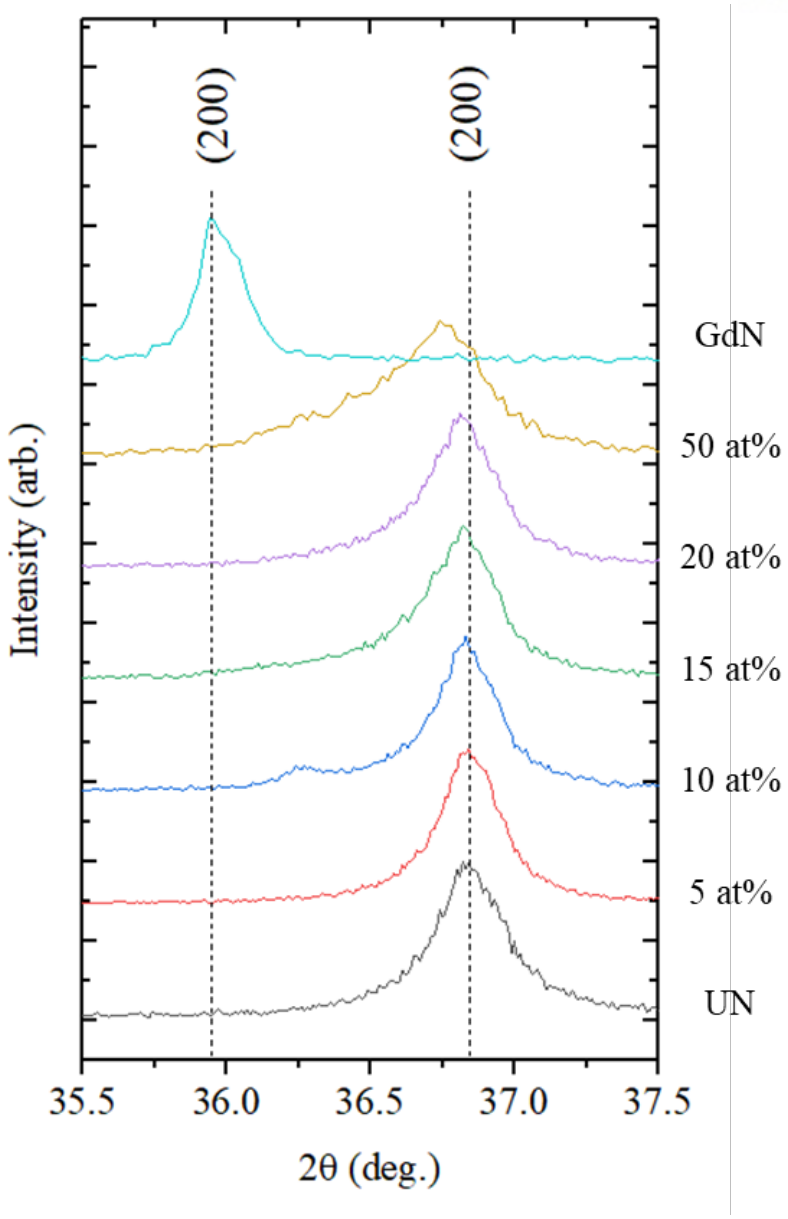

Figure 4-26 Selected XRD peak from (200) plane of UN/GdN composite pellets SPSed at 1800 °C for 10 min shown in red dot box in Figure 4-25.

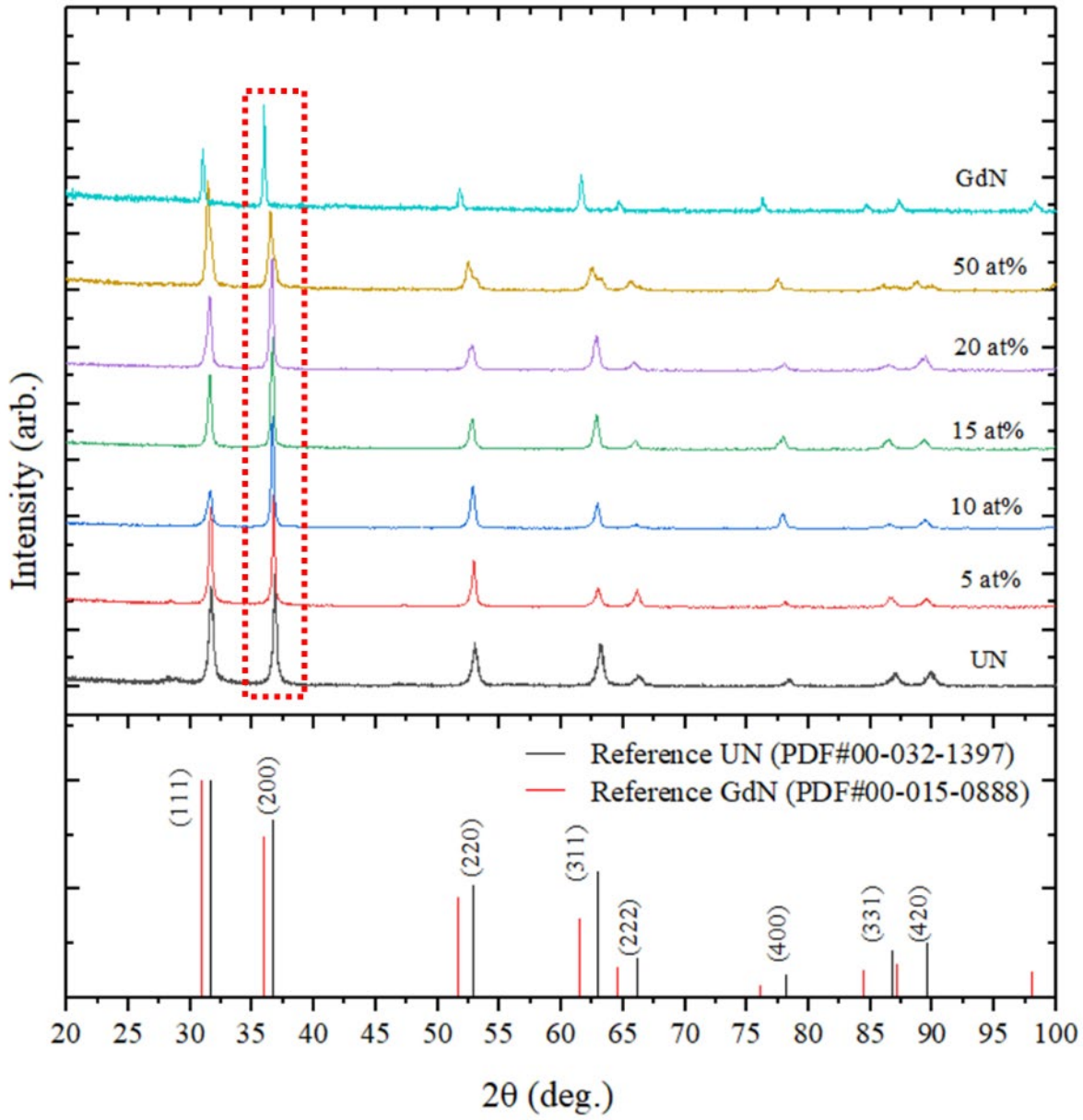

Figure 4-27. Normalized XRD patterns of the UN/GdN composite pellets SPSed at 2000 °C for 60 min with various GdN compositions; reference ICDD XRD patterns of UN (PDF#00-032-1397) and GdN (PDF#00-015-0888) are shown in below.

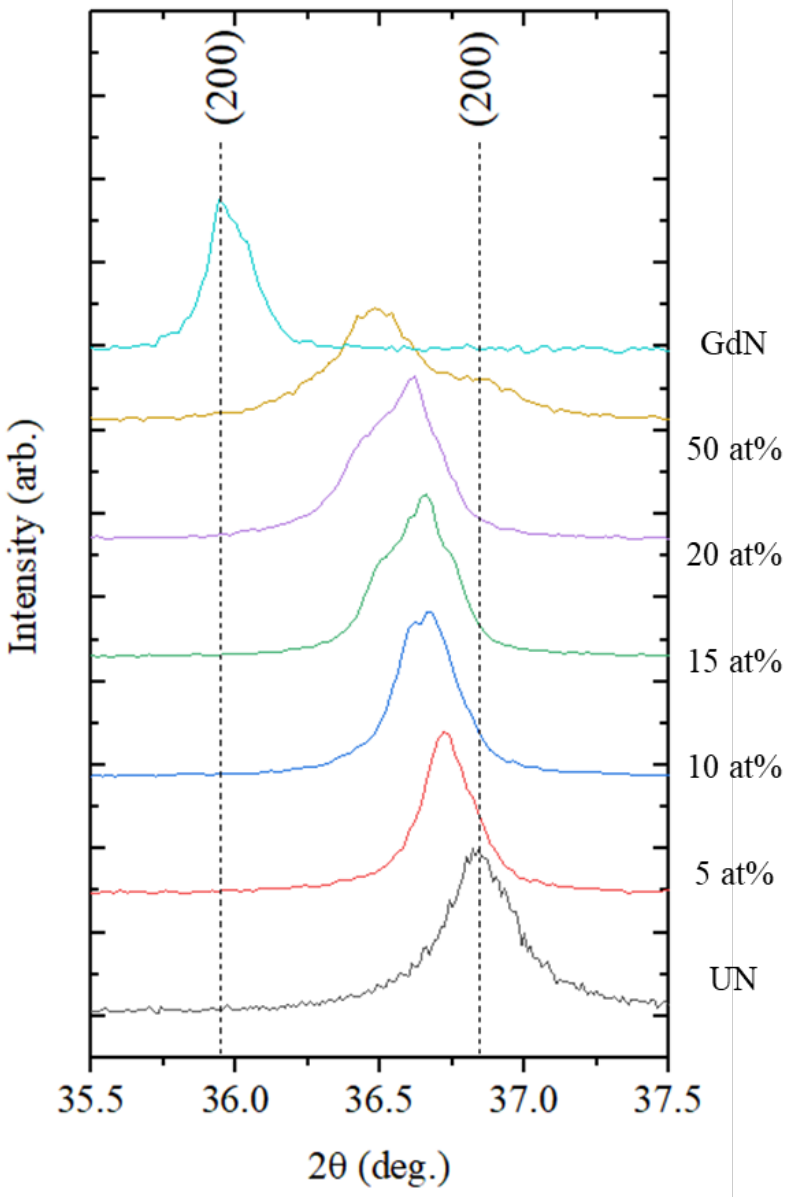

Figure 4-28 Selected XRD peak from (200) plane of UN/GdN composite pellets SPSed at 1800 °C for 10 min shown in red dot box in Figure 4-27

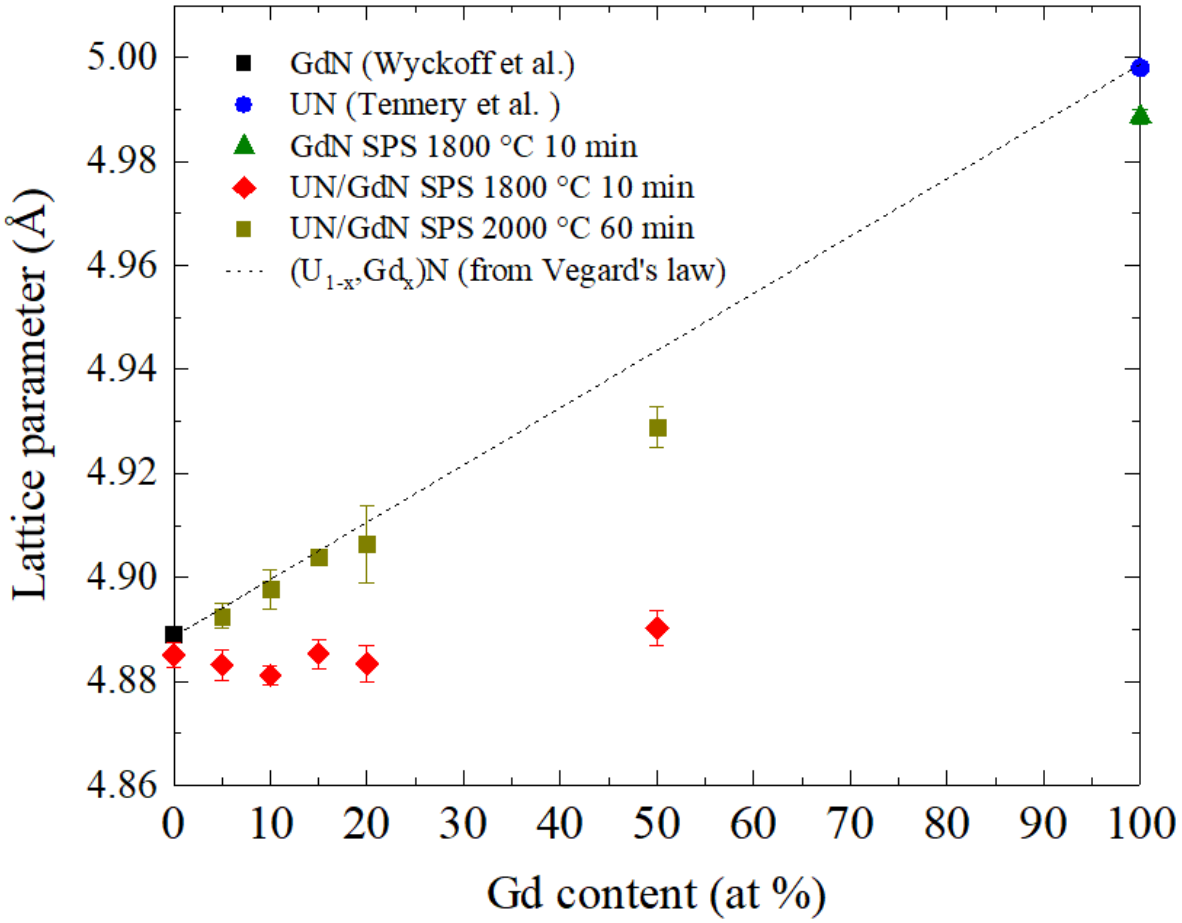

Figure 4-29. Lattice parameter of UN/GdN composite pellets with Gd compositions in at%. Dashed line was plotted according to Vegard's law.

4.2.5. Microstructure

Representative microstructures of gadolinium compounds added UN samples are presented in this section. Figure 4-30 shows the SEM/BSE images of UN/Gd_2O_3 composite pellets. The two-phase microstructures were clearly revealed by the contrast difference between the Gd_2O_3 and UN phases, i.e., the darker contrast for the Gd_2O_3 phase with lower atomic number (Z) density and the brighter contrast for the UN phase with higher Z density. This would support previous XRD results, where XRD peaks of pure UN and Gd_2O_3 were separately observed. Notably, the Gd_2O_3 phase seemed to form a net-like structure, surrounding the UN phases as Gd_2O_3 concentration increased. Also, several pores were presented as black dots.

The microstructures of the non-solid-solution UN/GdN pellets are shown in the SEM/BSE images (see Figure 4-31). The non-solid-solution pellets, which were sintered at the relatively low temperature (1800 °C) for the short-term (10 min), showed the GdN additive particles (darker) and UN matrix (brighter) phases. The microstructures were similar to those found in the previous UN/Gd_2O_3 composite pellets because the phase boundaries between the UN and GdN were clearly distinguishable. However, the agglomeration of the GdN phase may have occurred during the sintering since the size of GdN was comparatively larger than that of the Gd_2O_3 phase at a similar Gd composition. The agglomeration of the GdN phase, thus, enabled to maintain the continuous microstructure of UN matrix for GdN concentration up to 14.5 wt%.

Figure 4-32 shows the solid-solution UN/GdN pellets surface. The solid-solution pellets, sintered at 2000 °C, showed slightly different microstructures to those of non-solid-solution pellets. The boundary between the UN and GdN phases was becoming unclear with increasing GdN contents compared to the previous non-solid-solution UN/GdN samples. In addition, the UN phases seemed to form a dark lamella-like structure (see UN phase in Figure 4-32d). It is also notable that the large pores were more frequently observed in solid-solution pellets than non-solid-solution pellets when the GdN composition increased.

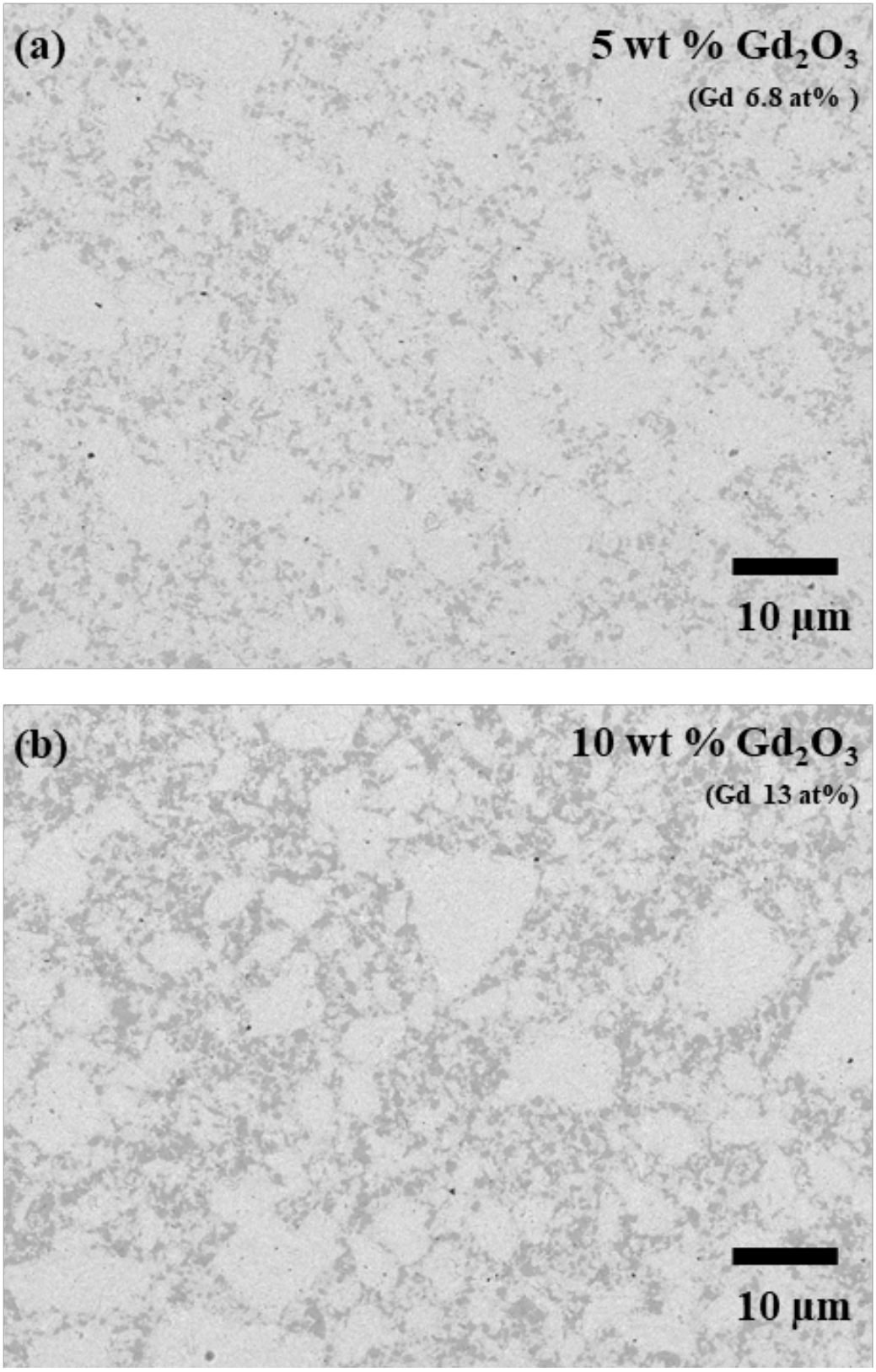

Figure 4-30. SEM images of UN/Gd_2O_3 composite pellet surfaces SPSed at 1800 °C for 10 min with Gd_2O_3 composition of (a) 5 wt%, (b) 10 wt%, and (c) 15 wt%

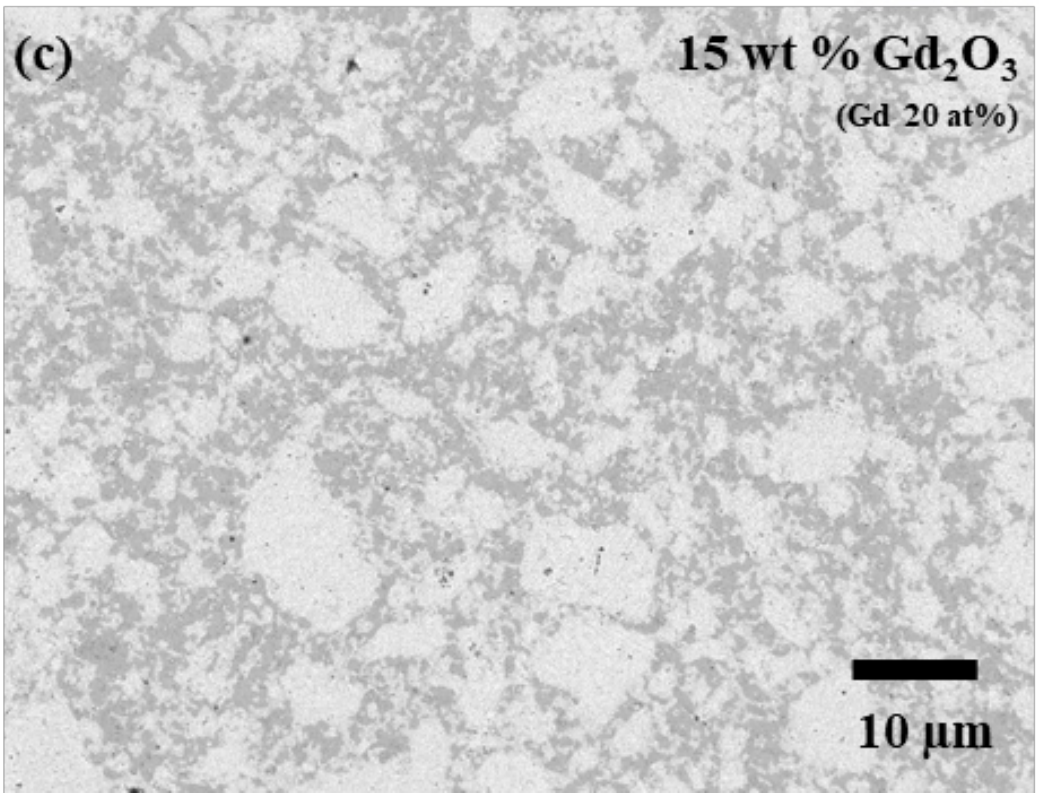

Figure 4-30. Continued

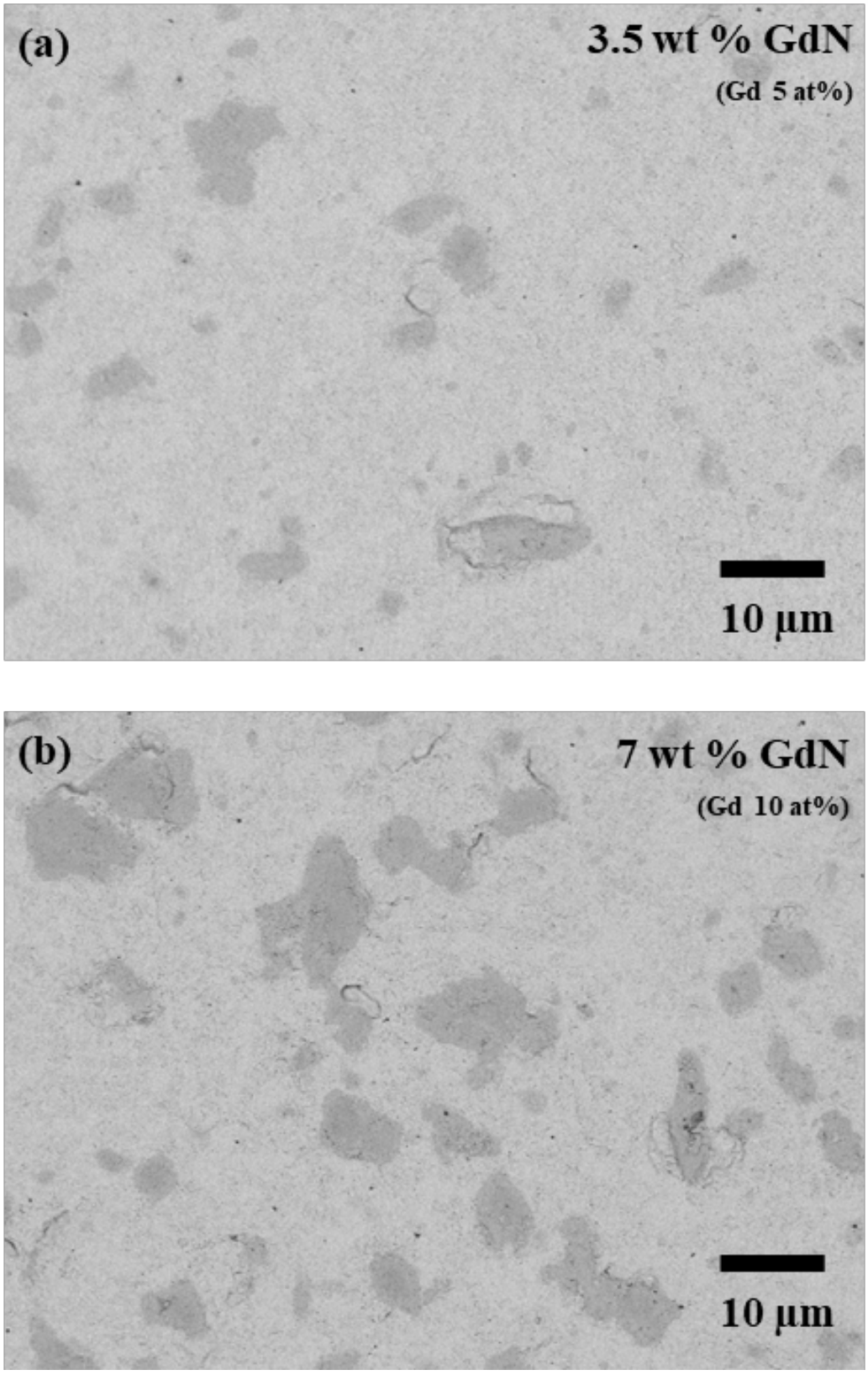

Figure 4-31. SEM images of UN/GdN composite pellet surfaces SPSed at 1800 °C for 10 min with GdN compositions of (a) 3.5 wt%, (b) 7 wt%, (c) 10.7 wt%, (d) 14.5 wt%, and (e) 38.4 wt%

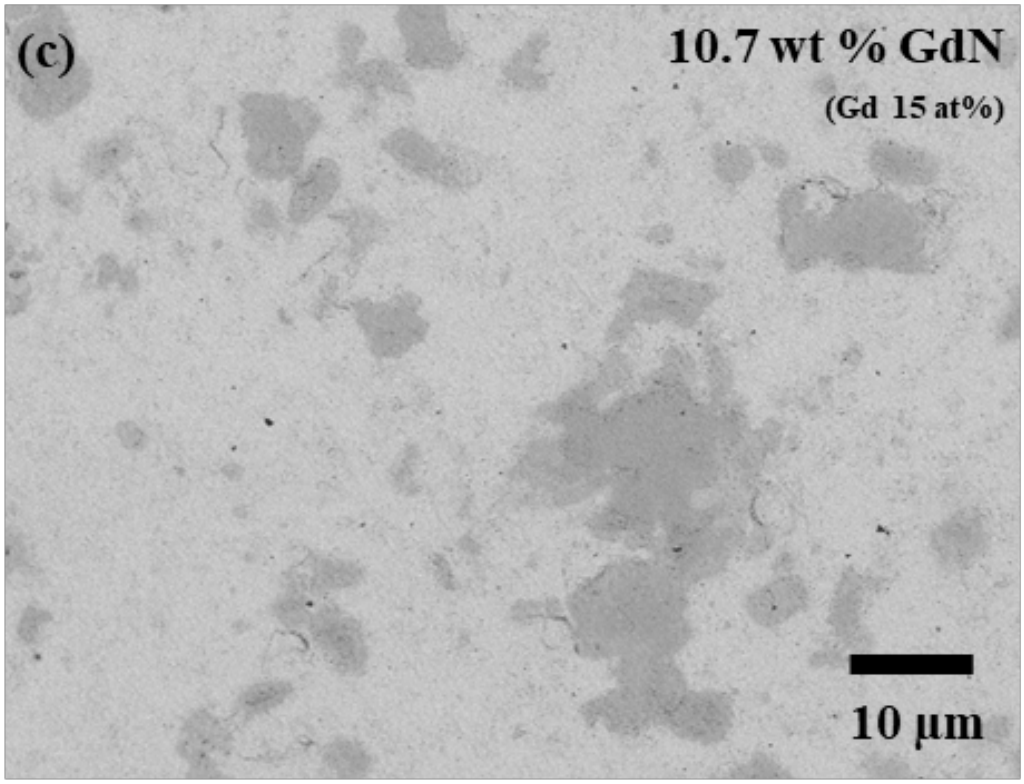

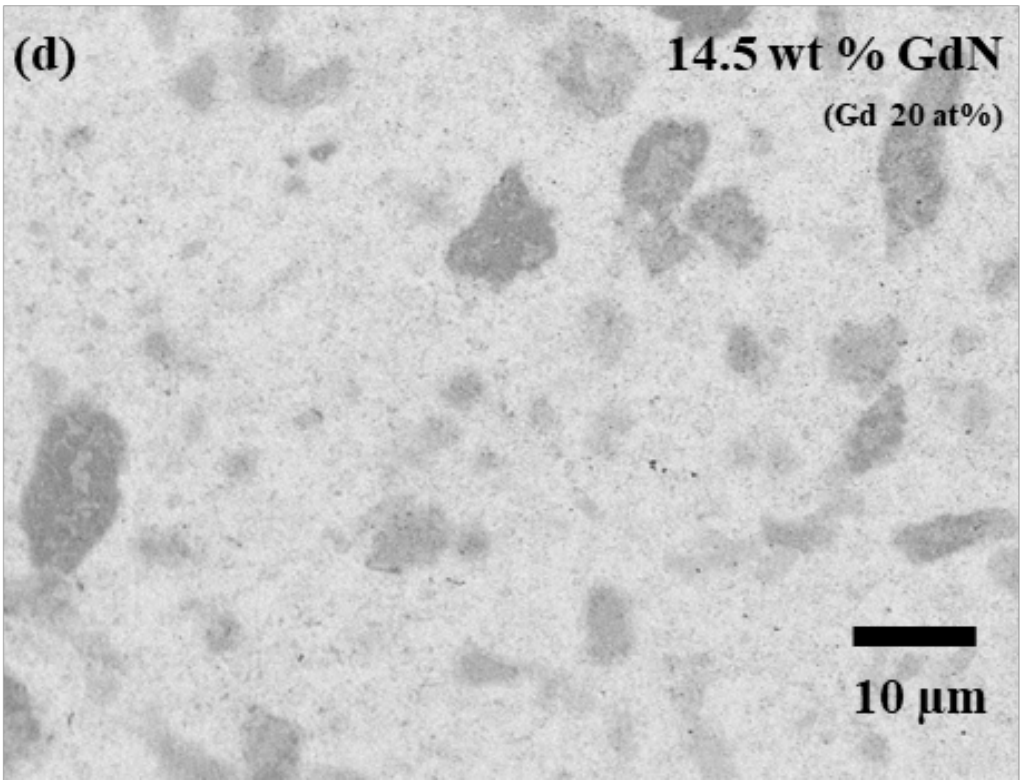

Figure 4-31. Continued

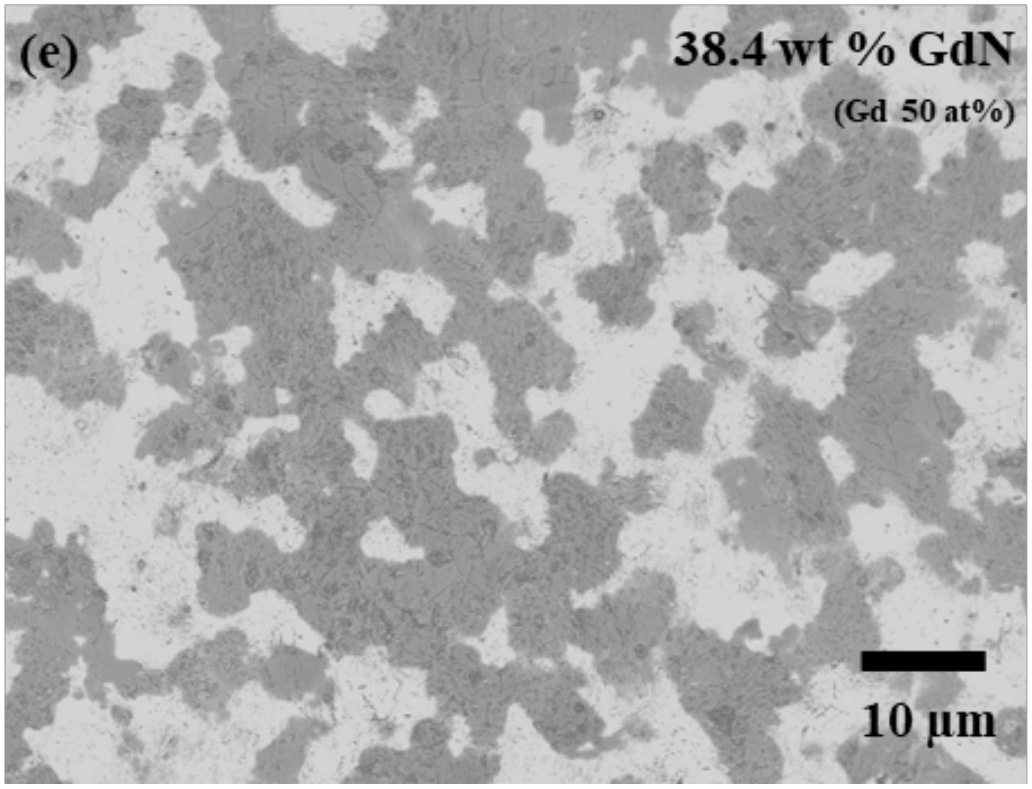

Figure 4-31. Continued

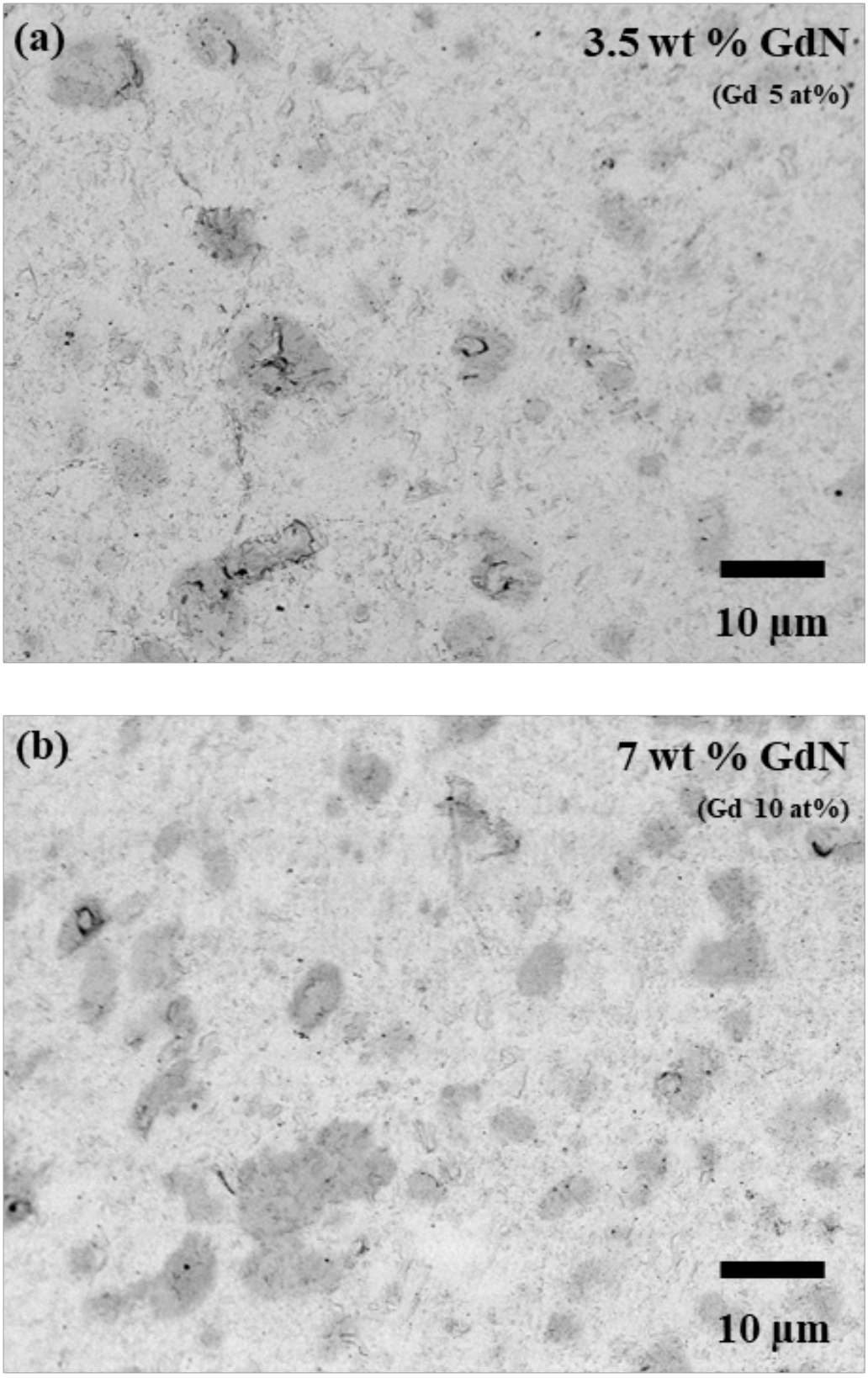

Figure 4-32. SEM images of UN/GdN composite pellet surfaces SPSed at 2000 °C for 60 min with GdN compositions of (a) 3.5 wt%, (b) 7 wt%, (c) 10.7 wt%, (d) 14.5 wt%, and (e) 38.4 wt%

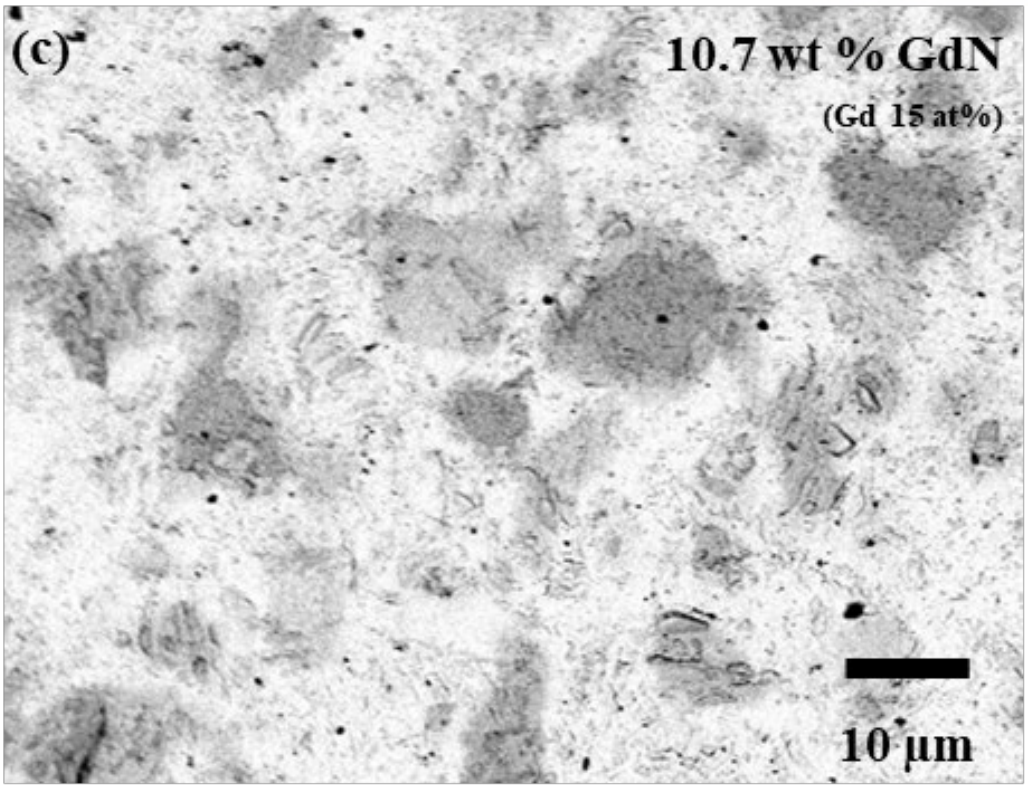

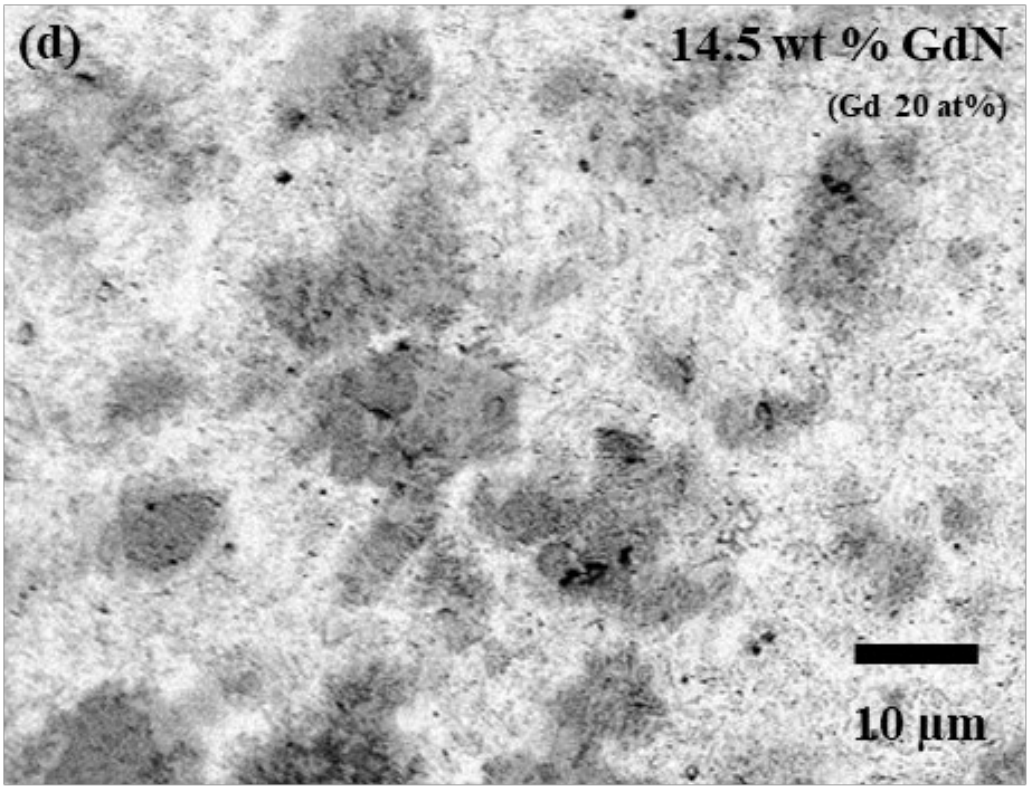

Figure 4-32. Continued

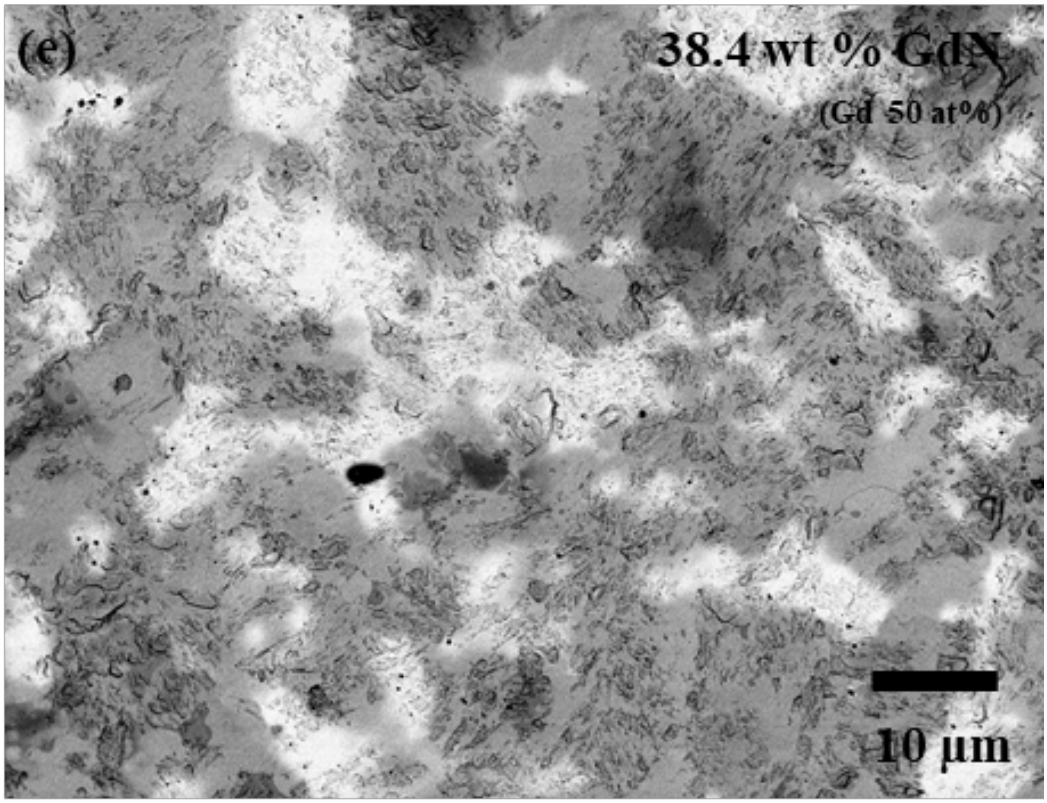

Figure 4-32. Continued

4.2.6. Specific heat capacity

The specific heat capacity of pure UN, GdN, and Gd_2O_3 pellets measured using LFA are presented in Figure 4-33. The heat capacity of samples increased as temperature increased from 25 °C to 1000 °C. Both Gd_2O_3 and GdN exhibited larger heat capacities than UN over the entire temperature range measured. It is worthwhile to note that the heat capacities of the gadolinium compounds were similar to each other. The measured values of UN were well-matched with those from Hayes et al. [60]. On the other hand, the heat capacity of cubic-Gd_2O_3 was lower than the value given by Pankratz [116]. The heat capacity of GdN has not been experimentally measured at high temperature region up to 1000 °C; therefore, this study reports the values for the first time.

The measured heat capacity data were fitted to Maier-Kelley equation [117] as follows:

$$C_p = a + bT + cT^2 + dT^{-2} \tag{4-1}$$

where *a, b, c,* and *d* are constants to be fit and *T* is the temperature (K). The values of parameters are given in Table 4-6. The heat capacities of the composite pellets were obtained with the corresponding mass fractions of UN and Gd compounds according to the Kopp–Neumann rule.

Table 4-6. Parameters of the specific heat capacity fitted in Equation 4-1

Sample	a	b ($\times 10^{-3}$)	c ($\times 10^{-6}$)	d ($\times 10^{3}$)
UN	0.25	-0.11	0.10	-1.63
Gd_2O_3	0.31	-0.10	0.11	-0.98
GdN	0.30	-0.02	0.06	-1.19

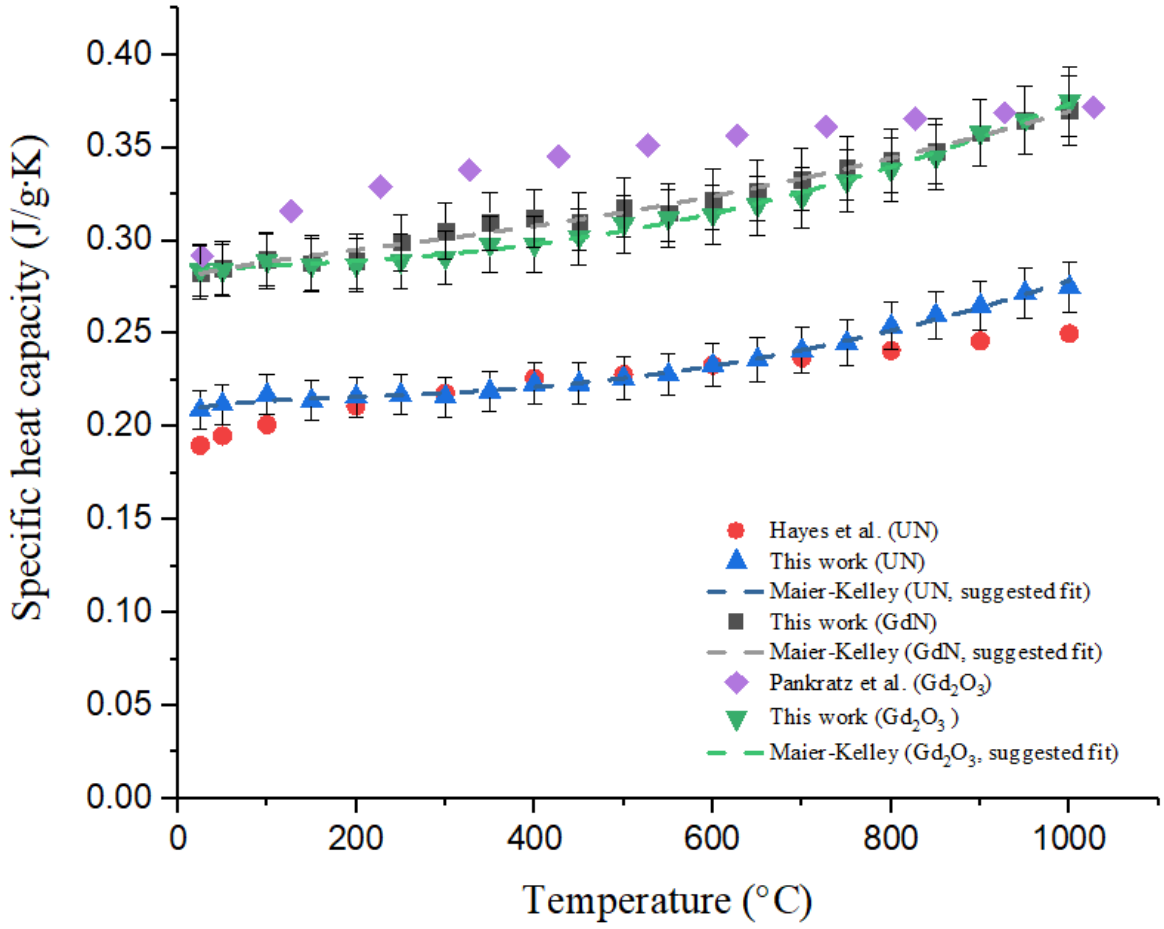

Figure 4-33. Specific heat capacity of UN, GdN, and Gd_2O_3 measured by LFA. Dashed lines are drawn according to the Maier-Kelly equation.

4.2.7. Thermal diffusivity

The thermal diffusivity of gadolinium compounds added UN pellets are shown in Figure 4-34 to 4-36 with the temperature range from 25 to 1000 °C. The measured data are given in Tables B-2 to B-4. In general, the UN/Gd_2O_3 pellets exhibited lower thermal diffusivities than both UN/GdN composite pellets. As an example, the thermal diffusivity of non-solid-solution UN-10.7wt%GdN pellets was ~23% higher than that of the UN-10.0wt%Gd_2O_3 at 25 °C. The difference between those values increased with increasing temperature: the thermal diffusivity of the non-solid-solution UN-10.7wt%GdN pellets was ~43% higher than that of the UN-10.0wt%Gd_2O_3 at 1000 °C. More notably, the difference between those values also increased with increasing Gd concentration: the thermal diffusivity of UN-14.5wt%GdN pellets was 44–79% higher than that of UN-15wt%Gd_2O_3 with increasing temperature from 25 °C to 1000 °C. The non-solid-solution UN/GdN pellets exhibited 13–23% higher values than solid-solution UN/GdN pellets at the same GdN concentration.

4.2.8. Thermal conductivity

The calculated thermal conductivities of gadolinium compounds added UN pellets are displayed in Figures 4-37 to 4-39. The measured data are given in Tables B-6 to B-8. The thermal conductivity of composite pellets showed a similar tendency with thermal diffusivity. The solid-solution UN-14.5wt%GdN pellet showed 20–65% higher thermal conductivity than the UN-15wt%Gd_2O_3 pellets. In general, the non-solid-solution UN/GdN pellets exhibited 16–25% higher thermal conductivity than the solid-solution containing UN/GdN pellets.

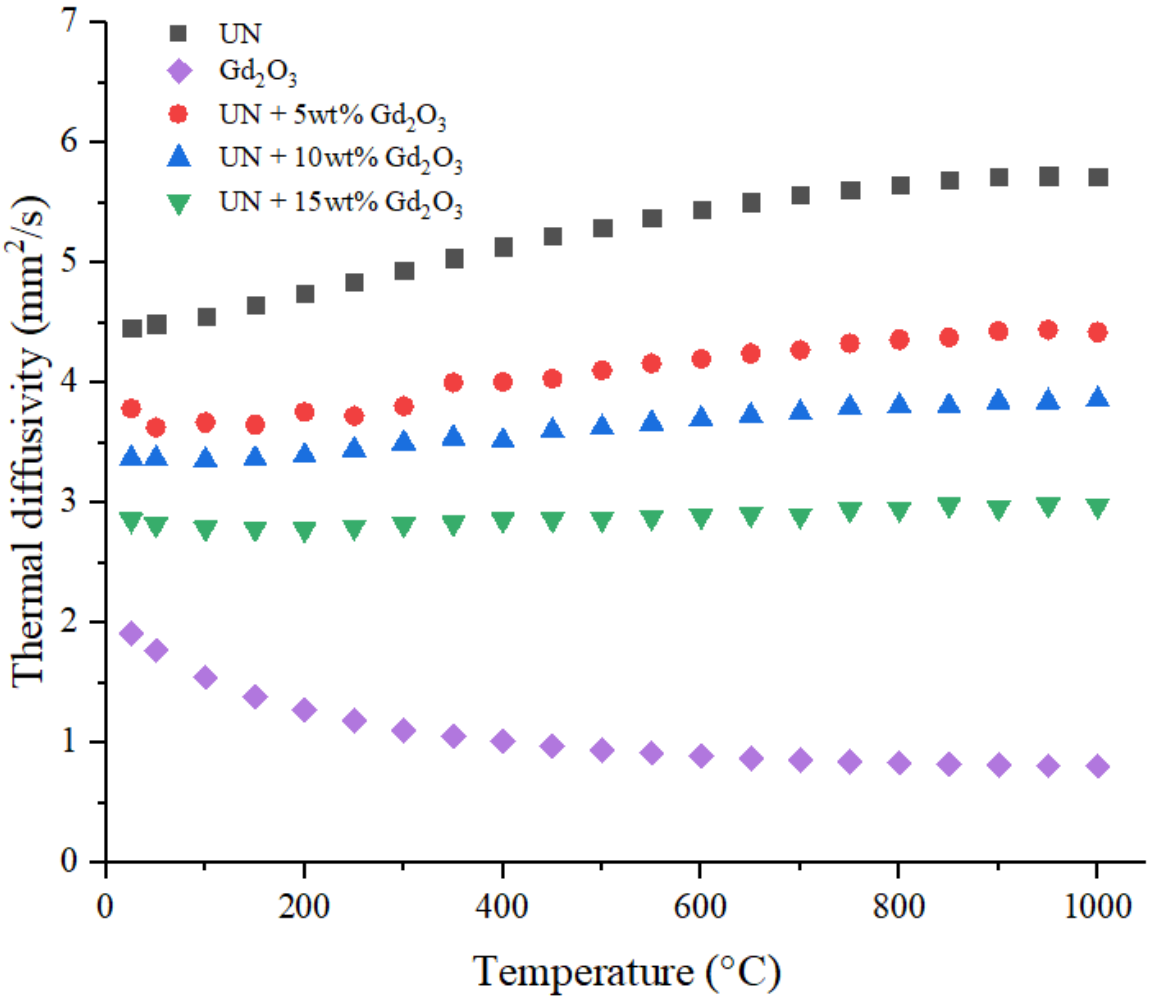

Figure 4-34. Thermal diffusivity of SPSed UN/Gd_2O_3 composite pellets (1800 °C, 10 min)

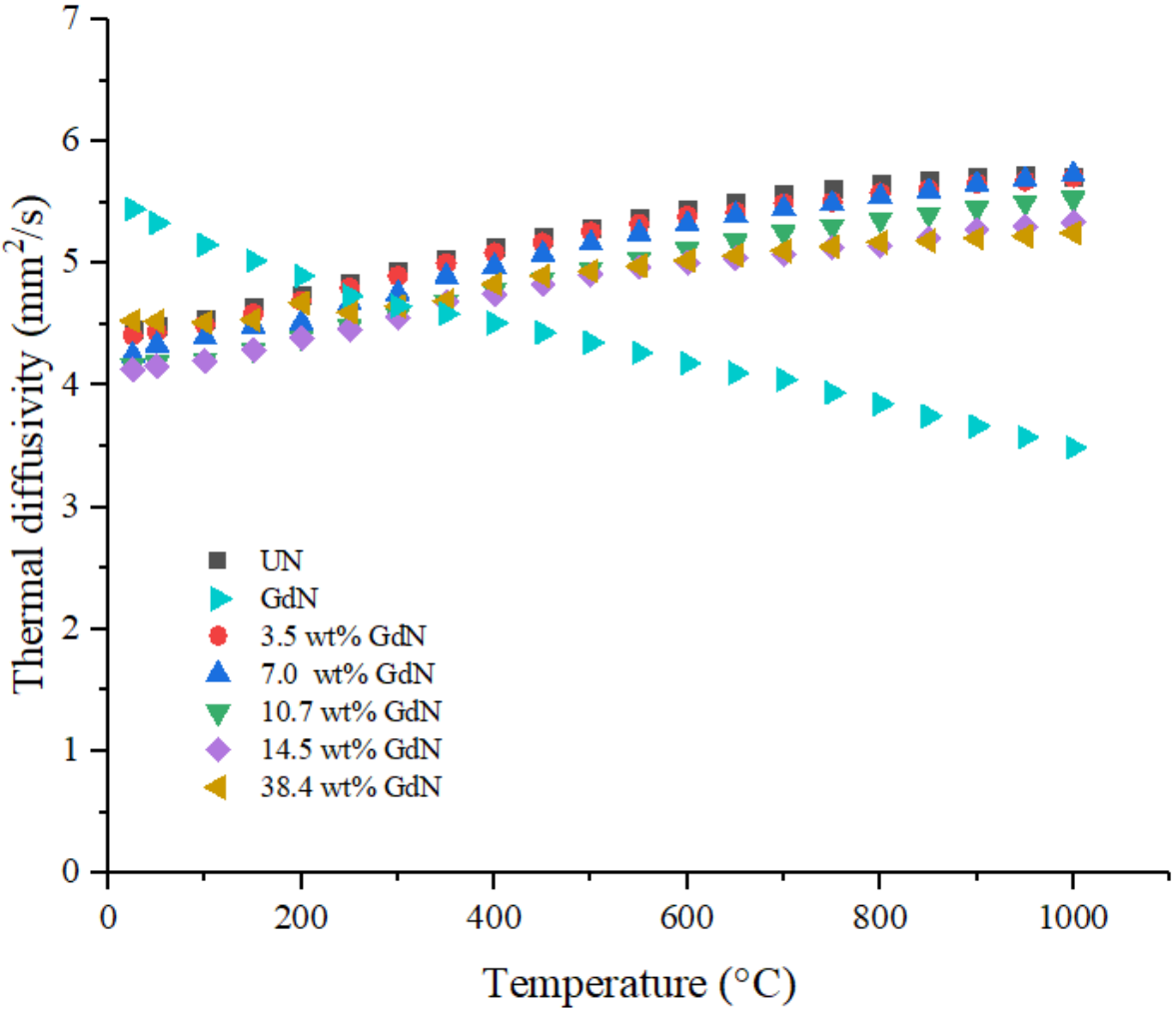

Figure 4-35. Thermal diffusivity of SPSed UN/GdN composite pellets (1800 °C, 10 min)

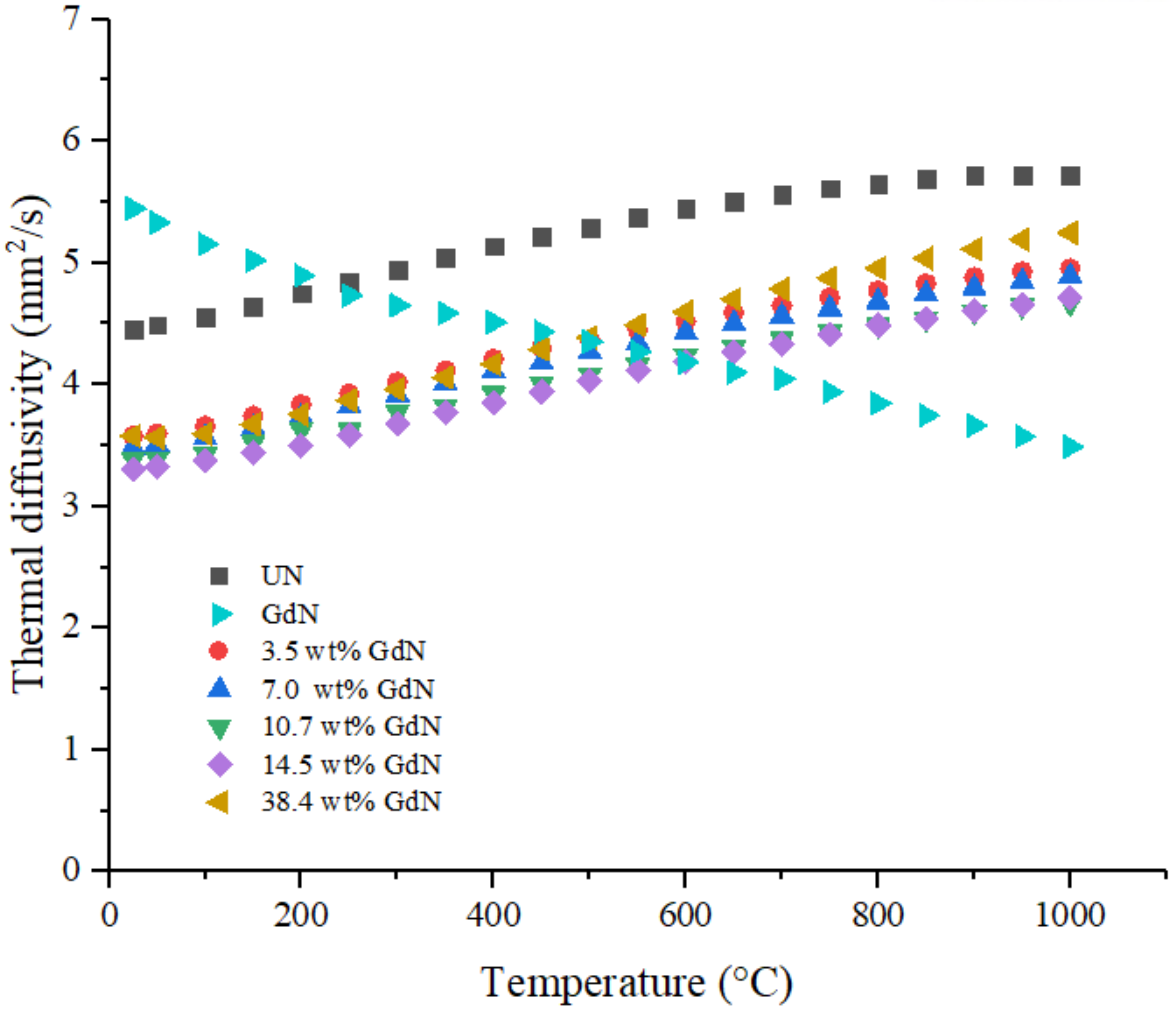

Figure 4-36. Thermal diffusivity of SPSed UN/GdN composite pellets (2000 °C, 60 min)

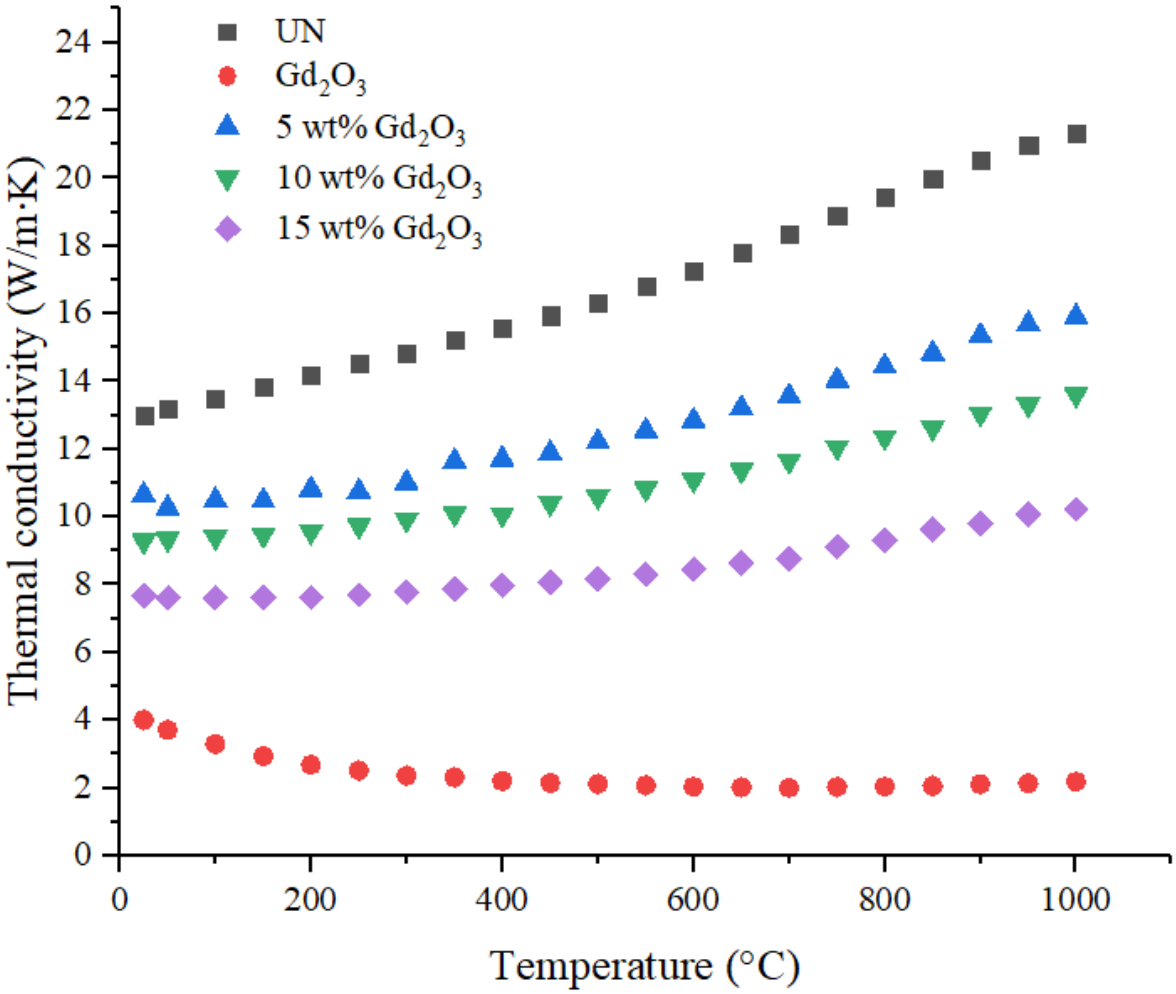

Figure 4-37. Thermal conductivity of SPSed UN/Gd_2O_3 composite pellets (1800 °C, 10 min)

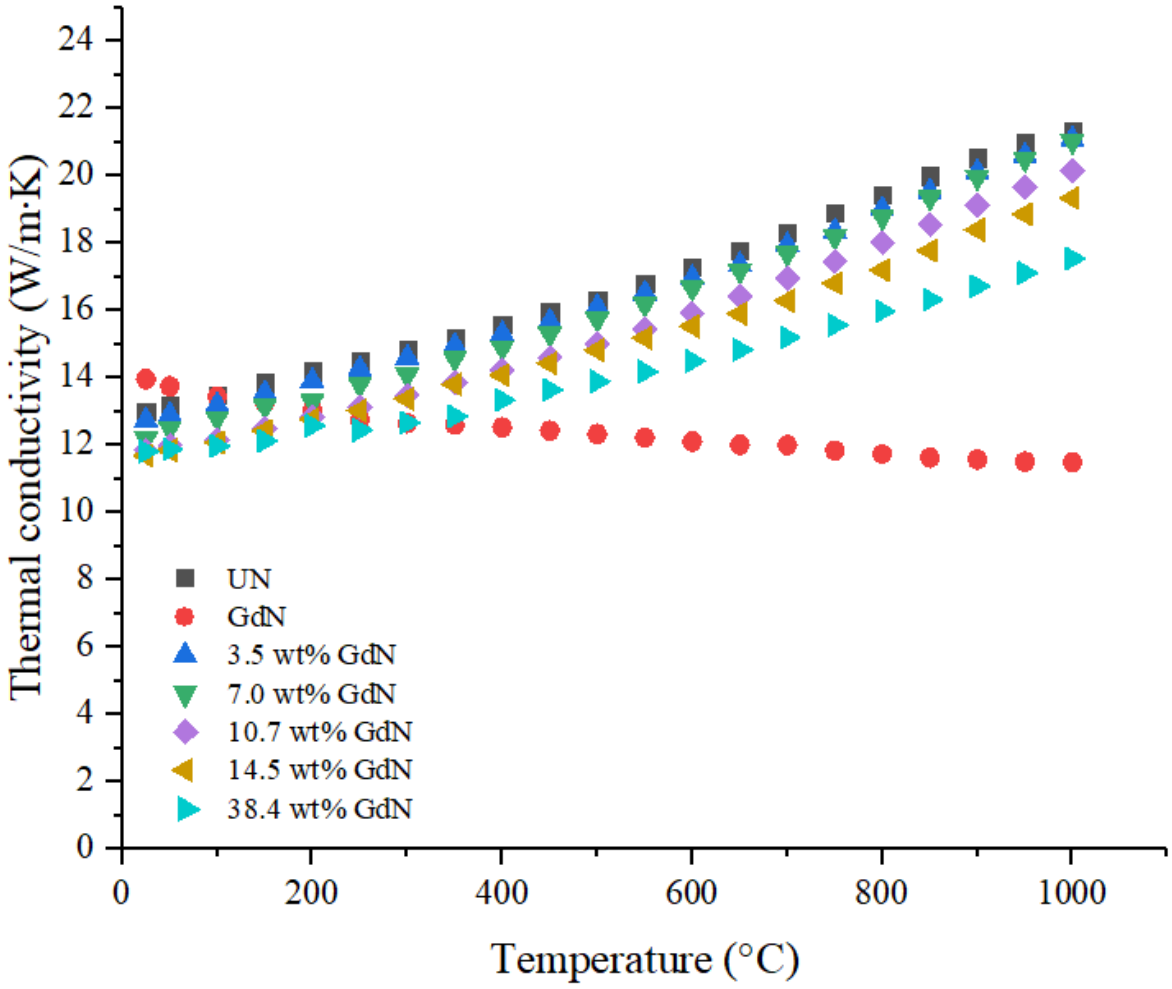

Figure 4-38. Thermal conductivity of SPSed UN/GdN composite pellets (1800 °C, 10 min)

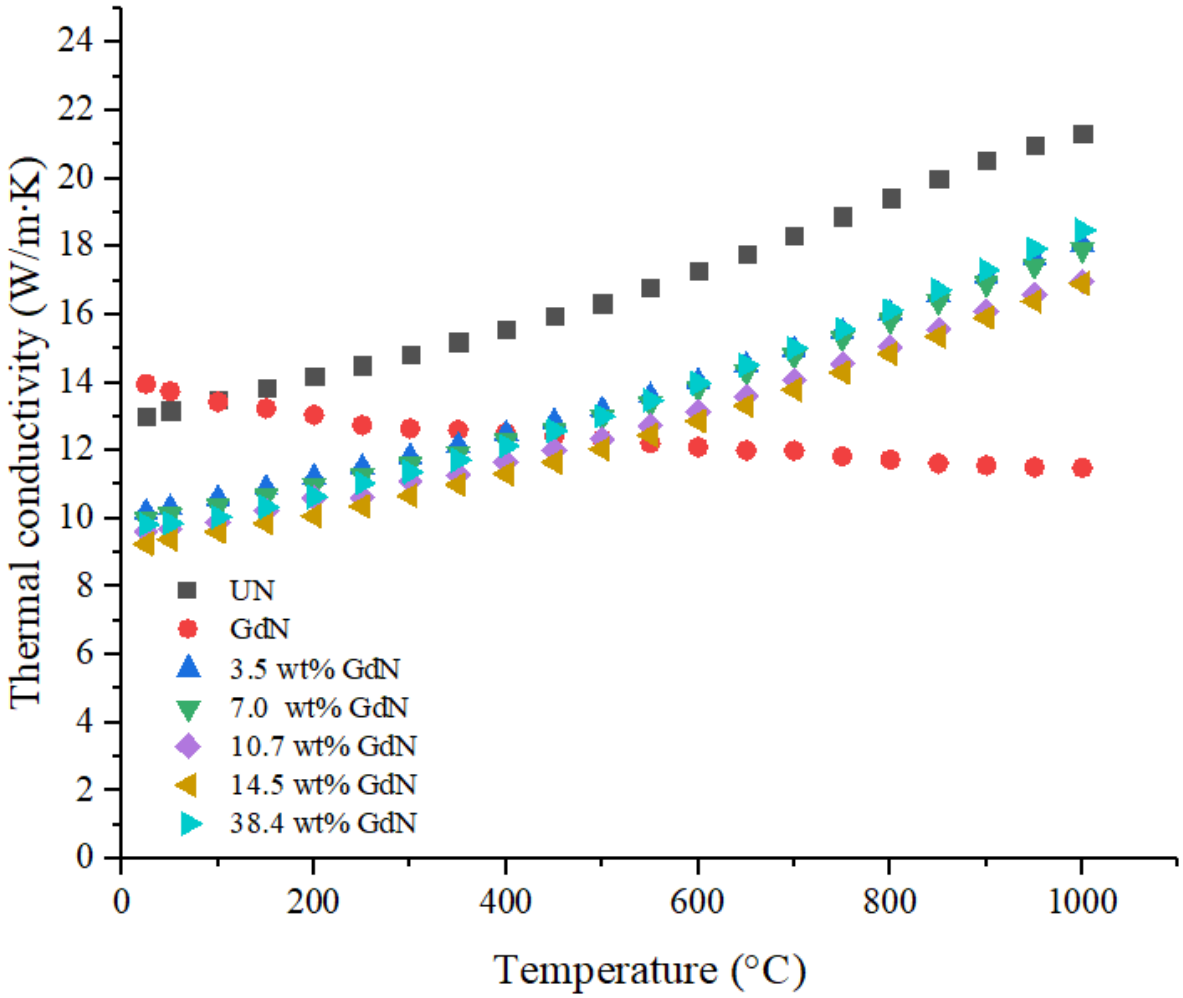

Figure 4-39. Thermal conductivity of SPSed UN/GdN composite pellets (2000 °C, 60 min)

Chapter 5. DISCUSSION

5.1. SPS behavior of pure UN powder

5.1.1. Crystal structure of SPSed UN pellets

The XRD patterns of UN pellets (yellow line in Figure 4-1) showed the relatively increased peak intensity of (200) plane, indicating that the crystal structure of the pellet was preferentially orientated along the plane perpendicular to the sample surface. This type of texture might have been formed during SPS due to uniaxial pressure applied on the pellets, hence unavoidable. However, the texture can be expected to have a limited impact on the irradiation performance of the UN fuel, considering its isotropic crystal structure (cubic, Fm-3m) and swelling characteristics.

The lattice parameter calculated from the XRD data of the UN pellet was slightly lower (~0.2%) than that of the reference. In general, this type of lattice parameter deviation in sintered pellets could occur for two reasons: (1) impurities (carbon and oxygen) in samples and (2) the nitrogen to uranium metal (N/U) ratio change (i.e., the formation of the non-stoichiometric UN phase). According to Muromura and Tagawa [88], the lattice parameter of UN increases with increasing carbon and oxygen contents; however, its effect is negligible since the value increases only 0.02% for UN pellets with high carbon content (0.07 wt%). It is thus likely that the decrease of the lattice parameter in this study had occurred due to the formation of the non-stoichiometric UN phase. It was revealed by Benz and Bowman [118] that UN exhibits hypo-stoichiometric UN_{1-x} phase with the N/U ratio equal to or less than 0.92 ± 0.02 over 1800 °C. Although the effect of the N/U ratio on the lattice parameter change for UN has not been studied or reported previously; however, its effect could be hinted from other nitrides with the same crystal structure. Typically, the lattice parameters of NaCl structure nitrides such as niobium nitride (NbN) [119] and molybdenum nitride (MoN) [120] decrease with decreasing nitrogen to metal ratio. For UN, thus, the decrease of the lattice parameter with decreasing N/U ratio is highly anticipated. This could be further investigated with the development of accurate N/U ratio measurement methods.

5.1.2. Effect of pore distribution on maximum density achieved

For UN pellets with a density over 90 %TD, small isolated pores were mostly observed at grain boundaries and triple junctions, while some pores separated from grain boundaries forming intragranular pores. The presence of intragranular pores suggests that pore-grain boundary separation may have occurred. The maximum density achievable under current sintering conditions (~97 %TD) can be explained by the presence of intragranular pores since these types of pores are hardly eliminated by sintering. This can be further strengthened by the appearance of two adjacent pores, shown in Figure 4-18b (yellow arrow), indicating that the further growth of intragranular pores may also have occurred.

Another possible consideration given on the maximum UN pellet density achievable was the presence of the large trapezoidal void shown in Figure 4-19b (yellow arrow). The trapezoidal void observed in the UN pellet is similar to the Wulff-shaped void in UO_2 crystals, which are normally formed at an extremely high temperature; according to Castell [121], a high annealing temperature over 2100 °C was typically required to form the Wulff shape in UO_2 pellets. For UN pellets, however, there is no experimental study available regarding this type of void formation. The maximum sintering temperature of 1800 °C used in this study implies that Wulff shape voids could be formed in UN even at a lower temperature. Thus, further investigation is required to assess the formation of this type of void and its effects on the maximum UN pellet density obtainable from SPS.

5.1.3. Time- and temperature-dependent SPS behavior

To visualize the effect of time and temperature on SPS behavior, the grain sizes are organized as a function of pellet density as shown in Figure 5-1. The grain size-density trajectory graph clearly reveals two separate SPS stages in accordance with the sintering temperature. With increasing sintering temperature up to 1700 °C, the density of the pellets increased until it reached the maximum value (~97 %TD) without any significant grain growth. On the contrary, at the sintering temperature of 1800 °C (green triangle in Figure 5-1), pellets were rapidly densified up to 97 %TD within 5 min, and considerable grain growth was observed as dwell time increased up to 180 min. The result indicates that that the threshold temperature for densification would lie between 1700 and 1800 °C.

5.1.4. Effect of pressure and particle size on SPS behavior

The effect of sintering pressure could be glimpsed from the similar study [38], where UN pellets were sintered under various pressures (45, 90, and 135 MPa) using SPS. In the previous study, the grain size increased with increasing pressure at a relatively low-pressure region (< 90 MPa), while the grain growth was suppressed at high pressure of 135 MPa. Thus, the large grain size (~31 μm) of the pellet was obtained under 90 MPa at a sintering temperature of 1650 °C for 15 min; however, this value is much larger than even the largest grain size (~8 μm) of this study, obtained at the sintering temperature of 1800 °C for 180 min under 70 MPa. Therefore, it seems that threshold sintering pressure for grain growth could exist between 70–90 MPa.

Additionally, the difference in final grain size could be further explained by the effect of the particle size distribution (PSD) on the microstructure of sintered pellets. Bjork et al. [122] demonstrated, from the kinetic Monte Carlo model of solid-state sintering, that compacts sintered from a powder with broader PSD exhibited a small grain size compared to that from narrower PSD. The wide range of UN powder PSD (1–20 μm) used in this study, therefore, may have resulted in the smaller grain size.

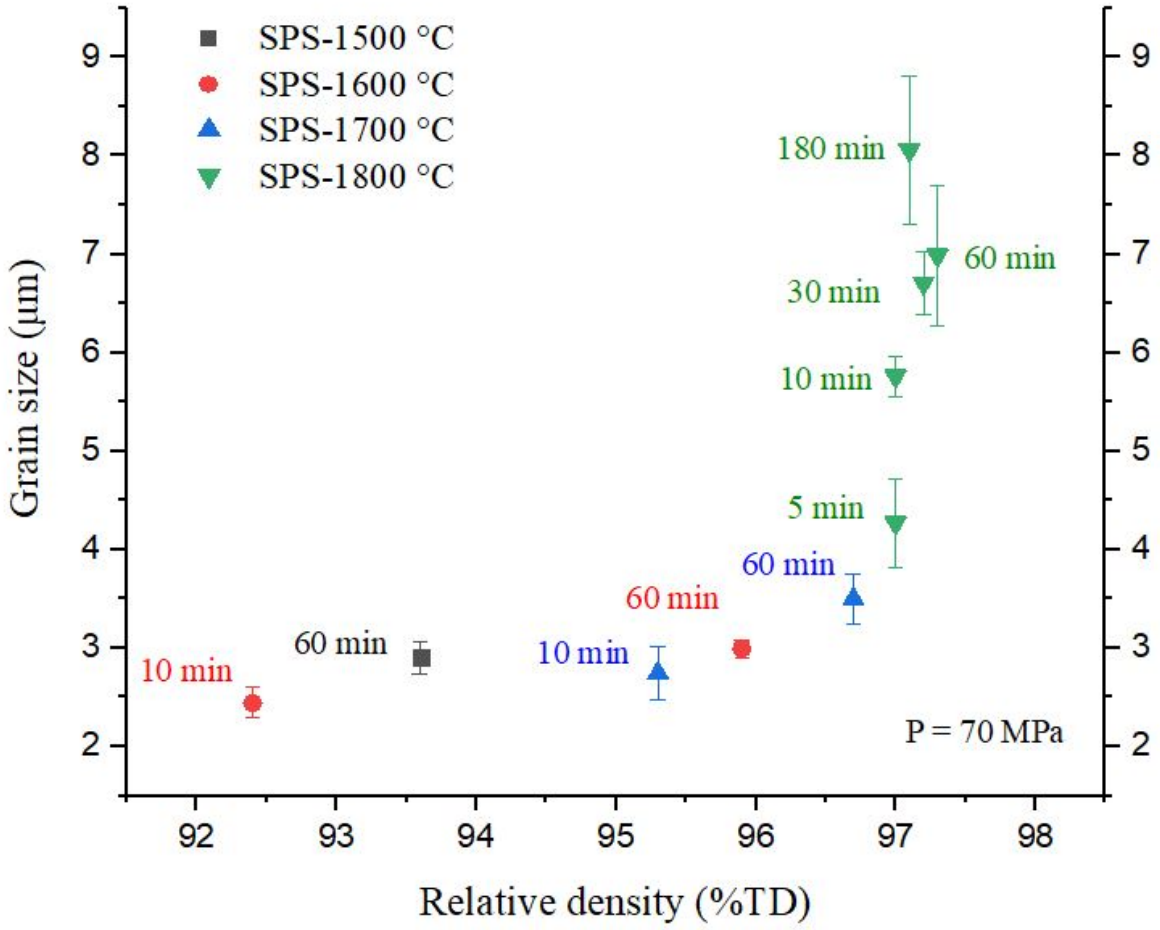

Figure 5-1. Grain size-density trajectory of UN pellets sintered at temperature of 1500 °C (grey), 1600 °C (red), 1700 °C (blue), and 1800 °C (green) under constant pressure of 70 MPa

5.2. Thermophysical properties of burnable absorber (Gd_2O_3 and GdN) added UN pellets

5.2.1. Phase stability of Gd_2O_3 in UN matrix

Thus far, it was reported that Gd_2O_3 has five different phases of cubic (C-form), the monoclinic (B-form), two hexagonal (A- and H-form), and the cubic (X-form) at ambient pressure; nonetheless, the thermodynamic stability of several Gd_2O_3 phases is still under debate whether some of those phases are metastable or not [123]. The thermodynamic instability of Gd_2O_3 was also observed in the UN/Gd_2O_3 composite pellets sintered by SPS. According to phase transformation temperatures (listed in Table 5-1), the monoclinic B-Gd_2O_3 phase (8.05 g/cm^3) was expected to be formed at the sintering temperature of 1800 °C. However, the XRD patterns of UN/Gd_2O_3 composite pellets sintered at 1800 °C (Figure 4-24) revealed that C-Gd_2O_3 phase (7.41 g/cm^3) still maintains its cubic structure. It is noteworthy that pure Gd_2O_3 pellets sintered at 1800 °C, on the other hand, exhibited the pure monoclinic B-Gd_2O_3 phase, which is consistent with the phase transformation temperatures. This implies that the phase transformation of Gd_2O_3 BA could occur unexpectedly during operation under a particular irradiation environment, however, unrevealed yet.

5.2.2. Phase stability of GdN in UN matrix

Although the phase diagram of the UN-GdN binary system has never been investigated yet, their identical crystal structure indicates that the system may exhibit miscibility in the similar manner that the Gd_2O_3-UO_2 system exhibits a solid solution $(Gd_x,U_{1-x})O_2$ phase.

Thus far, it has been reported that the UN system exhibits complete miscibility with several lanthanide-based nitrides including Lanthanum-, Cerium-, Praseodymium-, and Neodymium nitrides [124,125]. To achieve the equilibrium between UN and lanthanide-based nitrides, high-temperature and long-term annealing were required. According to Holleck [125], the equilibrium between UN and CeN was not achieved at an annealing temperature of 1700 °C, but its equilibrium was achieved after 66 h annealing at 1800 °C. In his other work [124], the equilibrium between UN and NdN was obtained after 43h annealing at 1900 °C.

The study conducted by Benedict [126,127], therefore, concluded that the relative lattice

parameter difference (RLPD) between UN and solute nitrides is the main factor that determines the solubility limits. The RLPD values of previous lanthanide-based nitrides are 8.5, 2.7, 5.7, and 4.9 %, respectively. Thus, complete solubility between the UN-GdN system is also anticipated because the RLPD value of GdN to UN is 2.3 %. Although the complete solubility of GdN in UN system was not fully investigated for all compositions in this study since the concentrations of BA compound in the commercial nuclear fuel are typically less than 10 wt%, the formation of solid-solution phase between UN-GdN was confirmed up to 50at%GdN from the XRD peaks shift (Figure 4-28) and corresponding lattice parameters are calculated (Figure 4-29). The formation of solid-solution phase within short-term (60 min) annealing might be enabled by the SPS characteristics, where a high pulsed direct electric current, up to 1000 A, momentarily generates spark plasma with very high temperature (thousands °C) in local areas between particles.

However, the homogeneity of the solid-solution phase obtained in this study is still arguable, because the microstructure of solid-solution UN/GdN pellets (Figure 4-32) is quite similar to those of non-solid-solution UN/GdN pellet (Figure 4-31), where the formation of two-phase structure of UN (brighter) and GdN (darker) was distinctive. One possibility is that the lamellar-like texture would be the main feature of the solid-solution phase, considering the appearance of the texture became apparent with increasing GdN. Additionally, phase boundaries between two phases appeared ambiguous as the appearance of the texture. These features are clearly observed in the solid-solution UN-14.5wt%GdN pellets (Figure 4-32d). Thus, the UN/GdN samples sintered at 2000 °C for 60 min would have not yet reached its equilibrium but contain a solid-solution $(U_{1-x},Gd_x)N$ phase.

Table 5-1. The solid to solid phase transformation temperatures of pure Gd_2O_3 at ambient pressure [123]**. (C represents cubic; B monoclinic; A hexagonal; H hexagonal; and X cubic)**

Transition	Temperature (°C)
C ↔ B	1152 ± 20
B ↔ A	2170 ± 10
A ↔ H	2208 ± 10
H ↔ X	2360 ± 20

Table 5-2. Lattice parameters of the various FCC structure nitrides and corresponding RLPD values compared to UN (Å = 4.8892)

Compound	Lattice parameter (Å)	RLPD $\frac{a_{MN}-a_{UN}}{a_{UN}}\times 100$ (%)	Experimental results
LaN	5.305	+8.5	Complete miscibility at 1900°C after 24 h annealing [124]
CeN	5.022	+2.7	Complete miscibility at 1800°C after 66 h annealing [125]
PrN	5.165	+5.7	Complete miscibility at 1900°C after 24 h annealing [124]
NdN	5.126	+4.9	Complete miscibility at 1900°C after 43 h annealing [125]
*SmN	5.048	+3.3	n/a
*EuN	5.007	+2.4	n/a
*GdN	4.999	+2.3	n/a
TbN	4.936	+1.0	n/a
*DyN	4.894	+0.1	n/a
HoN	4.877	-0.3	n/a
*ErN	4.836	-1.1	n/a
TmN	4.809	-1.6	n/a
YbN	4.785	-2.1	n/a
LuN	4.766	-2 5	n/a
*HfN	4.524	-7.5	Completely soluble > 2000°C

*Burnable absorber candidates

5.2.3. Thermal conductivity of UN-GdN composite pellets

The thermal conductivity of non-solid-solution UN/GdN pellets (blue triangle in Figure 5-2) decreased almost linearly with increasing Gd composition at both 500 and 1000 °C, while the thermal conductivities of solid-solution UN/GdN pellets are somewhat off from the theoretical reference line. To assess the thermal conductivity data further, the Maxwell model [128] was employed. It was assumed in this model that the infinite continuous matrix phase enclosed spherical particles; the thermal interaction between particles would be ignored; no thermal resistance of interfacial boundary of matrix-particles would be taken into account. In this regard, the following equation was derived.

$$k_{eff} = k_m \left[\frac{2k_m + k_p - 2V_p(k_m - k_p)}{2k_m + k_p + V_p(k_m - k_p)} \right] \quad (5\text{-}1)$$

where k_{eff} is the effective thermal conductivity of the composite material, k_m thermal conductivity of matrix, k_p the thermal conductivity of particles, and V_p the volume fraction of particles. To calculate the volume fractions of Gd_2O_3 and GdN particles in the UN matrix, it was assumed that particles are uniformly and randomly distributed throughout the matrix. Thus, areal fractions between particles and matrix measured by SEM images (Figure 4-30) were estimated to be equal to the corresponding volume fractions.

As presented in Figures 5-3 to 5-6, the thermal conductivity of non-solid-solution UN/GdN pellets (violet diamond) was well matched with the effective thermal conductivity estimated by the Maxwell model (blue triangle). The gap between non-solid-solution and the Maxwell prediction increased as GdN concentrations increased. Notably, the values from Maxwell prediction were larger at low temperature and small at high temperature. Therefore, the Maxwell model would slightly overestimate/underestimate the thermal conductivity of UN/GdN composites at low/high temperatures. Nonetheless, considering the assumptions of Maxwell model, this similarity would indicate that the thermal boundary resistance between the GdN particle and the UN matrix might be negligible.

On the other hand, the different tendency was observed in the thermal conductivity of the solid-solution containing UN/GdN pellets (yellow triangle). All solid-solution containing samples exhibited thermal conductivity values 15–20% lower than Maxwell prediction or that of non-solid-solution UN/GdN pellets. One plausible explanation for this different tendency would be the distortion of the electronic band structure in $(U_{1-x},Gd_x)N$ phase. It was demonstrated by Szpunar et al. [72] that the thermal conductivity of UN is mainly dominated by the electron thermal conductivity rather than lattice thermal conductivity. The electron-electron contribution to the thermal conductivity is generally

calculated by the electronic band structures of solids. During the formation of the solid-solution phase, the substitution of Gd atom at U atom site would certainly distort the electronic band structure of UN, and then the decrease of electron heat transport capacity would be followed. Therefore, it is highly anticipated that the thermal conductivity of the solid-solution containing UN/GdN pellets is much lower than that of its two-phase counterpart. These results may indicate that further enhanced thermal conductivity could be available for UN/GdN composite fuel with an optimized microstructure of two-phase lamellae obtainable from relatively low (< 1800 °C) SPS temperature.

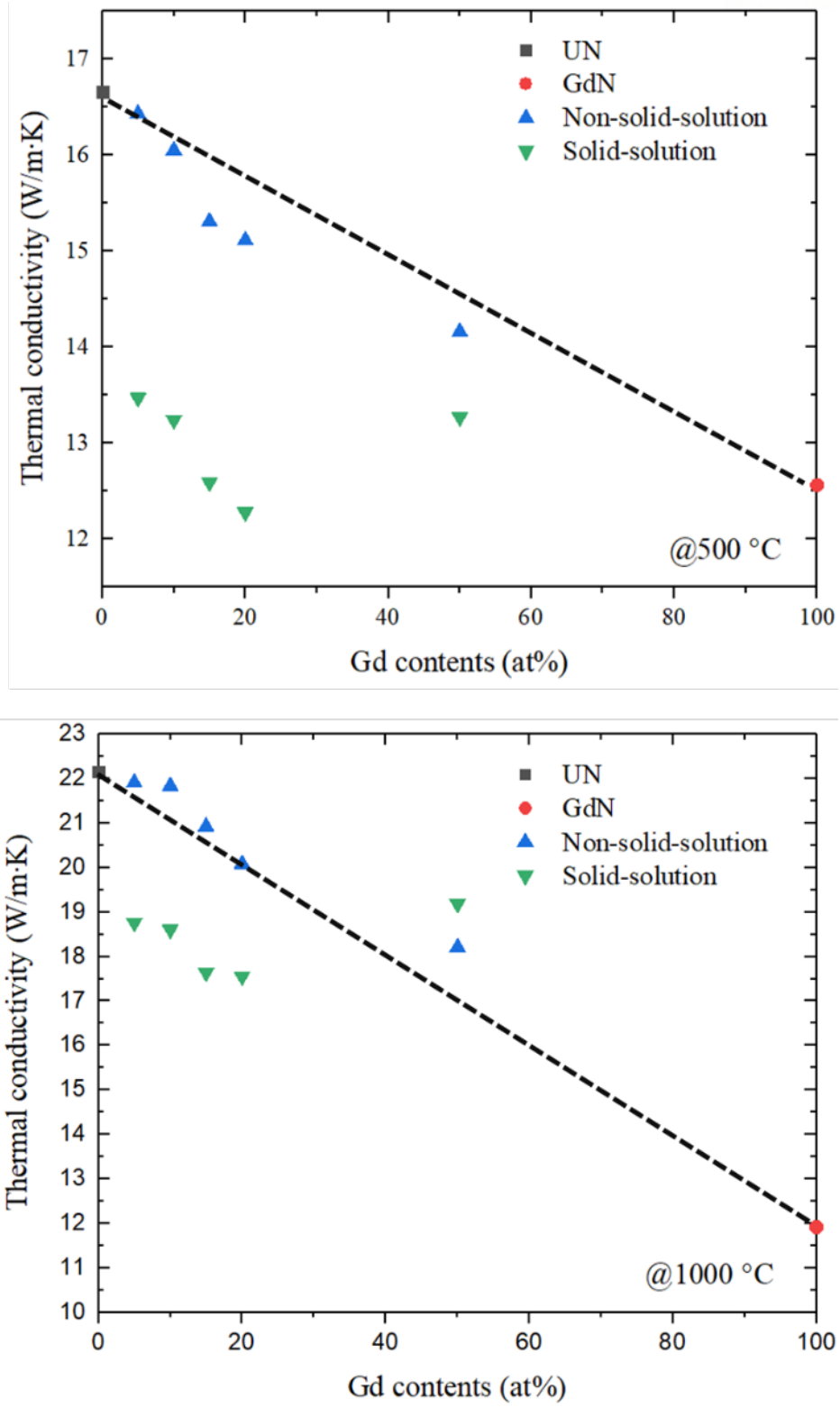

Figure 5-2. Thermal conductivity of GdN added UN pellets at 500 °C (top) and 1000 °C (bottom)

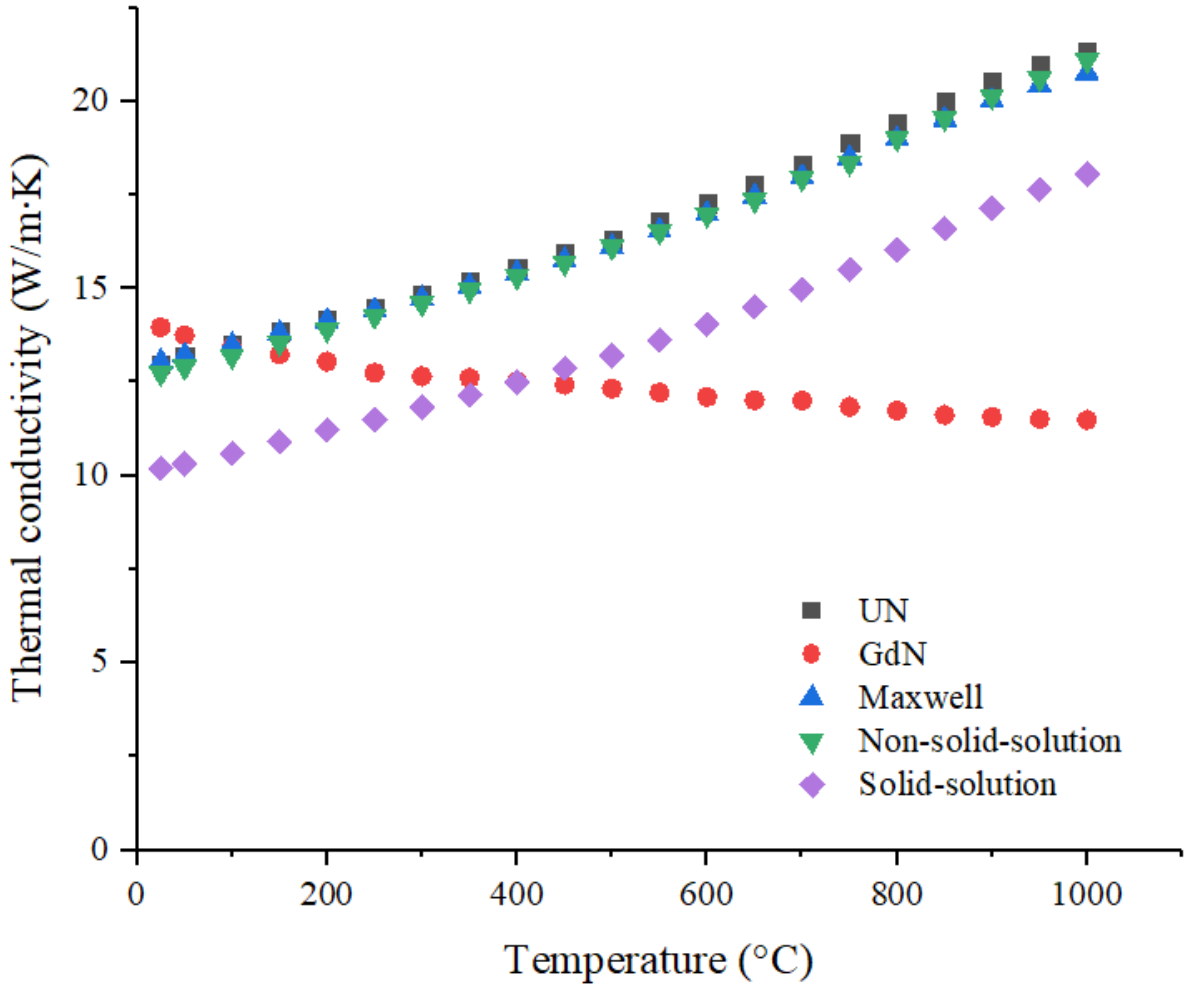

Figure 5-3. Thermal conductivity of SPSed UN + 3.5wt%GdN pellets with calculated values from Maxwell model

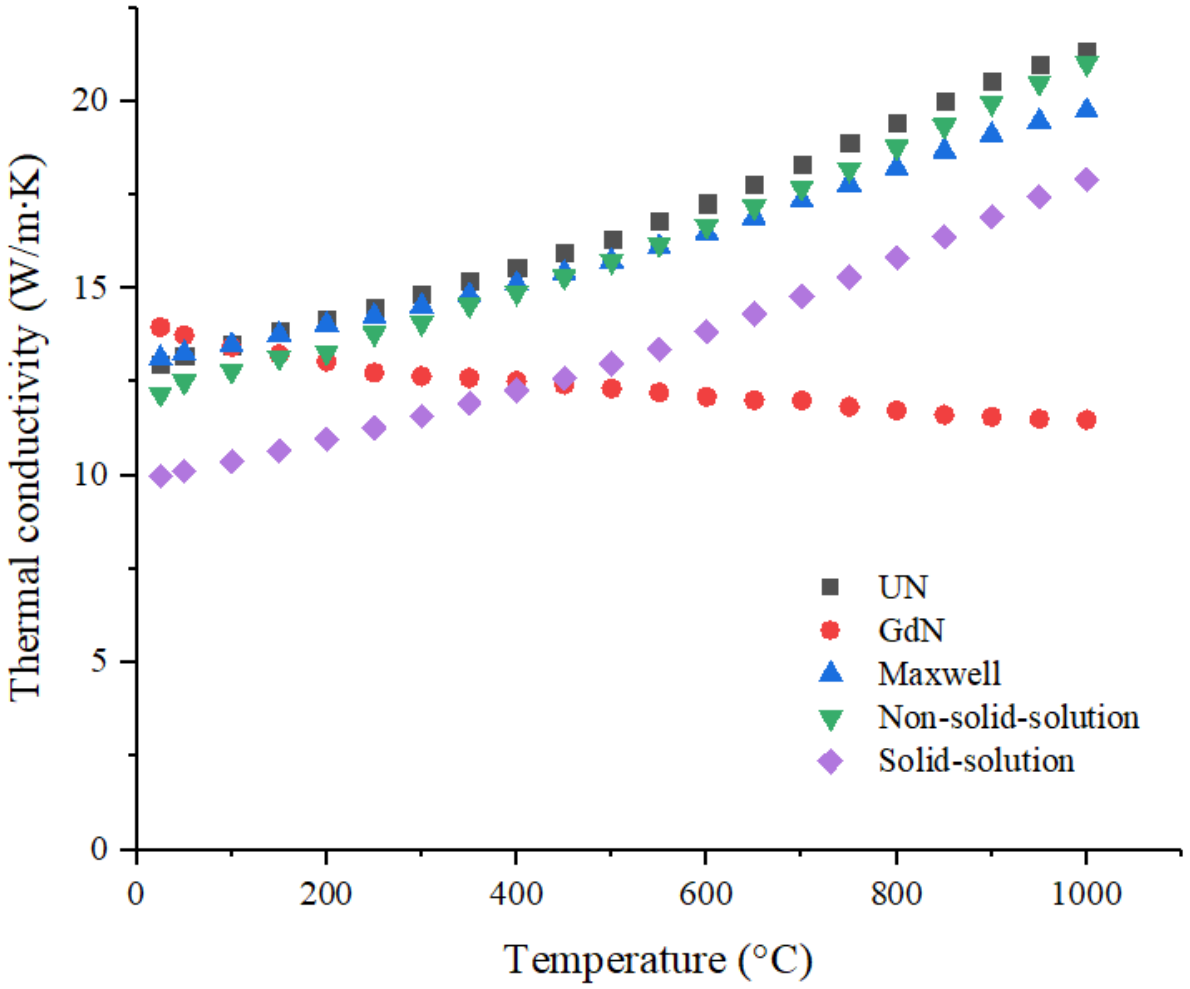

Figure 5-4. Thermal conductivity of SPSed UN + 7.0wt%GdN pellets with calculated values from Maxwell model

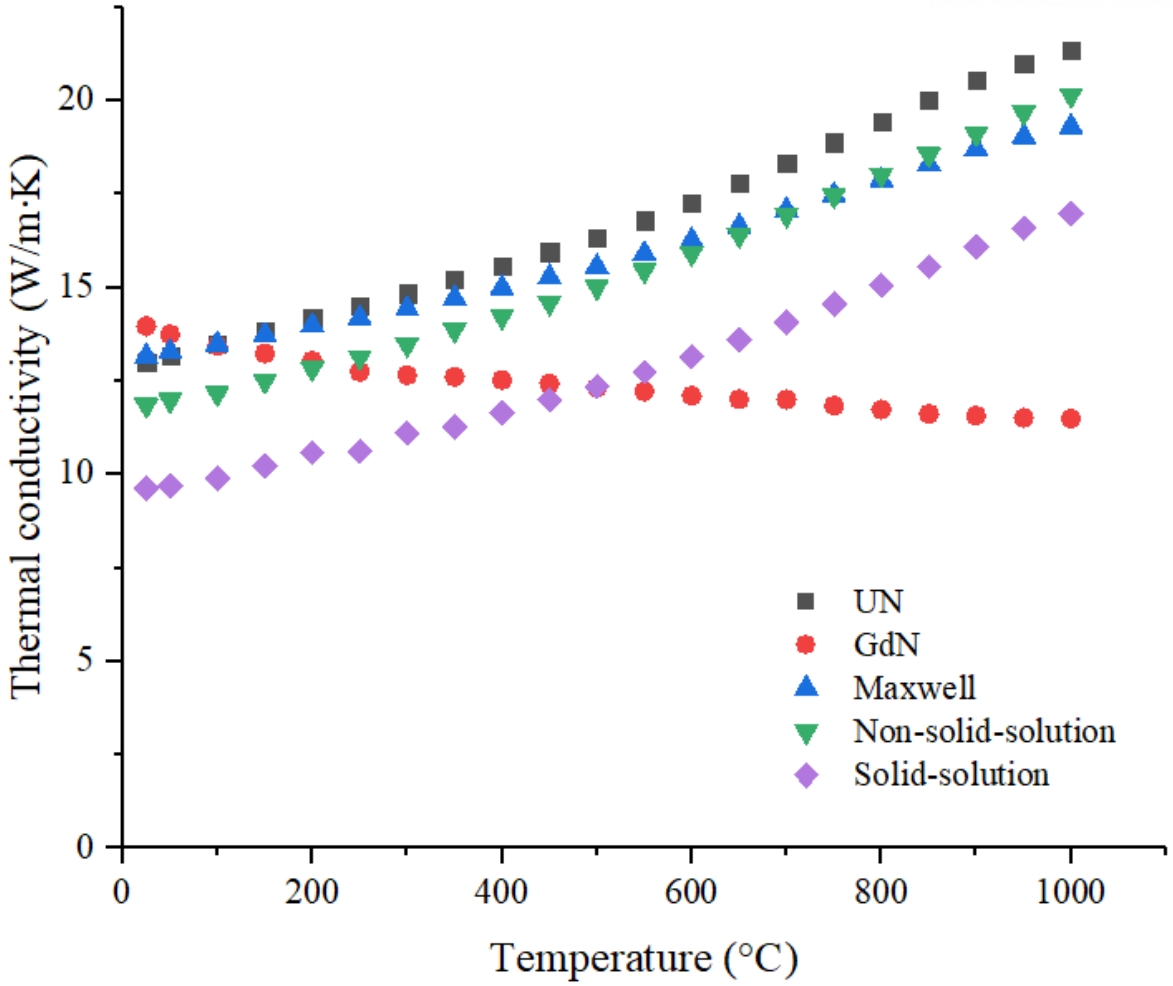

Figure 5-5. Thermal conductivity of SPSed UN + 10.7wt%GdN composite pellets with calculated values from Maxwell model

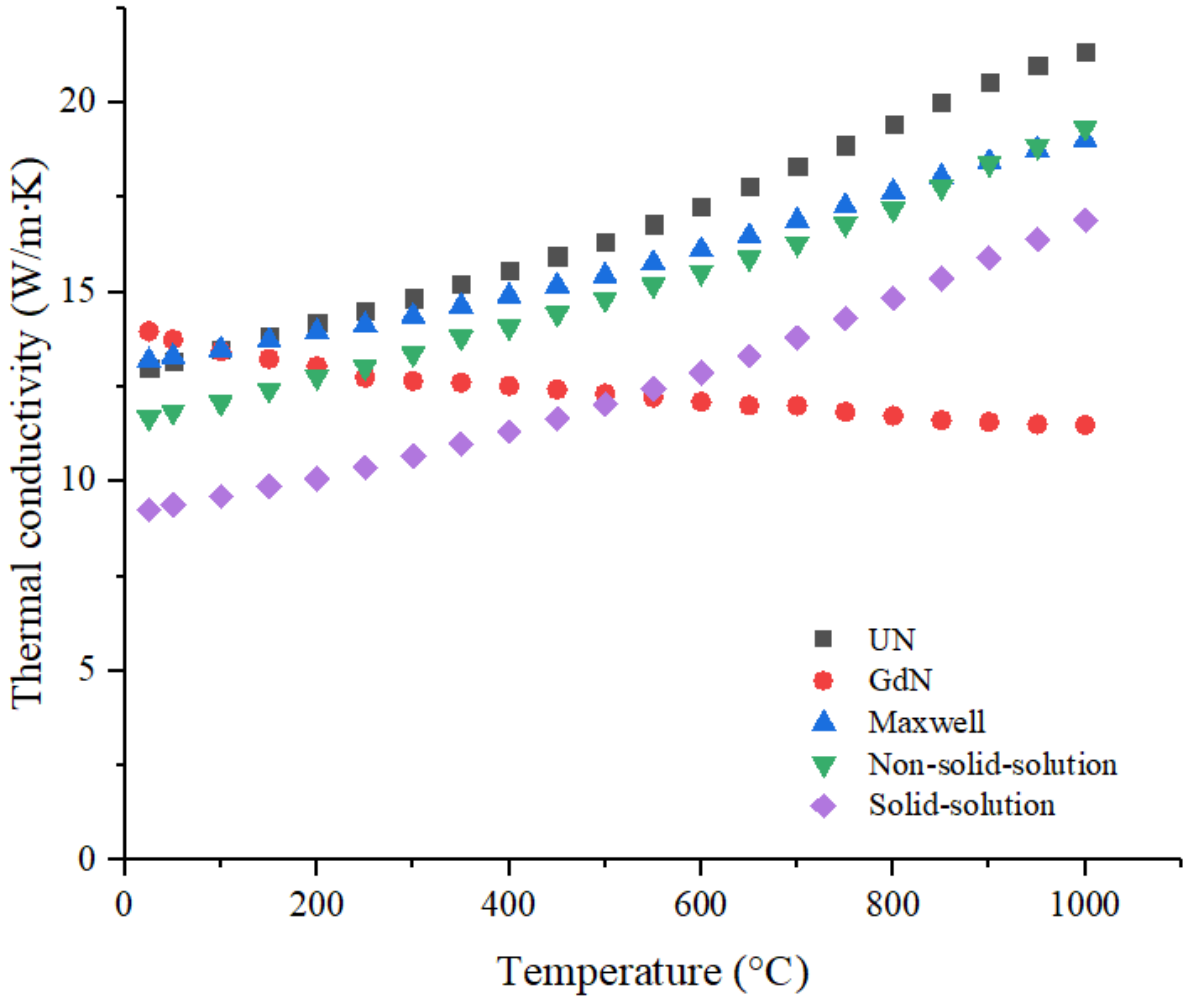

Figure 5-6. Thermal conductivity of SPSed UN + 14.5wt%GdN pellets with calculated values from Maxwell model

Chapter 6. CONCLUSIONS

This study focused on the experimental investigation of the SPS characteristics and thermophysical properties of pure and gadolinium compounds added UN fuel pellets for LWR applications. Various UN pellets were first fabricated at sintering temperatures from 1500 to 1800 °C and dwell times from 5 to 180 min. The microstructural characterization of the thermally etched pure UN pellets was carried out by SEM image analysis. Secondly, UN/Gd_2O_3 and UN/GdN composite pellets were prepared in a wide composition range of Gd_2O_3 (5, 10, and 15 wt%) and GdN (3.5, 7.0, 10.7, 14.5, and 38.4 wt%). The crystallographic and microstructural characterizations of the composite pellets were conducted using XRD and SEM/BSE. The thermal conductivity of samples was measured using LFA at the temperature range of 25–1000 °C.

6.1. Densification and grain growth behavior of UN during SPS

The effect of SPS temperature and dwell time on densification and grain growth of pure UN was clearly revealed in the grain size-density trajectory. At low temperatures below 1700 °C, the density of pellets increased when temperature increases until it reaches the maximum value (~97 %TD) without any notable grain growth. On the contrary, at a temperature of 1800 °C, densification was completed rapidly (less than 5 min) with considerable grain growth. The maximum grain size of 8 μm was obtained with as dwell time increases up to 180 min. Therefore, optimum SPS temperature for UN fuel fabrication would lie between 1700 and 1800 °C at which rapid densification occurs, and thus the fuel fabrication cost could be reduced significantly with short dwell time, unless very large or small grain size is desired to enhance irradiation performance of the fuel such as fission gas release.

6.2. Thermal conductivity of gadolinium compounds added UN burnable absorber fuel pellets

The crystallographic and microstructural characterizations of gadolinium compounds added UN pellets revealed that the solid-solution $(U_{1-x},Gd_x)N$ phase was formed only for UN/GdN pellets SPSed at 2000 °C for 60 min. The two-phase system was maintained for both UN/GdN and UN/Gd_2O_3 pellets SPSed at 1800 °C for 10 min. In general, the thermal conductivity of UN pellet decreased when

Gd compositions increased regardless of its chemical form; however, it still maintained an increasing tendency with increasing temperature for all Gd compositions. The thermal conductivity of two-phase UN/GdN was 88% higher at 1000 °C than that of UN/Gd_2O_3, while the solid-solution UN/GdN pellets exhibited slightly lower thermal conductivity than two-phase UN/GdN pellets. Combined with the fact that GdN has 31% higher neutron absorption capability per unit volume than that of Gd_2O_3, the result of this study would indicate that GdN clearly has a comparative advantage over Gd_2O_3 as a burnable absorber to be implemented with UN fuel. Although the solid-solution phase between UN and GdN would hardly be formed at the suggested SPS temperature between 1700–1800 °C, considering that the solid-solution phase could be formed later due to the enhanced atomic diffusivity under irradiation conditions, the centerline temperature of UN/GdN burnable absorber fuels could be conservatively calculated based on thermal conductivity of solid-solution UN/GdN pellets.

REFERENCES

[1] S.L. Hayes, J.K. Thomas, K.L. Peddicord, Material property correlations for uranium mononitride. III. Transport properties, J. Nucl. Mater. 171 (1990) 289–299. https://doi.org/10.1016/0022-3115(90)90376-X.

[2] M. Amaya, T. Kubo, Y. Korei, Thermal conductivity measurements on UO2+x from 300 to 1,400 K, J. Nucl. Sci. Technol. 33 (1996) 636–640. https://doi.org/10.1080/18811248.1996.9731970.

[3] V.I. Kolyadin, E.P. Il'in, A.G. Kharlamov, V. V. Yakovlev, The thermal conductivity of uranium dioxide, Sov. At. Energy. 36 (1974) 64–66. https://doi.org/10.1007/BF01123109.

[4] J.K. Fink, Thermophysical properties of uranium dioxide, J. Nucl. Mater. 279 (2000) 1–18. https://doi.org/10.1016/S0022-3115(99)00273-1.

[5] A.F. Grachev, L.M. Zabud'ko, Y.A. Ivanov, M. V. Skupov, E.A. Zvir, F.N. Kryukov, O.N. Nikitin, E.E. Marinenko, S.I. Porollo, Results of Studies of BN-600 Fuel Rods with Mixed Uranium-Plutonium Nitride Fuel and ChS68-ID c.d. Steel Cladding, At. Energy. 126 (2019) 182–190. https://doi.org/10.1007/s10512-019-00534-0.

[6] V.M. Troyanov, A.F. Grachev, L.M. Zabud'Ko, M. V. Skupov, D. V. Zozulya, Program and results of reactor tests of mixed nitride fuel for fast reactors, At. Energy. 118 (2015) 96–100. https://doi.org/10.1007/s10512-015-9962-0.

[7] B.D. Rogozkin, N.M. Stepennova, A.A. Proshkin, Mononitride fuel for fast reactors, At. Energy. 95 (2003) 624–636. https://doi.org/10.1023/B:ATEN.0000007886.86817.32.

[8] A.F. Grachev, L.M. Zabud'ko, A.E. Glushenkov, Y.A. Ivanov, G.A. Kireev, M. V. Skupov, I.F. Gil'mutdinov, P.I. Grin', E.A. Zvir, F.N. Kryukov, O.N. Nikitin, Investigations of Mixed Uranium-Plutonium Nitride Fuel in Project Breakthrough, At. Energy. 122 (2017) 185–199. https://doi.org/10.1007/s10512-017-0254-8.

[9] A.F. Grachev, A.A. Zherebtsov, L.M. Zabud'ko, E.A. Zvir, F.N. Kryukov, O.N. Nikitin, M. V. Skupov, Y.A. Ivanov, S.I. Porollo, Results of Investigations of BREST-Type Reactor Fuel Rods with Mixed Uranium-Plutonium Nitride Fuel, Irradiated in BOR-60 and BN-600, At. Energy. 125 (2019) 314–321. https://doi.org/10.1007/s10512-019-00487-4.

[10] J. Choi, B. Ebbinghaus, T. Meier, J. Ahn, Development (LDRD) on Mono-uranium Nitride Fuel

Development for SSTAR and Space Applications, 2006.

[11] S.F. Demuth, SP100 space reactor design, Prog. Nucl. Energy. 42 (2003) 323–359. https://doi.org/10.1016/S0149-1970(03)90003-5.

[12] R.B. Matthews, K.M. Chidester, C.W. Hoth, R.E. Mason, R.L. Petty, Fabrication and testing of uranium nitride fuel for space power reactors, J. Nucl. Mater. 151 (1988) 345. https://doi.org/10.1016/0022-3115(88)90029-3.

[13] G. Giudicelli, Achievable Power Uprates in Pressurized Water Reactors Using Uranium Nitride Fuel, 2017.

[14] W.E. Cummins, R.P. Vijuk, T.L. Schulz, Westinghouse AP1000 advanced passive plant, Proc. Am. Nucl. Soc. - Int. Congr. Adv. Nucl. Power Plants 2005, ICAPP'05. 6 (2005) 3337–3346.

[15] G.A.R. Rao, K. Jayanthi, S.K. Mukerjee, V.N. Vaidya, V. Venugopal, Oxidation behaviour of U2N3, Thermochim. Acta. 159 (1990) 349–356. https://doi.org/10.1016/0040-6031(90)80120-N.

[16] R.M. Dell, V.J. Wheeler, E.J. Mciver, Oxidation of uranium mononitride and uranium monocarbide, Trans. Faraday Soc. 62 (1966) 3591–3606. https://doi.org/10.1039/tf9666203591.

[17] M. Paljević, Z. Despotović, Oxidation of uranium mononitride, J. Nucl. Mater. 57 (1975) 253–257. https://doi.org/10.1016/0022-3115(75)90208-1.

[18] R.M. Dell, V.J. Wheeler, N.J. Bridger, Hydrolysis of uranium mononitride, Trans. Faraday Soc. 63 (1967) 1286–1294. https://doi.org/10.1039/tf9676301286.

[19] S. Sugihara, S. Imoto, Hydrolysis of uranium nitrides, J. Nucl. Sci. Technol. 6 (1969) 237–242. https://doi.org/10.3327/jnst.6.237.

[20] J.E. Antill, B.L. Myatt, Kinetics of the oxidation of UN and U(CO) in carbon dioxide, steam and water at elevated temperatures, Corros. Sci. 6 (1966) 17–23. https://doi.org/10.1016/S0010-938X(66)80046-X.

[21] G.A.R. Rao, S.K. Mukerjee, V.N. Vaidya, V. Venugopal, D.D. Sood, Oxidation and hydrolysis kinetic studies on UN, J. Nucl. Mater. 185 (1991) 231–241. https://doi.org/10.1016/0022-3115(91)90340-D.

[22] J.K. Watkins, E. Sikorski, L. Li, B.J. Jaques, Improved hydrothermal corrosion resistance of un

fuel forms via addition of metallic Constituents, Proc. Topfuel2019. (2019).

[23] D.R. Costa, M. Hedberg, S.C. Middleburgh, J. Wallenius, P. Olsson, D.A. Lopes, UN microspheres embedded in UO2 matrix: An innovative accident tolerant fuel, J. Nucl. Mater. 540 (2020). https://doi.org/10.1016/j.jnucmat.2020.152355.

[24] D.A. Lopes, S. Uygur, K. Johnson, Degradation of UN and UN–U3Si2 pellets in steam environment, J. Nucl. Sci. Technol. 54 (2017) 405–413. https://doi.org/10.1080/00223131.2016.1274689.

[25] P. Malkki, The manufacturing of uranium nitride for possible use in light water reactors, 2015. http://www.diva-portal.org/smash/record.jsf?pid=diva2%3A816319&dswid=-7279.

[26] D.R. Costa, M. Hedberg, S.C. Middleburgh, J. Wallenius, P. Olsson, D.A. Lopes, Oxidation of UN-U2N3/UO2 composites: an evaluation of UO2 as an oxidation barrier for the nitride phases, J. Nucl. Mater. 544 (2020) 152700. https://doi.org/10.1016/j.jnucmat.2020.152700.

[27] L.H. Ortega, B.J. Blamer, J.A. Evans, S.M. McDeavitt, Development of an accident-tolerant fuel composite from uranium mononitride (UN) and uranium sesquisilicide (U3 Si2) with increased uranium loading, J. Nucl. Mater. 471 (2016) 116–121. https://doi.org/10.1016/j.jnucmat.2016.01.014.

[28] J.K. Watkins, A. Gonzales, A.R. Wagner, E.S. Sooby, B.J. Jaques, Challenges and opportunities to alloyed and composite fuel architectures to mitigate high uranium density fuel oxidation: Uranium mononitride, J. Nucl. Mater. (2021) 153048. https://doi.org/10.1016/j.jnucmat.2021.153048.

[29] C. Tritium, Management of Waste Containing Tritium and Carbon-14, 2001.

[30] J. Wallenius, Influence of N-15 Enrichment on Neutronics, Costs and C-14 Production In Nitride Fed Cycle Scenarios, Proc. Symp. Nitride Fuel Cycle Technol. (2004) 111–120.

[31] M.A. DeCrescente, M.S. Freed, S.D. Caplow, USAEC Research and Development Report PWAC-488, 1965.

[32] S.C. Weaver, J.L. Scot, R.L. Senn, B.H. Montgomery, USAEC Report ORNL-4461, 1969.

[33] D. Salvato, J.F. Vigier, M. Cologna, L. Luzzi, J. Somers, V. Tyrpekl, Spark plasma sintering of fine uranium carbide powder, Ceram. Int. 43 (2017) 866–869. https://doi.org/10.1016/j.ceramint.2016.09.136.

[34] B. Li, Z. Yang, J. Jia, P. Zhang, R. Gao, T. Liu, R. Li, H. Huang, M. Sun, D. Mazhao, High temperature thermal physical performance of SiC/UO2 composites up to 1600 °C, Ceram. Int. 44 (2018) 10069–10077. https://doi.org/10.1016/j.ceramint.2018.02.208.

[35] M. Cologna, V. Tyrpekl, M. Ernstberger, S. Stohr, J. Somers, Sub-micrometre grained UO2 pellets consolidated from sol gel beads using spark plasma sintering (SPS), Ceram. Int. 42 (2016) 6619–6623. https://doi.org/10.1016/j.ceramint.2015.12.172.

[36] H. Muta, K. Kurosaki, M. Uno, S. Yamanaka, Thermal and mechanical properties of uranium nitride prepared by SPS technique, J. Mater. Sci. 43 (2008) 6429–6434. https://doi.org/10.1007/s10853-008-2731-x.

[37] P. Malkki, M. Jolkkonen, T. Hollmer, J. Wallenius, Manufacture of fully dense uranium nitride pellets using hydride derived powders with spark plasma sintering, J. Nucl. Mater. 452 (2014) 548–551. https://doi.org/10.1016/j.jnucmat.2014.06.012.

[38] K.D. Johnson, D.A. Lopes, Grain growth in uranium nitride prepared by spark plasma sintering, J. Nucl. Mater. 503 (2018) 75–80. https://doi.org/10.1016/j.jnucmat.2018.02.041.

[39] K.D. Johnson, J. Wallenius, M. Jolkkonen, A. Claisse, Spark plasma sintering and porosity studies of uranium nitride, J. Nucl. Mater. 473 (2016) 13–17. https://doi.org/10.1016/j.jnucmat.2016.01.037.

[40] K. Johnson, V. Ström, J. Wallenius, D.A. Lopes, Oxidation of accident tolerant fuel candidates, J. Nucl. Sci. Technol. 54 (2017) 280–286. https://doi.org/10.1080/00223131.2016.1262297.

[41] J.T. White, A.W. Travis, J.T. Dunwoody, A.T. Nelson, Fabrication and thermophysical property characterization of UN/U3Si2 composite fuel forms, J. Nucl. Mater. 495 (2017) 463–474. https://doi.org/10.1016/j.jnucmat.2017.08.041.

[42] L.G. Gonzalez Fonseca, M. Hedberg, L. Huan, P. Olsson, T. Retegan Vollmer, Application of SPS in the fabrication of UN and (U,Th)N pellets from microspheres, J. Nucl. Mater. 536 (2020) 152181. https://doi.org/10.1016/j.jnucmat.2020.152181.

[43] S. Fukushima, T. Ohmichi, A. Maeda, H. Watanabe, The effect of gadolinium content on the thermal conductivity of near-stoichiometric (U,Gd)O2 solid solutions, J. Nucl. Mater. 105 (1982) 201–210. https://doi.org/10.1016/0022-3115(82)90375-0.

[44] D. Staicu, V. V. Rondinella, C.T. Walker, D. Papaioannou, R.J.M. Konings, C. Ronchi, M. Sheindlin, A. Sasahara, T. Sonoda, M. Kinoshita, Effect of burn-up on the thermal conductivity

of uranium-gadolinium dioxide up to 100 GWd/tHM, J. Nucl. Mater. 453 (2014) 259–268. https://doi.org/10.1016/j.jnucmat.2014.07.006.

[45] R. De Coninck, W. Van Lierde, A. Gijs, Uranium carbide: Thermal diffusivity, thermal conductivity and spectral emissivity at high temperatures, J. Nucl. Mater. 57 (1975) 69–76. https://doi.org/10.1016/0022-3115(75)90179-8.

[46] T. Ogata, Irradiation behavior and thermodynamic properties of metallic fuel, J. Nucl. Sci. Technol. 39 (2002) 675–681. https://doi.org/10.1080/00223131.2002.10875558.

[47] H.D. Lewis, J.F. Kerrisk, Electrical and Thermal Transport Properties of Uranium and Plutonium Carbides: a review of the literature, 1976.

[48] G.D. Mahan, Crystal Structures, 2nd ed., Interscience Publishers, 2019. https://doi.org/10.2307/j.ctvcm4htt.5.

[49] X. Wang, R.Z. Qiu, Q. Wang, L.Z. Luo, Y. Hu, K.Z. Liu, P.C. Zhang, Insights into the Phase Relations in a U-N System Using a Cluster Formula, Inorg. Chem. 56 (2017) 3550–3555. https://doi.org/10.1021/acs.inorgchem.7b00020.

[50] P. Ettmayer, J. Waldhart, A. Vendl, Über die Mischbarkeit von UN mit LaN, CeN, PrN, NdN, SmN, GdN, DyN, und ErN, Monatshefte Für Chemie. 110 (1979) 1109–1112. https://doi.org/10.1007/BF00910958.

[51] R.E. Rundle, N.C. Baenziger, A.S. Wilson, R.A. McDonald, The Structures of the Carbides, Nitrides and Oxides of Uranium, J. Am. Chem. Soc. 70 (1948) 99–105. https://doi.org/10.1021/ja01181a029.

[52] Y. SASA, T. ATODA, Nonstoichiometric Hexagonal Close-Packed Uranium Sesquinitride, J. Am. Ceram. Soc. 53 (1970) 102–105. https://doi.org/10.1111/j.1151-2916.1970.tb12020.x.

[53] N. Masaki, H. Tagawa, THE STRUCTURE OF beta-U,N, 58 (1975) 241–243.

[54] D. Zhou, J. Yu, C. Pu, Y. Song, Prediction of Stable Ground-State Uranium Nitrides at Ambient and High Pressures, ArXiv. (2018). http://arxiv.org/abs/1804.00095.

[55] G.W.C. Silva, C.B. Yeamans, A.P. Sattelberger, T. Hartmann, G.S. Cerefice, K.R. Czerwinski, Reaction sequence and kinetics of uranium nitride decomposition, Inorg. Chem. 48 (2009) 10635–10642. https://doi.org/10.1021/ic901165j.

[56] A. V. Lunev, V. V. Mikhalchik, A. V. Tenishev, V.G. Baranov, Kinetic and microstructural studies of thermal decomposition in uranium mononitride compacts subjected to heating in high-purity helium, J. Nucl. Mater. 475 (2016) 266–273. https://doi.org/10.1016/j.jnucmat.2016.04.018.

[57] T. Hiroaki, Phase relations and thermodynamic properties of the uranium-nitrogen system, J. Nucl. Mater. 51 (1974) 78–89. https://doi.org/10.1016/0022-3115(74)90117-2.

[58] L. Vinet, A. Zhedanov, A "missing" family of classical orthogonal polynomials, J. Phys. A Math. Theor. 44 (2011). https://doi.org/10.1088/1751-8113/44/8/085201.

[59] R. Benz, Melting point maxima of ThC-ThN and of UC-UN solid solutions, J. Nucl. Mater. 31 (1969) 93–98. https://doi.org/10.1016/0022-3115(69)90046-4.

[60] S.L. Hayes, J.K. Thomas, K.L. Peddicord, Material property correlations for uranium mononitride. IV. Thermodynamic properties, J. Nucl. Mater. 171 (1990) 300–318. https://doi.org/10.1016/0022-3115(90)90377-Y.

[61] H. Okamoto, N-U (Nitrogen-Uranium), J. Phase Equilibria. 18 (1997) 107–107. https://doi.org/10.1007/bf02646768.

[62] M. Katsura, H. Serizawa, Formation of a nitrogen-rich α-U2N3+x phase by the reaction of uranium with a stream of ammonia, J. Alloys Compd. 187 (1992) 389–399. https://doi.org/10.1016/0925-8388(92)90444-E.

[63] L. He, M. Khafizov, C. Jiang, B. Tyburska-Püschel, B.J. Jaques, P. Xiu, P. Xu, M.K. Meyer, K. Sridharan, D.P. Butt, J. Gan, Phase and defect evolution in uranium-nitrogen-oxygen system under irradiation, Acta Mater. 208 (2021). https://doi.org/10.1016/j.actamat.2021.116778.

[64] H. Serizawa, K. Fukuda, Y. Ishii, Y. Morii, M. Katsura, Crystallographic study on the phase transition of α-U2N3, J. Nucl. Mater. 208 (1994) 128–134. https://doi.org/10.1016/0022-3115(94)90204-6.

[65] K.O. Obodo, M. Braun, Nitrogen non-stoichiometric stabilization of UN2, Solid State Commun. 254 (2017) 21–25. https://doi.org/10.1016/j.ssc.2017.01.009.

[66] J.T. White, A.T. Nelson, Thermal conductivity of UO2+x and U4O9-y, J. Nucl. Mater. 443 (2013) 342–350. https://doi.org/10.1016/j.jnucmat.2013.07.063.

[67] K. Gofryk, S. Du, C.R. Stanek, J.C. Lashley, X.Y. Liu, R.K. Schulze, J.L. Smith, D.J. Safarik, D.D. Byler, K.J. McClellan, B.P. Uberuaga, B.L. Scott, D.A. Andersson, Anisotropic thermal

conductivity in uranium dioxide, Nat. Commun. 5 (2014) 1–7. https://doi.org/10.1038/ncomms5551.

[68] W. Chen, X.M. Bai, Temperature and composition dependent thermal conductivity model for U-Zr alloys, J. Nucl. Mater. 507 (2018) 360–370. https://doi.org/10.1016/j.jnucmat.2018.05.021.

[69] K. Kurosaki, K. Yano, K. Yamada, M. Uno, S. Yamanaka, Molecular dynamics study of the thermal conductivity of uranium mononitride, J. Alloys Compd. 311 (2000) 305–310. https://doi.org/10.1016/S0925-8388(00)01127-0.

[70] Q. Yin, A. Kutepov, K. Haule, G. Kotliar, S.Y. Savrasov, W.E. Pickett, Electronic correlation and transport properties of nuclear fuel materials, Phys. Rev. B - Condens. Matter Mater. Phys. 84 (2011) 1–7. https://doi.org/10.1103/PhysRevB.84.195111.

[71] J.A. Webb, I. Charit, Analytical determination of thermal conductivity of W-UO 2 and W-UN CERMET nuclear fuels, J. Nucl. Mater. 427 (2012) 87–94. https://doi.org/10.1016/j.jnucmat.2012.04.020.

[72] B. Szpunar, J.I. Ranasinghe, L. Malakkal, J.A. Szpunar, First principles investigation of thermal transport of uranium mononitride, J. Phys. Chem. Solids. 146 (2020) 109636. https://doi.org/10.1016/j.jpcs.2020.109636.

[73] E.K. Storms, An equation which describes fission gas release from UN reactor fuel, J. Nucl. Mater. 158 (1988) 119–129. https://doi.org/10.1016/0022-3115(88)90161-4.

[74] K. Tanaka, K. Maeda, K. Katsuyama, M. Inoue, T. Iwai, Y. Arai, Fission gas release and swelling in uranium-plutonium mixed nitride fuels, J. Nucl. Mater. 327 (2004) 77–87. https://doi.org/10.1016/j.jnucmat.2004.01.002.

[75] H. Blank, K. Richter, M. Coquerelle, H. Matzke, M. Campana, C. Sari, I.L.F. Ray, Dense fuels in Europe, J. Nucl. Mater. 166 (1989) 95–104. https://doi.org/10.1016/0022-3115(89)90181-5.

[76] B.D. Rogozkin, N.M. Stepennova, Y.Y. Fedorov, M.G. Shishkov, F.N. Kryukov, S. V. Kuzmin, O.N. Nikitin, A. V. Belyaeva, L.M. Zabudko, Results of irradiation of (U0.55Pu0.45)N and (U 0.4Pu0.6)N fuels in BOR-60 up to ~12 at.% burn-up, J. Nucl. Mater. 440 (2013) 445–456. https://doi.org/10.1016/j.jnucmat.2013.04.033.

[77] Y. Arai, Y. Suzuki, T. Iwai, A. Maeda, T. Sasayama, K. ichi Shiozawa, T. Ohmichi, Fabrication of uranium-plutonium mixed nitride fuel pins for irradiation tests in JMTR, J. Nucl. Sci. Technol. 30 (1993) 824–830. https://doi.org/10.1080/18811248.1993.9734553.

[78] Y.E.F. V.V. Orlov, A.G. SILA-NOVITSKY, V.S. SMIRNOV, V.S. SKIKUNOV, A.I. FILIN, V.V. NAUMOV, S.V. BULAVKIN, B.D. ROGOSKIN, M.G. SHISHKOV, O.N. DUBROVIN, N.M. STEPENNOVA, Mononitride fuel and large scale nuclear power industry, Tech. Comm. Meet. Held Moscow Stud. Fuels with Low Fission Gas Releases, IEA-TECDOC-970. IEA-TECDOC (1996) 155–168.

[79] R.O. Meyer, Analysis of plutonium segregation and central-void formation in mixed-oxide fuels, J. Nucl. Mater. 50 (1974) 11–24. https://doi.org/10.1016/0022-3115(74)90055-5.

[80] S.B. Ross, M.S. El-Genk, R.B. Matthews, Uranium nitride fuel swelling correlation, J. Nucl. Mater. 170 (1990) 169–177. https://doi.org/10.1016/0022-3115(90)90409-G.

[81] J. Rest, M.W.D. Cooper, J. Spino, J.A. Turnbull, P. Van Uffelen, C.T. Walker, Fission gas release from UO2 nuclear fuel: A review, J. Nucl. Mater. 513 (2019) 310–345. https://doi.org/10.1016/j.jnucmat.2018.08.019.

[82] I. Atomic, E. Agency, Related To Extended Burnup, 1992.

[83] R. Restani, M. Horvath, W. Goll, J. Bertsch, D. Gavillet, A. Hermann, M. Martin, C.T. Walker, On the condition of UO2 nuclear fuel irradiated in a PWR to a burn-up in excess of 110 MWd/kgHM, J. Nucl. Mater. 481 (2016) 88–100. https://doi.org/10.1016/j.jnucmat.2016.08.023.

[84] T.B. Lindemer, S.L. Voit, C.M. Silva, T.M. Besmann, R.D. Hunt, Carbothermic synthesis of 820 μm uranium nitride kernels: Literature review, thermodynamics, analysis, and related experiments, J. Nucl. Mater. 448 (2014) 404–411. https://doi.org/10.1016/j.jnucmat.2013.10.036.

[85] Z. Qu, B. Yin, J. Ren, X. Wang, Low temperature synthesis of uranium mononitride powder, J. Nucl. Mater. 496 (2017) 193–196. https://doi.org/10.1016/j.jnucmat.2017.09.032.

[86] W.O. GREENHALGH, Kinetic Measurements for the Carbothermic Synthesis of UN, PuN, and (U,Pu)N, J. Am. Ceram. Soc. 56 (1973) 553–557. https://doi.org/10.1111/j.1151-2916.1973.tb12414.x.

[87] K. Minato, M. Akabori, M. Takano, Y. Arai, K. Nakajima, A. Itoh, T. Ogawa, Fabrication of nitride fuels for transmutation of minor actinides, J. Nucl. Mater. 320 (2003) 18–24. https://doi.org/10.1016/S0022-3115(03)00163-6.

[88] T. Muromura, H. Tagawa, Formation of uranium mononitride by the reaction of uranium dioxide

with carbon in ammonia and a mixture of hydrogen and nitrogen. II. Reaction rates, J. Nucl. Mater. 80 (1979) 330–338. https://doi.org/10.1016/0022-3115(79)90196-X.

[89] Y. Arai, C. Sari, J.C. Spirlet, Investigation of the reaction UO2 + x + NpO2 + C + N2 by thermogravimetry, J. Nucl. Mater. 185 (1991) 159–166. https://doi.org/10.1016/0022-3115(91)90331-Z.

[90] E.O. Speidel, D.L. Keller, Fabrication and properties of hot-pressed uranium mononitride, 1963. http://catalog.hathitrust.org/Record/100168477.

[91] V.J. TENNERY, T.G. GODFREY, R.A. POTTER, Sintering of UN as a Function of Temperature and N2 Pressure, J. Am. Ceram. Soc. 54 (1971) 327–331. https://doi.org/10.1111/j.1151-2916.1971.tb12306.x.

[92] B.D. Rogozkin, N.M. Stepennova, G.A. Bergman, A.A. Proshkin, Thermochemical stability, radiation testing, fabrication, and reprocessing of mononitride fuel, At. Energy. 95 (2003) 835–844. https://doi.org/10.1023/B:ATEN.0000018996.79185.bc.

[93] P.E. Evans, T.J. Davies, Uranium nitrides, J. Nucl. Mater. 10 (1963) 43–55. https://doi.org/10.1016/0022-3115(63)90115-6.

[94] C.B. Yeamans, G.W.C. Silva, G.S. Cerefice, K.R. Czerwinski, T. Hartmann, A.K. Burrell, A.P. Sattelberger, Oxidative ammonolysis of uranium(IV) fluorides to uranium(VI) nitride, J. Nucl. Mater. 374 (2008) 75–78. https://doi.org/10.1016/j.jnucmat.2007.06.022.

[95] G.W.C. Silva, C.B. Yeamans, L. Ma, G.S. Cerefice, K.R. Czerwinski, A.P. Sattelberger, Microscopic characterization of uranium nitrides synthesized by oxidative ammonolysis of uranium tetrafluoride, Chem. Mater. 20 (2008) 3076–3084. https://doi.org/10.1021/cm7033646.

[96] Y. Arai, S. Fukushima, K. Shiozawa, M. Handa, Fabrication of (U, Pu)N fuel pellets, J. Nucl. Mater. 168 (1989) 280–289. https://doi.org/10.1016/0022-3115(89)90593-X.

[97] S.D. Caplow, G.W. Lindemann, A.C. Schilling, Fabrication of Low Density Uranium Nitride for High Fission Gas Release, 1965.

[98] N. Ol, S. Hirayama, I. Tanabe, A. Muramatsu, T. Kawada, Preparation of high density uranium nitride and uranium carbonitride fuel pellets, J. Nucl. Sci. Technol. 9 (1972) 521–527. https://doi.org/10.1080/18811248.1972.9734891.

[99] J. i Y. Chang, “Hot-Pressing Study on Mixed Uranium-Plutonium Nitride for Advanced Reactor

Fuel," 1975.

[100] Z.Y. Hu, Z.H. Zhang, X.W. Cheng, F.C. Wang, Y.F. Zhang, S.L. Li, A review of multi-physical fields induced phenomena and effects in spark plasma sintering: Fundamentals and applications, Mater. Des. 191 (2020) 108662. https://doi.org/10.1016/j.matdes.2020.108662.

[101] M. Asou, J. Porta, Prospects for poisoning reactor cores of the future, Nucl. Eng. Des. 168 (1997) 261–270. https://doi.org/10.1016/s0029-5493(96)01322-2.

[102] A.A. Galahom, Investigation of different burnable absorbers effects on the neutronic characteristics of PWR assembly, Ann. Nucl. Energy. 94 (2016) 22–31. https://doi.org/10.1016/j.anucene.2016.02.025.

[103] R.A. Matzie, S.E. Ritterbusch, System 80+ TM standard plant: Design and operations overview, Int. Symp. Evol. Water Cool. React. Issues, Technol. Econ. Viability. (1998) 430–442. http://inis.iaea.org/Search/search.aspx?orig_q=RN:31007062%0Ahttp://www.iaea.org/inis/collection/NCLCollectionStore/_Public/31/007/31007062.pdf%0Ahttps://inis.iaea.org/search/search.aspx?orig_q=RN:31007062.

[104] J.-P.A. Renier, M.L. Grossbeck, Development of Improved Burnable Poisons for Commerical Nuclear Power Reactors, 2001.

[105] A.R. Massih, S. Persson, Z. Weiss, Modelling of (U, Gd)O2 fuel behaviour in boiling water reactors, J. Nucl. Mater. 188 (1992) 323–330. https://doi.org/10.1016/0022-3115(92)90492-4.

[106] D.M. Camarano, F.A. Mansur, A.M.M. Santos, L.S. Ribeiro, A. Santos, Thermal Conductivity of UO2–BeO–Gd2O3 Nuclear Fuel Pellets, Int. J. Thermophys. 40 (2019) 1–9. https://doi.org/10.1007/s10765-019-2574-5.

[107] K. Iwasaki, T. Matsui, K. Yanai, R. Yuda, Y. Arita, T. Nagasaki, N. Yokoyama, I. Tokura, K. Une, K. Harada, Effect of Gd2 O3 Dispersion on the Thermal Conductivity of UO2, J. Nucl. Sci. Technol. 46 (2009) 673–676. https://doi.org/10.1080/18811248.2007.9711574.

[108] M. Hirai, S. Ishimoto, Thermal Diffusivities and Thermal Conductivities of UO2-Gd2O3, J. Nucl. Sci. Technol. 28 (1991) 995–1000. https://doi.org/10.3327/jnst.28.995.

[109] R. Metroka, Fabrication of Uranium Mononitride Compacts, NASA Tech. Note. (1970) 1–31. https://ntrs.nasa.gov/search.jsp?R=19700022336.

[110] I.L. Tangen, Y. Yu, T. Grande, R. Høier, M.A. Einarsrud, Preparation and characterisation of

aluminium nitride-titanium nitride composites, J. Eur. Ceram. Soc. 24 (2004) 2169–2179. https://doi.org/10.1016/S0955-2219(03)00367-4.

[111] ASTM, ASTM E112-13: Standard test methods for determining average grain size, 2013. https://doi.org/10.1520/E0112-13.1.4.

[112] ASTM International, Standard Test Methods for Density of Compacted or Sintered Powder Metallurgy (PM) Products Using Archimedes' Principle, 2013. https://doi.org/10.1520/B0962-13.2.

[113] W. Conshohocken, Standard Test Method for Thermal Diffusivity by the Flash Method 1, 2012. https://doi.org/10.1520/E1461-07.10.1520/E1461-11.2.

[114] W.J. PARKER, R.J. JENKINS, C.P. BUTLER, G.L. ABBOTT, Flash Method of Determining Thermal Diffusivity, Encycl. Therm. Stress. 32 (2014) 1683–1683. https://doi.org/10.1007/978-94-007-2739-7_100240.

[115] J. Zajas, P. Heiselberg, Measurements of thermal diffusivity, specific heat capacity and thermal conductivity with LFA 447 apparatus, 2013.

[116] D.R. Stulland, C.G. Sinke, Thermodynamic properties of elements, U.S. Department of the Interior, Bureau of Mines, 1956. https://books.google.co.kr/books?id=ZjJauQAACAAJ.

[117] C.G. Maier, K.K. Kelley, An equation for the representation of high-temperature heat content data, J. Am. Chem. Soc. 54 (1932) 3243–3246. https://doi.org/10.1021/ja01347a029.

[118] R. Benz, M.G. Bowman, Some Phase Equilibria in the Uranium-Nitrogen System, J. Am. Chem. Soc. 88 (1966) 264–268. https://doi.org/10.1021/ja00954a015.

[119] M. Torche, G. Schmerber, M. Guemmaz, A. Mosser, J.C. Parlebas, Non-stoichiometric niobium nitrides: Structure and properties, Thin Solid Films. 436 (2003) 208–212. https://doi.org/10.1016/S0040-6090(03)00616-3.

[120] G. Linker, R. Smithey, O. Meyer, Superconductivity in MoN films with NaCl structure, J. Phys. F Met. Phys. 14 (1984). https://doi.org/10.1088/0305-4608/14/7/005.

[121] M.R. Castell, Wulff shape of microscopic voids in UO2 crystals, Phys. Rev. B - Condens. Matter Mater. Phys. 68 (2003) 1–8. https://doi.org/10.1103/PhysRevB.68.235411.

[122] R. Bjørk, V. Tikare, H.L. Frandsen, N. Pryds, The effect of particle size distributions on the

microstructural evolution during sintering, J. Am. Ceram. Soc. 96 (2013) 103–110. https://doi.org/10.1111/jace.12100.

[123] M. Zinkevich, Thermodynamics of rare earth sesquioxides, Prog. Mater. Sci. 52 (2007) 597–647. https://doi.org/10.1016/j.pmatsci.2006.09.002.

[124] H. Holleck, E. Smailos, F. Thümmler, Zur mischphasenbildung der mononitride in den systemen U- (Y, La, Pr)-N, J. Nucl. Mater. 32 (1969) 281–289. https://doi.org/10.1016/0022-3115(69)90077-4.

[125] H. Holleck, E. Smailos, F. Thümmler, Zur mischkristallbildung von un mit den nitriden der seltenen erden CeN und NdN, in: J. Nucl. Mater., 1968: pp. 105–109. https://doi.org/10.1016/0022-3115(68)90061-5.

[126] F. Torrens, G. Castellano, Nuclear Science and Technology, Chem. Ind. Tech. Chem. Eng. EUR-5766 (2020) 311–330. https://doi.org/10.1201/9780429286674-17.

[127] U. Benedict, The solubility of solid fission products in carbides and nitrides of uranium and plutonium Part I: Literature review on experimental results, EUR-5766 (1977).

[128] M. James Clerk, A treatise on electricity and magnetism, Oxford University Press, 2010. https://doi.org/10.1017/CBO9780511709333.

Appendix A. Supplementary Data

A.1. Thermal diffusivities of samples measured

Table B-1 Thermal diffusivity of pure elements pellets

Samples	UN (1800 °C, 10 min)	GdN (1800 °C, 10 min)	Gd_2O_3 (1000 °C, 10 min)
Temperature (°C)	Thermal conductivity (mm^2/s)		
25	4.456	5.446	1.909
50	4.491	5.331	1.769
100	4.554	5.153	1.546
150	4.647	5.022	1.387
200	4.748	4.897	1.272
250	4.842	4.734	1.184
300	4.939	4.650	1.106
350	5.041	4.587	1.057
400	5.136	4.512	1.011
450	5.221	4.433	0.972
500	5.292	4.351	0.939
550	5.375	4.268	0.913
600	5.444	4.183	0.890
650	5.506	4.101	0.870
700	5.566	4.047	0.855
750	5.614	3.939	0.842
800	5.650	3.847	0.830
850	5.688	3.748	0.823
900	5.716	3.665	0.817
950	5.724	3.575	0.811
1000	5.718	3.490	0.807

Table B-2. Thermal diffusivity of UN + Gd_2O_3 pellets (SPS - 1800 °C, 10 min)

Sample	UN + Gd_2O_3 (SPS - 1800 °C, 10 min)		
Gd_2O_3 composition (wt%)	5	10	15
Temperature (°C)	Thermal conductivity (mm^2/s)		
25	3.786	3.370	2.857
50	3.628	3.369	2.818
100	3.670	3.359	2.788
150	3.652	3.369	2.785
200	3.757	3.394	2.777
250	3.723	3.444	2.798
300	3.804	3.500	2.819
350	4.002	3.540	2.829
400	4.006	3.517	2.857
450	4.034	3.603	2.862
500	4.103	3.628	2.865
550	4.160	3.664	2.879
600	4.198	3.699	2.891
650	4.243	3.727	2.905
700	4.273	3.750	2.894
750	4.329	3.795	2.944
800	4.359	3.806	2.946
850	4.379	3.806	2.982
900	4.431	3.844	2.958
950	4.442	3.843	2.982
1000	4.421	3.859	2.973

Table B-3. Thermal diffusivity of UN + GdN pellets (SPS - 1800 °C, 10 min)

Sample	UN + GdN (SPS - 1800 °C, 10 min)				
GdN composition (wt%)	3.5	7	10.7	14.5	38.4
Temperature (°C)	Thermal conductivity (mm^2/s)				
25	4.409	4.249	4.163	4.128	4.530
50	4.438	4.333	4.183	4.157	4.526
100	4.495	4.393	4.206	4.200	4.517
150	4.589	4.489	4.294	4.290	4.538
200	4.693	4.517	4.389	4.388	4.677
250	4.801	4.673	4.477	4.459	4.599
300	4.898	4.755	4.577	4.560	4.650
350	4.998	4.896	4.686	4.685	4.691
400	5.089	4.978	4.779	4.748	4.830
450	5.172	5.076	4.867	4.828	4.898
500	5.260	5.166	4.954	4.908	4.935
550	5.325	5.248	5.038	4.969	4.979
600	5.389	5.324	5.113	5.009	5.024
650	5.420	5.396	5.183	5.043	5.065
700	5.493	5.450	5.254	5.073	5.104
750	5.504	5.491	5.306	5.131	5.138
800	5.578	5.547	5.361	5.143	5.175
850	5.610	5.595	5.406	5.206	5.185
900	5.654	5.650	5.452	5.276	5.206
950	5.676	5.688	5.501	5.302	5.224
1000	5.707	5.730	5.531	5.338	5.250

Table B-4. Thermal diffusivity of UN + GdN pellets (SPS - 2000 °C, 60 min)

Sample	UN + GdN (SPS - 2000 °C, 60 min)				
GdN composition (wt%)	3.5	7	10.7	14.5	38.4
Temperature (°C)	Thermal conductivity (mm^2/s)				
25	3.578	3.486	3.387	3.302	3.577
50	3.598	3.510	3.389	3.329	3.566
100	3.660	3.565	3.429	3.374	3.596
150	3.743	3.643	3.526	3.440	3.672
200	3.836	3.736	3.630	3.499	3.755
250	3.925	3.821	3.625	3.585	3.871
300	4.021	3.918	3.776	3.676	3.961
350	4.117	4.015	3.819	3.768	4.058
400	4.212	4.108	3.926	3.855	4.168
450	4.298	4.182	4.008	3.941	4.288
500	4.372	4.269	4.083	4.028	4.388
550	4.450	4.345	4.161	4.116	4.490
600	4.523	4.428	4.234	4.190	4.597
650	4.592	4.502	4.303	4.266	4.702
700	4.648	4.564	4.372	4.338	4.786
750	4.715	4.626	4.432	4.409	4.876
800	4.771	4.682	4.488	4.485	4.955
850	4.829	4.743	4.541	4.542	5.037
900	4.883	4.795	4.598	4.607	5.113
950	4.929	4.847	4.647	4.654	5.192
1000	4.954	4.889	4.671	4.712	5.248

A.2. Thermal conductivity of samples measured

Table B-5. Thermal conductivity of pure elements pellets

Sample	UN (1800 °C, 10 min)	GdN (1800 °C, 10 min)	Gd_2O_3 (1000 °C, 10 min)
Temperature (°C)	Thermal conductivity (W/m·K)		
25	13.001	13.964	4.012
50	13.188	13.747	3.715
100	13.498	13.439	3.300
150	13.850	13.242	2.936
200	14.199	13.051	2.689
250	14.516	12.749	2.518
300	14.845	12.652	2.365
350	15.206	12.607	2.312
400	15.575	12.526	2.208
450	15.952	12.431	2.149
500	16.332	12.326	2.121
550	16.800	12.219	2.080
600	17.278	12.109	2.038
650	17.786	12.011	2.021
700	18.338	12.002	2.009
750	18.891	11.842	2.031
800	19.436	11.738	2.035
850	20.005	11.624	2.057
900	20.541	11.572	2.117
950	20.986	11.514	2.139
1000	21.336	11.489	2.184

Table B-6. Thermal conductivity of UN + Gd_2O_3 pellets (SPS - 1800 °C, 10 min)

Sample	UN + Gd_2O_3 (SPS - 1800 °C, 10 min)		
Gd_2O_3 composition (wt%)	5	10	15
Temperature (°C)	Thermal conductivity (W/m·K)		
25	10.647	9.289	7.680
50	10.265	9.338	7.614
100	10.485	9.406	7.613
150	10.482	9.469	7.627
200	10.817	9.566	7.624
250	10.748	9.735	7.706
300	11.012	9.923	7.788
350	11.641	10.097	7.872
400	11.710	10.076	7.982
450	11.884	10.406	8.063
500	12.218	10.600	8.172
550	12.543	10.836	8.309
600	12.844	11.093	8.456
650	13.210	11.372	8.643
700	13.561	11.657	8.767
750	14.037	12.057	9.118
800	14.444	12.352	9.318
850	14.832	12.624	9.638
900	15.349	13.052	9.795
950	15.696	13.309	10.070
1000	15.908	13.616	10.234

Table B-7. Thermal conductivity of UN + GdN pellets (SPS - 1800 °C, 10 min)

Sample	UN + GdN (SPS - 1800 °C, 10 min)				
GdN composition (wt%)	3.5	7	10.7	14.5	38.4
Temperature (°C)	Thermal conductivity (W/m·K)				
25	12.741	12.186	11.851	11.686	11.813
50	12.908	12.507	11.984	11.844	11.876
100	13.197	12.800	12.165	12.082	11.973
150	13.551	13.160	12.499	12.422	12.126
200	13.910	13.296	12.832	12.767	12.582
250	14.271	13.799	13.136	13.025	12.448
300	14.602	14.088	13.479	13.373	12.664
350	14.958	14.566	13.862	13.806	12.860
400	15.315	14.896	14.222	14.079	13.340
450	15.684	15.307	14.598	14.431	13.646
500	16.111	15.736	15.009	14.819	13.889
550	16.517	16.186	15.454	15.188	14.178
600	16.970	16.667	15.916	15.534	14.497
650	17.367	17.184	16.408	15.900	14.835
700	17.945	17.689	16.946	16.290	15.196
750	18.359	18.191	17.461	16.805	15.570
800	19.013	18.773	18.016	17.196	15.978
850	19.546	19.349	18.560	17.777	16.324
900	20.124	19.958	19.115	18.396	16.720
950	20.611	20.498	19.676	18.860	17.115
1000	21.096	21.024	20.147	19.341	17.540

Table B-8. Thermal conductivity of UN + GdN pellets (SPS - 2000 °C, 60 min)

Sample	UN + GdN (SPS - 2000 °C, 60 min)				
GdN composition (wt%)	3.5	7.0	10.7	14.5	38.4
Temperature (°C)	Thermal conductivity (W/m·K)				
25	10.199	9.984	9.623	9.255	9.831
50	10.322	10.117	9.691	9.390	9.861
100	10.599	10.373	9.899	9.609	10.046
150	10.902	10.665	10.243	9.862	10.341
200	11.215	10.982	10.592	10.079	10.646
250	11.508	11.267	10.616	10.368	11.043
300	11.824	11.592	11.098	10.674	11.369
350	12.153	11.928	11.275	10.994	11.724
400	12.503	12.275	11.661	11.317	12.133
450	12.856	12.593	11.998	11.663	12.591
500	13.209	12.985	12.346	12.041	13.015
550	13.615	13.382	12.739	12.456	13.475
600	14.049	13.843	13.154	12.865	13.981
650	14.513	14.317	13.595	13.316	14.515
700	14.977	14.793	14.074	13.792	15.018
750	15.513	15.303	14.556	14.297	15.573
800	16.041	15.823	15.053	14.847	16.124
850	16.595	16.379	15.560	15.356	16.713
900	17.143	16.914	16.090	15.904	17.306
950	17.654	17.443	16.590	16.390	17.928
1000	18.063	17.913	16.982	16.903	18.479

ACKNOWLEDGEMENTS

First of all, I express my sincere gratitude to my advisor, Dr. Sangjoon Ahn for his endless support and consideration. It was truly an honor for me to study under his instruction. I would like to thank my committee members, Dr. Hee Reyoung Kim, Dr. Jaeyoung Park, Dr. Eisung Yoon, and Dr. Seung Ho Jung for their insightful comments and guidance.

I thank all members of URANUM group for their partnership and teamwork. I thank early group members, Dr. Myeongkyu Lee and Geon Kim, for their dedication and contribution to this successful radioactive nuclear materials laboratory. I had the pleasure to work with Dr. Yunsong Jung, Jungsu Ahn, Changhyun Nam, Woong Ha, and Taewook Moon.

I would like to thank the members of INFUEL group, Dr. Taewon Cho, Dr. Cheolmin Lee, and Dr. Gwanyoon Jung for their encouragement and valuable help during my research period.

Lastly, I am grateful to my family for their support throughout my life. I thank my father in heaven, Jungho Kim, for his devotion and love. I thank my mother, Meeok Kwak and my sister, Inae Kim for supporting and believing in me. I thank Jeongeun Kim for loving me and always being with me.